ANALYSIS OF CATHODE INTERFACES IN SOLID STATE LITHIUM BATTERIES

by

Alexander Amadore Delluva

M.S., University of Colorado Boulder, 2017

B.S., University of Delaware, 2015

A thesis submitted to the

Faculty of the Graduate School of the

University of Colorado in partial fulfillment

of the requirement for the degree of

Doctor of Philosophy

Department of Chemical and Biological Engineering

2021

Committee Members:

Adam Holewinski

Al Weimer

Chunmei Ban

Se-Hee Lee

Will Medlin

Delluva, Alexander Amadore (Ph.D., Chemical Engineering Program)

Analysis of Cathode Interfaces in Solid State Lithium Batteries

Thesis directed by Professor Adam Holewinski

Interfaces between electrodes and the electrolyte in solid state lithium batteries frequently involve disparate materials in contact with one another under the effect of a large electrochemical potential—rather extreme conditions that can often lead to interfacial reaction and degradation, ultimately resulting in cell failure. Here, methodologies and analyses for probing the fundamental behavior at solid-solid interfaces for solid state lithium batteries are developed and explored, specifically investigating cathode interfaces with the solid electrolyte $Li_7La_3Zr_2O_{12}$ (LLZO).

To investigate of cathode compatibility with LLZO from a primarily electrochemical perspective, $LiMn_2O_4$ (LMO) was chosen as a model cathode due to its wide operable voltage window and the extensive body of literature in other electrolyte systems available for comparison. Thus, LMO|LLZO|Li full cells are constructed and galvanostatic cycling combined with electrochemical impedance spectroscopy (EIS) is used to assess changes in cell capacity and resistances as a function of cycle number. A series of symmetric cells isolating individual electrode-electrolyte interfaces aids in pinpointing the specific sources of cell capacity fade. Combined with X-ray photoelectron spectroscopy (XPS) depth-profiling, these analyses indicate a region of interdiffusion occurs at the LMO-LLZO interface, thereby suggesting their incompatibility as a cathode-electrolyte pairing.

To further explore behavior at the buried solid-solid interfaces, a novel electrochemical mass spectrometry (EC-MS) system is developed and implemented to probe gas-evolution from these interfaces under electrochemical load. It is commonly accepted, that despite extensive mitigation procedures, Li_2CO_3 is able to re-form on the surface of LLZO after its removal. Li_2CO_3 can therefore become a contaminant present at cell interfaces during synthesis, Interfacial Li_2CO_3 oxidation occurs in LMO|LLZO|Li cells starting at charging potentials relevant for the operation of common cathode materials. Evolution of CO_2 and O_2 from Li_2CO_3 decomposition is detected by EC-MS, and further confirmed via its detection under the same conditions in blocking Au|LLZO|Li cells. The decomposition of interfacial Li_2CO_3 is shown to cause large increases in cell impedance alongside significant capacity loss.

The techniques developed in the proceeding studies are then applied to a solid state Li-O_2 system, where patterned gold electrodes deposited onto LLZO act as cathodes, providing a conductive-network for the nucleation of the discharge product. The use of a carbon-free cathode and the absence of liquid electrolytes—two cell common cell components that result in parasitic side reactions—facilitates direct assessment of the Li-O_2 chemistry in a solid state system. It is found that by cycling these cells at high temperatures, which is permitted through the use of solid electrolytes, the thermally-enhanced electronic conductivity of the discharge products permits much thicker discharge product film growth than in traditional aprotic electrolyte Li-O_2 cells.

Acknowledgments

This thesis would not have been possible without the support of a large number of coworkers, friends, and family who I need to acknowledge for the years of support they have given to me.

First, I need to thank my advisor Adam Holewinski for his help and understanding during the course of my Ph.D. Adam taught me what it means to really care about the underlying problems in research and to truly strive for the best and most thorough understanding of a problem you can have. When we began the work present in this thesis, the lab wasn't even built yet and we were both relatively new to the battery field. Things have come a long way since then, and without Adam's deep understanding of physics and chemistry we would not have even made it close to this point. Thank you for constantly challenging me to be a better researcher, and thank you for allowing me the opportunity to pursue the exact area of research that I came to graduate school for.

I also need to say a large thank you to all members of the Holewinski research group for aiding me in both science-related and science-unrelated ways. In particular, Jessica Dudoff for many, many hours spent discussing underlying mechanisms in batteries, coding expertise, and knowledge of x-ray photoelectron spectroscopy. Adam Baz and Alex Roman were incredibly valuable resource in helping to build the lab as well as discussing both electrochemical mechanisms and mass-spectrometry during my tenure. Taylor Spivey and Joseph Hasse for many detailed discussions as well as positive interactions that helped me achieve my goals. Jonas Kulberg-Savercool was incredible undergraduate researcher for me in the final year of my PhD and his work and abilities helped immensely. Lastly, Dragan

Mejic fabricated all of the electrochemical cells used in these experiments and this work would not have been possible without his help.

Thank you to my Mom and Dad for helping me to grow and become the person I am today, as well as being constantly being supportive and listening to what I had to say along all of the steps across my life and Ph.D. Thank you to my brother, Anthony, for being a continued inspiration to believe in your passions, as well as being a positive, supportive role model by entire life. And thank you to my Grandparents, Aunts, and Uncles for all supporting me in your own unique ways, and just being an overall positive force in my life.

Finally, thank you to my fiancé and love of my life, Adrienne. Thank you for your immense compassion and understanding over these past years. Without your help I think I may have actually lost it some point during this Ph.D. Thank you for understanding the pressures I was under and thank you for listening to me vent at what were truly absurd hours of the night. Through listening and understanding you have aided me in achieving my goals and facilitated me becoming a better person along the way, and I will never be able to thank you enough for that.

Contents

List of Tables

List of Figures

1 Introduction

1.1 Lithium-ion Batteries

Development on lithium-ion batteries began during the 1970s and in the many years since then, they have become the most widely-used rechargeable battery by a significant margin. The beginnings of lithium-ion batteries saw engineers at Exxon, led by Stanley Whittingham, experimenting with TiS_2, where its ability to electrochemically intercalate lithium ions would be the basis for a lithium-ion battery.[1] Investigations of lithium intercalation into $LiCoO_2$ (LCO)[2], and $LiMn_2O_4$ (LMO)[3] by John Goodenough were to follow, both of which yielded positive results as potential cathode materials for a Li-ion battery. However, these cathode materials needed a complimentary anode and the development of the carbon anode by Akira Yoshino culminated in the commercialization of the lithium-ion chemistry (using $LiCoO_2$) in 1991 by Sony.[4] The next major event in the history of lithium-ion was the development of another suitable cathode material $LiFePO_4$ (LFP).[5] These three materials laid the backbone for the further refinement of the lithium-ion chemistry for the years to come. Transporting to present day, lithium-ion batteries are everywhere, and research towards new electrode materials is ongoing—the goal of which is to continually improve the safety and energy density of lithium-ion batteries. Absent from this discussion of the history of lithium-ion batteries has been the development of electrolytes for these cells, where research to replace the flammable liquid electrolytes currently used in lithium-ion cells with non-flammable solid

electrolytes—the implementation of which is the subject of this thesis— is currently being heavily pursued.

1.1.1 Theory

A battery is comprised of three primary components: cathode, anode and electrolyte. There are also secondary components such as separators, current collectors, and housing. In a lithium-ion cell the cathode is defined as the positive electrode and the anode is defined as the negative electrode. This definition is consistent with the polarity of these electrodes during discharge for a galvanic cell, and while the polarity of these electrodes inverts during charging, the naming convention dictates that the electrodes referred to as the cathode and anode do not switch with the cell polarity. The electrolyte is the substance through which ions move from anode to cathode (or vice-versa) during cell cycling. The most common electrolytes for lithium batteries are aprotic liquids with lithium salts dissolved inside of them, however, as will be discusses in the proceeding section, these electrolytes can also be comprised of solid materials with high lithium conductivity.

Operation of lithium batteries is realized through the use of intercalation electrodes; intercalation referring to a type of insertion chemical reaction. An insertion reaction involves the insertion of an ion into a crystal lattice, while intercalation specifically refers to this process when the host crystal structure consists of layered sheets. However, intercalation has come to be used interchangeably with insertion in this regard, so will be used as the general term for

this thesis. An intercalation reaction between a lithium ion and a host transition metal oxide, occurs via the following equation:

$$1.1)\ Li_{1-x}MO + xLi^{+} + xe^{-} \leftrightarrows Li_xMO$$

Transition metal oxides are typically the cathodes in Li-ion cells, and therefore during discharge this reaction proceeds in the forward direction, while during charge the reactions proceeds in the reverse direction. For the anode, which is traditionally comprised of graphitic carbon, intercalation occurs according to the following equation:

$$1.2)\ 6C + xLi^{+} + xe^{-} \leftrightarrows Li_xC_6$$

Thus, this reaction proceeds in the reverse direction for discharge, and the forward direction for charge—opposite that of intercalation process occurring at the cathode. A diagram of a lithium-ion battery with a transition metal oxide cathode, carbon anode, and liquid electrolyte is shown in **Figure 1.1.**

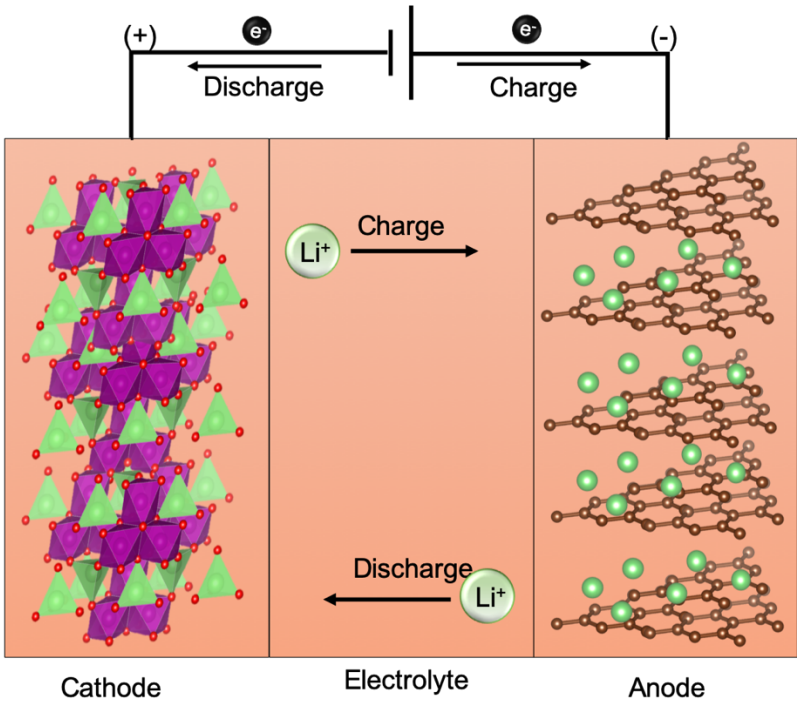

Figure 1.1. Simplified diagram of a typical Li-ion battery with a carbon anode and transition metal oxide cathode illustrating both charging and discharging operation. Design adapted from[6].

Discharge in a battery is the more energetically-favorable process, meaning this is the direction in which the reaction will naturally proceed. Thus, energy is extracted from the battery in the form of electricity during discharge, by allowing lithium ions to flow from anode to cathode, generating an electric current. During charge, energy is stored in the battery by using an applied electric current to force lithium ions from cathode to anode, back to their higher-energy, charged state. One complete battery cycle is thus a discharge of the battery followed by a charge of the battery.

The open circuit voltage (or potential) of a battery is determined by the following equation:

$$1.3)\ E = \frac{(\mu)_A - \mu_C}{e}$$

Where E is the cell voltage , $(\mu)_A$ and μ_C are the chemical potentials of the anode and cathode, and *e* is the magnitude of the electronic charge.[7] As lithium ions move from anode to cathode or cathode to anode, the chemical potentials of the cathode and anode shift, resulting in shifts in the operating voltage of the battery. Voltages in lithium batteries are therefore determined by the choice of material for the anode and cathode, and are most commonly given in reference to Li/Li^+. Common operating voltages are typically found to be in the range of 2.0-5.0 V vs Li/Li^+. The behavior at an individual electrode in a lithium-ion battery can be understood by the Nernst Equation:[8]

$$1.4)\ E = E^{o\prime} + \frac{RT}{nF}\ln\frac{C_O^*}{C_R^*}$$

Where E is the potential at the electrode, $E^{o\prime}$is the formal potential of the electrode, F is the Faraday constant, *n* is the stoichiometric number of electrons involved in the reaction, R is the ideal gas constant, T is the temperature, C_O^* is the bulk concentration of the oxidized species, and C_R^* is the bulk the concentration of the reduced species. Thus, the potential at each electrode can be interpreted as a function of the concentrations of the reduced and oxidized species that are present for an electrochemical half-reaction, such as those given by **Equations 1.1 and 1.2**.

Overpotentials in lithium-ion batteries, or the deviations of the battery's operating voltage from its thermodynamically determined reduction potential, come from several sources in the cell: ohmic, contact, diffusion and charge transfer.[9] Ohmic

overpotentials arise from the conductivities of cell components, contact overpotentials arise from resistance between the current collectors and electrodes, and diffusion overpotentials occur due to the diffusion of lithium ions. Finally, charge transfer overpotentials at the anode and cathode are described by the Butler-Volmer equation:[8]

$$1.5)\ j = j_o\left(e^{-\frac{\alpha F\eta}{RT}} - e^{\frac{(1-\alpha)F\eta}{RT}}\right)$$

Where j is the current density, j_o is the exchange current density, α is the charge transfer coefficient, and η is the overpotential. Thus, this equation directly relates the overpotential observed to the current (in the absence of mass transfer effects), and therefore how the rate of charge or discharge affects the operating voltage of lithium-ion batteries.

1.1.2 Motivation and Prospects for Better Batteries

It has been well established that the growing atmospheric CO_2 level is linked to the burning of fossil fuels, and that the increase in these levels is a primary driving force for climate change. Specifically, it is been predicted that by the year 2100, the global mean temperature could rise by up to 5˚C, coinciding with atmospheric CO_2 concentrations up to 1000 ppm.[10] Thus, sources of energy with significantly reduced environmental impact (in the form of reduced CO_2 emissions), such as solar, wind, geothermal, etc. need to be pursued. Beyond the use of fossil fuels for direct production of electricity, fossil fuels are extensively for used for transportation, the burning of which made up an estimated 35 % of CO_2 emissions in the U.S. in 2019.[11]

Replacing fuel-burning vehicles with electric vehicles will help to curb these emissions if these vehicles directly use electricity generated from alternative sources. Thus, there is a need to supplant these fuels with cleaner sources of energy, but to do so for transportation will require improved energy storage. In the case of electric vehicles, this specifically necessitates the need for improved rechargeable batteries to meet energy density and levelized cost of electricity ($/kWh) goals set by the U.S. Department of Energy.[12]

In addition to the need for more energy-dense cells, modern day lithium-ion cells have still levied several safety concerns, with the thermal runaway induced fires of the Galaxy Note 7 phones being a primary example.[13] The flammability of the electrolytes used in these cells, among other reasons, has motivated researchers to explore replacement of these flammable electrolytes with non-flammable solid electrolytes. The integration of solid electrolytes is a difficult task, but in addition to improved safety, solid electrolytes also offer improved energy and power density over traditional lithium-ion cells.[14] Specifically, improvements in energy density occur if the use of a solid electrolyte enables replacement of the carbon anode (372mAh/g) with metallic lithium (3860 mAh/g)—which has proven to offer poor cycle life and additional safety concerns when paired with traditional electrolytes.[15] A detailed discussion of solid electrolytes will follow in the proceeding sections.

1.2 Solid Electrolytes for Lithium Batteries

Liquid electrolytes in lithium-ions batteries permit transport of ions through them during battery operation by means of dissolved lithium ionic salts. In contrast,

solid electrolytes by definition are ionically-conductive materials in the solid phase of matter, that permit ionic transport through their crystal lattice via three mechanisms: interstitial directly hopping, interstitial knockoff, and vacancy directly hopping.[16] Research into solid electrolytes for lithium batteries started with LiN_3,[17] but it wasn't until the development of the lithium phosphorus oxynitride (LiPON) that research in this area started gaining more wide-spread attention.[18] While many of LiPON's qualities were favorable for lithium batteries, its low ionic conductivity relative to liquid electrolytes (about 3 orders of magnitude less), and the low areal capacities for commercial LiPON thin-film cells meant it could not serve as a true replacement electrolyte for the liquid electrolytes in larger devices.[18] The pursuit of solid electrolytes with higher conductivities eventually resulted in the synthesis of $Li_7La_3Zr_2O_{12}$ (LLZO), the electrolyte used for studies in this thesis.

LLZO was first synthesized by Murugan et al. in 2008, and was found to have a garnet-like crystal structure.[19] However, follow-up studies noticed that upon the high-temperature sintering of the material, which is necessary for densifying the electrolyte, the material was being doped by Al from Al_2O_3 boats used as vessels for the procedure.[20,21] The concertation of Al doping was investigated and found to play a clear role in whether a cubic or tetragonal garnet structure would form, the former being more desirable due to its higher conductivity.[22] Seeing the effect this inadvertent doping had, research into how different dopants would affect the properties of LLZO revealed several dopants that result in desirable changes to the electrolyte in addition to Al. Primarily these are niobium, cerium, gallium, tantalum,

tungsten, but combinations of multiple different dopants have also been investigated.[23]

The first working full cell utilizing LLZO as the electrolyte was published in 2010,[24] utilizing a lithium anode and Li_2CoO_2 cathode, but the cell suffered from poor performance. As discussed previously, lithium anodes have thus far proven to be unstable in liquid electrolyte systems due to dendritic shorting, but hopes for solid electrolytes were that the high shear modulus of these electrolytes would prevent the penetration of these dendrites;[25] however this was not the case. Dendritic shorting still proved to be a problem for LLZO[26,27], highlighting the need for better understanding of how solid-solid interfaces behave in garnet-containing cells.

1.3 Solid-Solid Interfaces with LLZO

Buried solid-solid interfaces are notoriously difficult to probe, while at the same time, interfacial impedances are considered to be one of the primary challenges in the pursuit of commercially viable solid state batteries.[28] More drastically, interfacial reactions between cell components can render certain combinations of electrodes and electrolytes completely incompatible. Thus, developing methodologies that can facilitate rapid testing and understanding of these interfaces is of the utmost importance.

1.3.1 Anodic-LLZO Interface

The overwhelming majority of studies with insight into the anodic-LLZO interface have used Li as the anode, because the aforementioned gains in energy density (relative to current carbon anodes) achieved through implementation of

lithium metal anodes are a primary driving force for research into solid electrolytes such as LLZO.

Li anodes operate differently than the carbon anodes in typical lithium-ion batteries. Rather than storing energy through the intercalation of lithium ions, lithium ions are stripped and plated from/to the surface of the lithium metal, and thus move from the metallic to ionic state or vice versa (**Figure 1.2**).

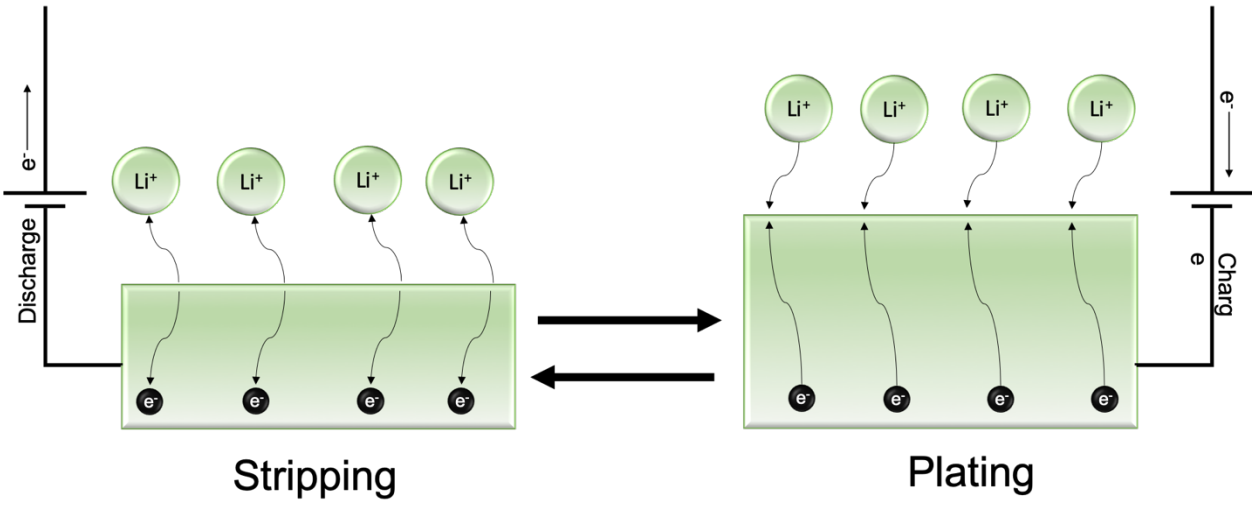

Figure 1.2. Stripping and plating reactions for a lithium metal anode.

Thus, for a lithium metal anode, during cell discharge lithium ions are stripped from the surface of the anode to travel through the electrolyte toward the cathode, while during charge lithium ions move through the electrolyte to be plated as lithium metal on the surface of the anode.

To understand the behavior of full cells utilizing LLZO, the use of symmetric cells (in this case Li | LLZO | Li) has been widely employed because they better isolate electrode-electrolyte interactions thus making it easier to draw conclusions about cell

behavior. The primary objectives of most symmetric cells studies have been to 1) reduce the interfacial impedance of these cells 2) attain commercially-relevant current densities without dendritic shorting and 3) understand the underlying phenomena that gave rise to issues 1 and 2.

The impedance of the Li-LLZO interface has seen massive reductions through research using symmetric cells, to values of near zero.[29,30] The effects of temperature,[31] pressure,[32] interlayers,[33] electrolyte composition[34], grain boundaries[35] and electrolyte density have all been thoroughly explored for this interface. While initially thought to be highly air stable, the surface of LLZO was later found to react with atmospheric moisture and CO_2, even with just trace amounts when contained within a glovebox environment, forming LiOH and Li_2CO_3 according to **Equations 1.6 and 1.7**:[36]

$$1.6)\ Li_7La_3Zr_2O_{12} + xH_2O \rightarrow Li_{7-x}H_xLa_3Zr_2O_{12} + xLiOH$$

$$1.7)\quad LiOH + ½\ CO2 \rightarrow ½\ Li_2CO_3 + ½\ H_2O$$

These surface layer contaminants were determined to be a contributing factor in the interfacial impedance, due primarily to their lower conductivity relative to LLZO. Thus, characterization and ultimately elimination of these surface layers has been explored to minimize the interfacial impedance. The state-of-the-art methodology for carbonate mitigation is a polishing procedure followed by heat treatment, all contained within an inert (i.e. glovebox) or UHV environment.[30,34] While less-explored than the influence of contaminants on the LLZO, the presence of an oxide layer on Li metal foil commonly employed in these experiments is also found to be a contributing

factor to high impedance,[37] and therefore should be removed via scraping directly prior to cell assembly.

Understanding the nature and behavior of dendritic shorting in these cells has been less of a straight forward problem. While links were found between impedance and the formation of dendrites, the reduction of the Li-LLZO interfacial impedance to near-zero did not permit cycling without dendritic shorting.[30] While initially dendritic shorting was thought to be related to mechanical issues with grain boundaries, single-crystal LLZO studies demonstrated that dendrites would still propagate in their absence.[38,39] Operando neutron diffraction of Cu|LLZO|Li cells suggested that the higher electronic conductivity of LLZO could be at fault, permitting nucleation of the dendrites directly within the electrolyte.[40] The formation of voids at the Li-LLZO interface has also been suggested as cause of dendritic shorting.[29,32] Multiple types of Li dendrite morphologies also being identified, suggesting different mechanisms for dendritic formation may exist.[41] While the exact understanding of dendrite formation and propagation remains elusive, lithium symmetric cells have successfully cycled cells at a rates of 1 mA/cm^2, approaching the necessary 3mA/cm^2 requirements for electric vehicles.[42]

1.3.2 Cathodic-LLZO Interface

When contrasted with the anodic studies where the overwhelming focus is on lithium, cathodic studies have covered a much wider range due to the abundance of cathode materials to be tested. Additionally, symmetric cells have seen far less use for the cathodic interface, so with some exception, most of the information about this

interface is derived from full cell studies. These full cell studies generally fall into two categories depending on the nature of cathode used: those utilizing thin-film deposition techniques for the cathode and those focusing on a more bulk-type cells.

Thin film studies are generally more useful for probing interfacial and fundamental cell behavior, as the cathode-electrolyte interface can be more easily accessed in this configuration. $LiCoO_2$ has been by far the most widely studied electrode, with numerous studies investigating its compatibility with LLZO.[43–46] In particular, Ohta et al. created an LCO | LLZO | Li cell exhibiting just 2% capacity fade over 100 cycles. One of the most detailed interfacial studies used a variety of x-ray techniques as well as taking advantage of symmetric cells to show formation of reaction interfacial reaction products when LCO and LLZO are annealed together.[47] The compatibility of $LiMn_2O_4$ with LLZO is examined in depth in Chapter 2 of this thesis.

In contrast, bulk-type studies have been more focused on realizing working solid state cells that could compete with the state-of-the-art commercial liquid cells. Because of this nature, these studies have often focused on assembly and synthesis methods for creating effective bulk cells (whereas the synthesis of thin-film cells is relatively straightforward and more geared toward investigation of materials compatibility rather than practical operation). In particular, these cells have seen a high degree of engineering through the use of interlayers and interface modification, as well as a wider range of cathode materials. $LiMn_{1.5}N_{0.5}O_2$ was studied as a high-voltage cathode, but ultimately found to be incompatible with LLZO, failing on the

first cycle.[48] $LifePO_4$ (LFP) has been less widely examined with LLZO, but a LFP cell exhibited excellent cycling stability over 100 cycles. An LCO|LLZO|Li with $Li_{2.3}C_{0.7}B_{0.3}O_3$ applied to the LCO-LLZO interface demonstrated the benefits of cathode interlayers to enhance cell performance. Because of the wide parameter space present due the sheer number of cathode materials available, computational studies provide a valuable screening tool for combinations of cathodes and electrolytes, as well as possible interlayers to be placed between these materials, permitting experimental researchers to focus in on the most-favorable LLZO-electrode combinations.[49,50]

1.4 Li-O_2 Batteries

While first being demonstrated in 1996,[51] it was not until the 2010s that research into the Li-O_2 (sometimes referred to as Li-air) battery chemistry gained widespread attention. The large theoretical energy density, comparable to that of gasoline by some estimates, is a primary driving factor for the research interest.[52] Typically, Li-O_2 batteries employ an aprotic liquid electrolyte, lithium anode, and carbon, transition metal, and/or transition metal oxide-based cathode. As will be discussed in section 1.4.2, solid state electrolytes have seen comparatively little attention for Li-O_2 batteries, despite favorable characteristics for the system. During discharge of an Li-O_2 cell, a discharge product is formed on the cathode through the reaction of lithium ions (which move from the anode through the electrolyte) with oxygen on the cell cathode. A. diagram of typical Li-O_2 cell undergoing a discharge reaction is presented in **Figure 1.3.**

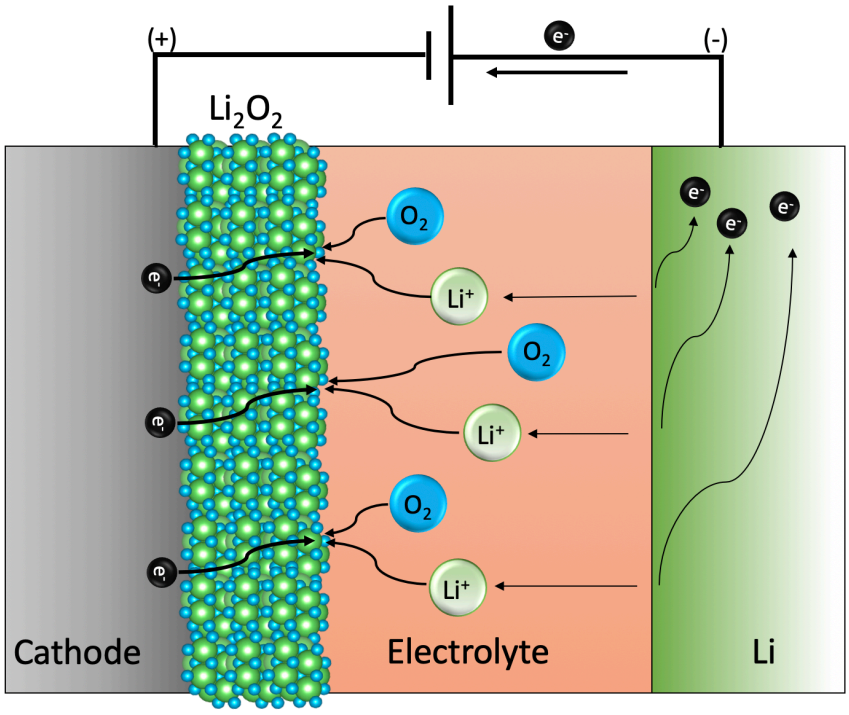

Figure 1.3. Diagram of a typical Li-O_2 cell during discharge operation.

Upon charging, this discharge product is then decomposed, oxygen is evolved, and lithium ions travel back through the electrolyte to become plated out at the lithium anode. The chemical structure of discharge products in Li-O_2 systems is a key factor in these studies, with reports of Li_2O_2, Li_2O, and LiO_2, all being present. Li_2O_2 is by far the most common, Li_2O forms solely at elevated temperatures,[53,54] and the ability to form a stable LiO_2 discharge product has been contested.[55,56]

The formation of Li_2O_2 obeys the following overall discharging and charging reactions:

$$1.8)\ 2Li^+ + O_2 + 2e^- \rightarrow Li_2O_2$$

$$1.9)\ Li_2O_2 \rightarrow 2Li^+ + O_2 + 2e^-$$

For Li_2O, these reactions proceed via:

$$1.10)\ 2Li^+ + \frac{1}{2}O_2 + 2e^- \rightarrow Li_2O$$

$$1.11)\ 2Li_2O \rightarrow 4Li^+ + O_2 + 4e^-$$

Characterization and analysis of the nature of discharge products in Li-O_2 cells is one of the most important factors in assessing and improving their performance.

1.4.1 Liquid Cells & the State of the Art

The two most prominent issues leading to poor performance are parasitic reactions between cell components, and the insulating nature of the Li_2O_2 discharge products. The source and nature of parasitic reactions in typical Li-O_2 configurations has been heavily investigated, where typical parasitic products include Li_2CO_3, lithium formate and lithium acetate.[57] In particular carbon-containing compounds[58] and singlet oxygen[59] have been found to be chief offenders for parasitic product formation. It has been suggested that catalysts for Li-O_2 batteries also catalyze the formation of these parasitic products, leading to some doubts about the efficacy of catalysis in the Li-O_2 system,[60] however this efficacy will depend on several factors present in the cell, perhaps most notably the choice of electrolyte.

Early Li-O_2 batteries were understood to operate by the now-termed surface mechanism, where during discharge Li_2O_2 would grow as a film to a limiting thickness, before the 'sudden death' of the cell when the insulating nature of Li_2O_2 resulted in a rapid overpotential increase due to the inability to conduct charge through the Li_2O_2 to continue its formation (**Figure 1.4**).[61]

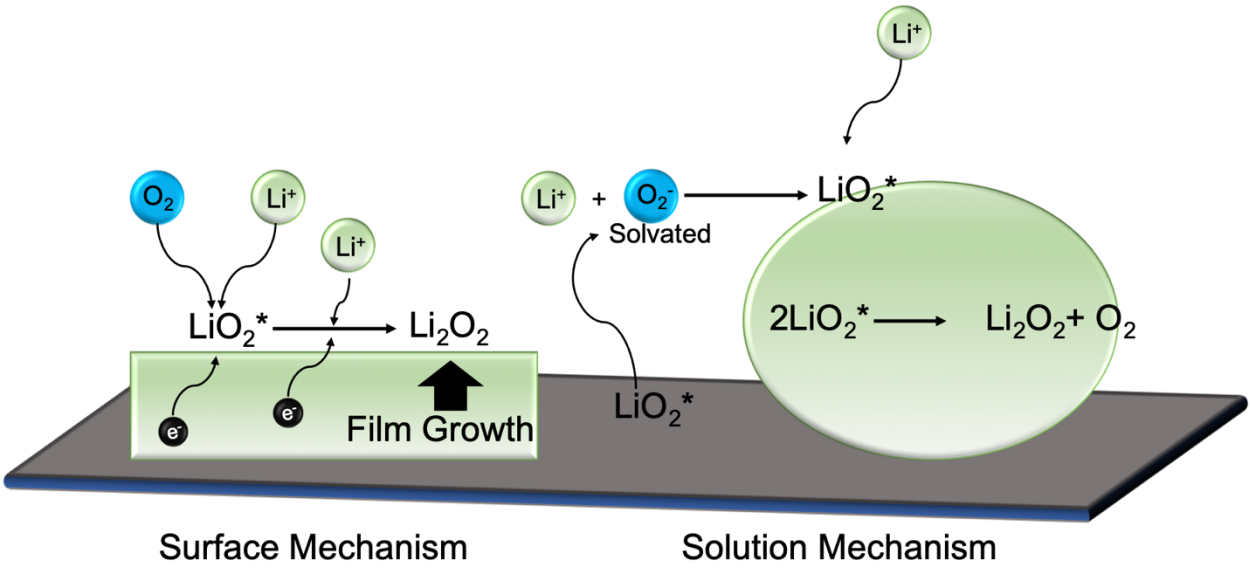

Figure 1.4. Surface and solution mechanism for Li-O_2 cells

The identification of a "solution-phase" mechanism,[62] which was found to operate alongside the surface mechanism,[63] partially overcame this depth of discharge problem, by growing the Li_2O_2 from the solution rather than from the surface of the electrode (**Figure 1.4**). Stemming from this mechanism was a body of research into the use of redox-mediators to facilitate this mechanism for Li-O_2 cells.[64]

However, even in systems that demonstrated large capacity increases by taking advantage of the solution mechanism, Li_2O_2 was found to detach from the cathode, resulting in capacity loss over time.[65] Additionally, these systems often still use materials that are subject to parasitic reactions. Thus, despite the best research efforts, it becomes clear that a solution is necessary that solves both of these issues simultaneously if Li-O_2 batteries are to ever reach the status of commercial product.

1.4.2 Ceramic Solid State Li-O_2 Batteries

The Li-O_2 chemistry also stands to benefit from the use of solid electrolytes over the commonly employed aprotic electrolytes, where solid electrolytes permit higher operating temperatures and therefore deeper discharges through enhancement of the conductivities of these discharge products. Higher operating temperatures (~150˚C) for Li-O_2 batteries have been explored through the use of molten-salt electrolytes, although these were not solid electrolyte studies.[53,54,65]

Solid state Li-O_2 batteries were demonstrated as early as 2010, where a carbon cathode and glass ceramic electrolyte to demonstrate the viability of solid state Li-O_2 cells.[66] Two studies involving patterned platinum cathodes on electrolytes on $Li_{1+x+y}(Ti,Ge)_{2-x}Si_yP_{3-y}O_{12}$ (LATP) solid electrolytes demonstrated the characteristics of solid state discharge products in oxygen and humidified oxygen, although these cells had limited cycle life.[67,68] An Li-air fuel cell utilized LLZO and elevated temperatures to operate, however the cell utilized a carbon cathode operated through an undetermined mechanism involving atmospheric CO_2.[69] Lu et al. utilized a solid state Li-O_2 cell and *in situ* x-ray photoelectron spectroscopy (XPS) to demonstrate the formation of Li_2O_2 discharge products on the surface of a $Li_xV_2O_5$ cathode, however they estimated only a 0.7 nm thick film of discharge product had formed. These studies serve to highlight that while solid state electrolytes have been investigated in several interesting ways for the Li-O_2 system, there is still an a very incomplete understanding of the Li-O_2 system works with solid state electrolytes when compared with aprotic electrolyte Li-O_2 systems.

1.5 Thesis Goals and Structure

By using case studies for LLZO-based Li-ion cells and Li-O_2 cells, this thesis seeks to provide a high-level means and methodology for investigating electrochemically-induced changes at solid-solid interfaces. The methodologies developed here are constructed in a way to highlight their effectiveness at gaining insight into interfacial fundamental mechanisms that cause battery success and failure, such that they could be applied to many like systems. The work heavily focuses cathode-LLZO interface because fundamental studies on this interface were lacking when compared to the anode-LLZO interface.

Chapter 2 lays the groundwork for these investigations by taking a primarily electrochemical approach in assessing the cathodic interface of LMO|LLZO|Li cells. The benefits of fully deconstructing a full cell into a series of symmetric cells to aid in the interpretation of EIS data and mechanisms of capacity fade are demonstrated. Galvanostatic cycling of LMO|LLZO|Li and LMO|LLZO|LMO cells indicate capacity fade, which is also correlated with an increase in cell impedance. These measurements in combination with XPS data demonstrated evidence of electrochemically-induced interfacial reaction and interdiffusion between LMO and LLZO, suggesting there are limits on their viability as an electrode-electrolyte pairing.

Chapter 3 expands upon the results of the previous chapter by developing operando methodology in the form of EC-MS to analyze buried solid-solid interfaces in LLZO solid state cells. It was found that despite rigorous attempts at removal, the

"time-to-synthesis" of thin film LMO|LLZO|Li cells still permitted the growth in a thin-layer of contaminant Li_2CO_3 at the interface between LMO and LLZO. It is shown that the electrochemical decomposition of this layer has detrimental effects on the impedance and capacity of these cells. These results represent the first known report of gaseous evolution from the cathode-electrolyte interface in solid state cells.

Chapter 4 can be seen as a culmination of ideas developed in the proceeding chapters where the knowledge and techniques developed from the previous systems are applied to the more challenging and less understood solid state Li-O_2 chemistry. Patterned Au electrodes are deposited onto LLZO to form Au|LLZO|Li cells. The patterning creates a high-area conductive network for the conduction of electrons allowing discharge product nucleation at the triple-phase-boundary between O_2, LLZO and Au. High temperatures are utilized to thermally enhance the discharge product conductivity, facilitating growth of discharge product films to a significantly greater thicknesses than possible with liquid phase conformal film growth. These results indicate that high temperature operation, enabled by the use of solid electrolytes, is a viable pathway to increase the achievable energy densities of Li-O_2 batteries.

Finally, chapter 5 brings these ideas together to provide broader conclusions about the cathode-LLZO interface and provide outlook for future studies based on these results.

2 Cathode interface compatibility of $LiMn_2O_4$ (LMO) and $Li_7La_3Zr_2O_{12}$ (LLZO) characterized with thin-film solid state electrochemical cells

2.1 Abstract

Solid state lithium ion batteries are a hopeful successor to traditional Li-ion cells that use liquid electrolytes. While a growing body of work has characterized the interfaces between various solid electrolytes and lithium metal, interfaces with common cathode intercalation compounds are comparatively less understood. In this contribution, the influence of polarization and temperature on interfacial stability between $LiMn_2O_4$ (LMO) and $Li_7La_3Zr_2O_{12}$ (LLZO) are investigated. Sputtered thin film LMO electrodes are utilized to permit high-capacity cycling while retaining a large ratio of interfacial area to electrode bulk. Electrochemical impedance spectroscopy (EIS) is compared across a set of full (LMO|LLZO|Li) and symmetric (LMO|LLZO|LMO, Li|LLZO|Li, and Au|LLZO|Au) cells in order to delineate impedance features that are specific to evolution of the cathode interface. Additional X-ray photoelectron spectroscopy (XPS) provides evidence of a limited interfacial reaction between LMO and LLZO that coincides with an increase in the impedance of the LMO-LLZO interface. A graphical abstract depicting the results of this paper can be seen in **Figure 2.1,** the work in this chapter was originally published and adapted from a journal article in ACS Applied Materials & Interfaces.[70]

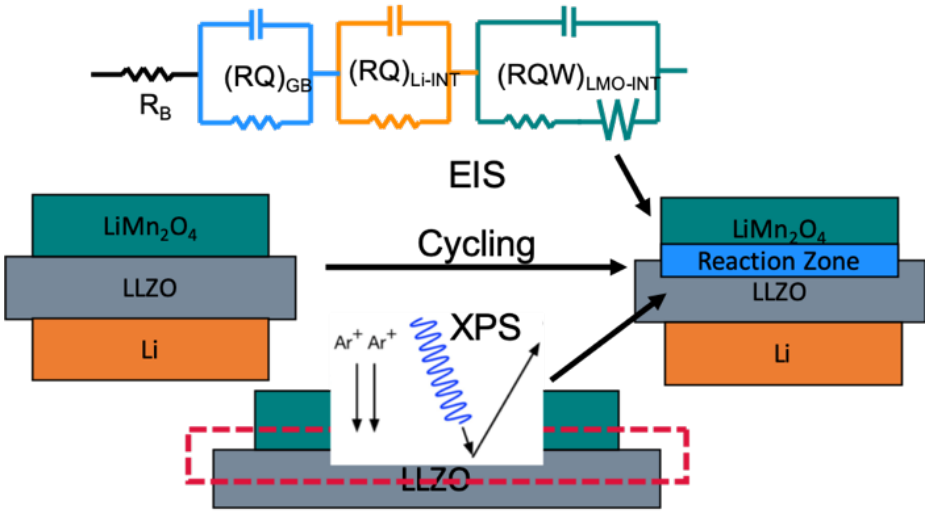

Figure 2.1. Graphical abstract depicting the effect of cycling on the LMO-LLZO interface as probed by XPS and EIS.

2.2 Introduction

Lithium batteries utilizing solid state electrolytes (SSEs) pose significant advantages over state-of-the-art Li-ion batteries, in terms of both safety and energy density. SSEs remove the need for flammable liquid electrolytes and associated safeguards, and they additionally hold the promise of enabling use of lithium metal anodes. However, solid state lithium batteries have not yet become widely commercially viable, with bulk conductivity and interfacial stability and impedance being primary hurdles.[28] Variables such as lattice mismatch, space charge distribution, and material interdiffusion or reaction can all play a role at both the cathode and anode SSE-interfaces,[71] and a greater understanding of the interplay between these phenomena is necessary to advance solid state battery technology.

Among lithium-conductive SSEs, $Li_7La_3Zr_2O_{12}$ (LLZO) has received much focus due to its good ionic conductivity (~10^{-4}-10^{-3} S/cm) and stability in contact with lithium

metal over a wide voltage window (~0-5V).[72–75] A growing body of research has characterized aspects of the anode (Li-metal) interface, addressing sources of impedance, overall stability, and dendritic growths.[30,34,75] Single crystal and neutron scattering studies have revealed that dendrites can still form in the absence of grain boundaries, and that contributions from electronic conductivity in LLZO may be a factor in their formation.[38,39,76] Nonetheless, lithium stripping and plating at this interface has been demonstrated without dendritic short-circuiting at current densities greater than 1 mA/cm^2 (one proposed threshold for a commercial solid state battery).[77,78], and Li-LLZO interfacial impedances of nearly zero Ohms have been achieved.[29] While there is still room for greater clarification, these studies highlight an increasingly firm understanding of the anodic LLZO interface. In contrast, the interface and compatibility of LLZO with various possible cathode insertion compounds has been investigated less extensively. One recent thermodynamic study has suggested that among a number of insertion compounds ($LiMn_2O_4$ (LMO), $LiFePO_4$ (LFP), $LiCoO_2$ (LCO), and $Li_4Ti_5O_{12}$ (LTO)), LMO may be the most stable against LLZO at room temperature.[79] Another study evaluated the electrochemical stability of $LiMnO_2$, LFP, and LCO with first-principles calculations and suggested LCO to have the lowest electrochemical driving force for interfacial decomposition.[50] This corroborates a recent experimental study of the thermal stability of these same three insertion electrodes, in which LCO tolerated the highest sintering temperature before interface decomposition phases were detected; however no polarization conditions were explored.[80,81] Several electrochemical studies have probed LCO

specifically,[43–46] including a detailed investigation by Vardar et al. using an array of synchrotron X-ray and other interface sensitive techniques to identify decomposition products between LCO and LLZO.[47] Studies of LFP cycling have shown limited capacity fade over 100 cycles, but without post-cycling chemical characterization.[82] In contrast, the high-voltage cathode $LiMn_{1.5}Ni_{0.5}O_4$ was reported to be un-cyclable with LLZO as the electrolyte[48], while variations of nickel-cobalt-manganese cathodes showed interfacial degradation due to both co-sintering[83] and electrochemical cycling.[84] The LMO-LLZO interface has been relatively unexplored, with only one study experimentally assessing the material's electrochemical operation over 3 cycles.[85] Thus, with a few exceptions, most cathodic interface studies to date have not taken the approach of combining electroanalytical techniques with interfacial chemical characterization to understand the effect of cycling.

For comparison, thin-film LMO cathodes have been more extensively explored with other electrolyte systems. These cathodes have shown excellent cycling performance in aprotic liquid electrolytes, as well the ability to be cycled at rates of 50C and upward.[86,87] More closely related to this study, LiPON-based all solid state batteries have shown a wide cycling window, and nanocrystalline LMO films (of the form $Li_xMn_{2-y}O_4$) have been stably cycled upward of 2000 times.[88] When utilizing the full voltage range available to these cells, capacities on the order of 270 mAh/g (LMO basis) have been observed.[89] Investigations into the charge transfer reaction at LMO|LiPON found the interface to have good stability, but also to have higher resistance than similar LCO-LiPON cells.[90]

In this contribution we investigate the LMO-LLZO interface using sputtered thin film LMO electrodes (i) to permit full-capacity cycling of a system with a high ratio of interface area to bulk volume, (ii) to remove the need for conductive additives and binders to probe only LMO-LLZO electrochemical interactions, and (iii) to facilitate access to the interface through ion milling.[81] We compare electrochemical impedance spectroscopy (EIS) of full cells (LMO | LLZO | Li) to symmetric cells (LMO | LLZO | LMO, Au | LLZO | Au, and Li | LLZO | Li) (**Figure 2.2 A-D**) in order to delineate impedance features that are specific to evolution of the cathode interface.

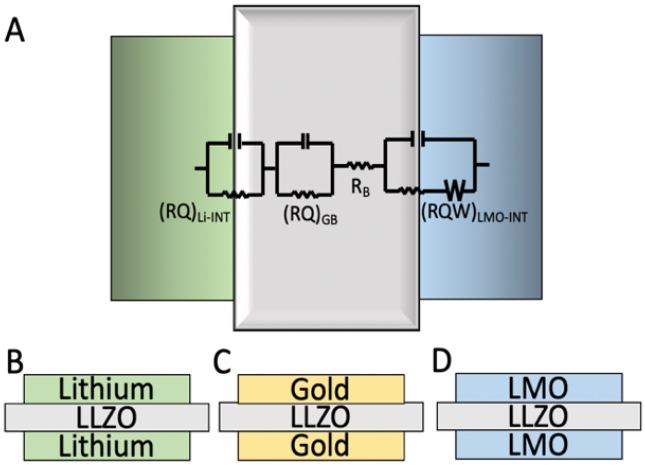

Figure 2.2 Cell architectures utilized for this study: (A) LMO | LLZO | Li, (B) Li | LLZO | Li, (C) Au | LLZO | Au, (D)LMO | LLZO | LMO. The EIS equivalent circuit model ultimately determined is overlaid on the full cell (A).

The interface is probed by EIS at two operating temperatures and further characterized before and after cycling using x-ray photoelectron spectroscopy (XPS) depth-profiling. We provide evidence of a limited interfacial reaction between LMO and LLZO at 100°C, which corresponds with an increase in the equivalent circuit

resistance of the LMO-LLZO interface as well as a capacity fade of ~30% during initial cycling of full cells.

2.3 Materials and Methods

2.3.1 Electrolyte Preparation

$Li_{6.4}La_3Zr_{1.4}Ta0_{.6}O_{12}$ (LLZTO) was purchased from MTI Corporation (μ_d = 5 μm) and pelletized in a 13 mm stainless steel die (Across International) at 2 metric tons of pressure using a mechanical press (Carver Model M). The resulting pellets were placed in MgO boats within a tube furnace (Thermcraft® XST-3-0-36-1V2-F01) for a two-step sintering process[91], which has been shown to help densify pellets while limiting lithium loss through an initial high temperature nucleation step and then lower temperature grain growth. Pellets were initially heated to 1200˚C at a ramp rate of 3˚C/min and held for 1 hour. The temperature was then reduced to 1100˚C and held for 5 hours before cooling to room temperature at a rate of 100˚C/hr. MgO boats

were used to eliminate the effect of crucible doping, and the resulting pellets (**Figure 2.3**) had approximate density of the pellets was 90±4%.

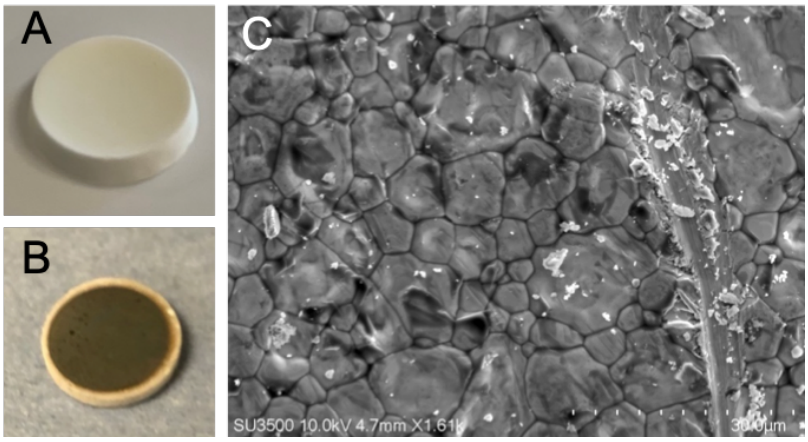

Figure 2.3 Photographs of sintered LLZO pellets before (A) and after (B) LMO depositon. Scanning electron microscopy image showing dense grain structure post-polishing.

The pellets showed no signs of contamination (**Figure 2.4**) by Mg from the boat.[92]

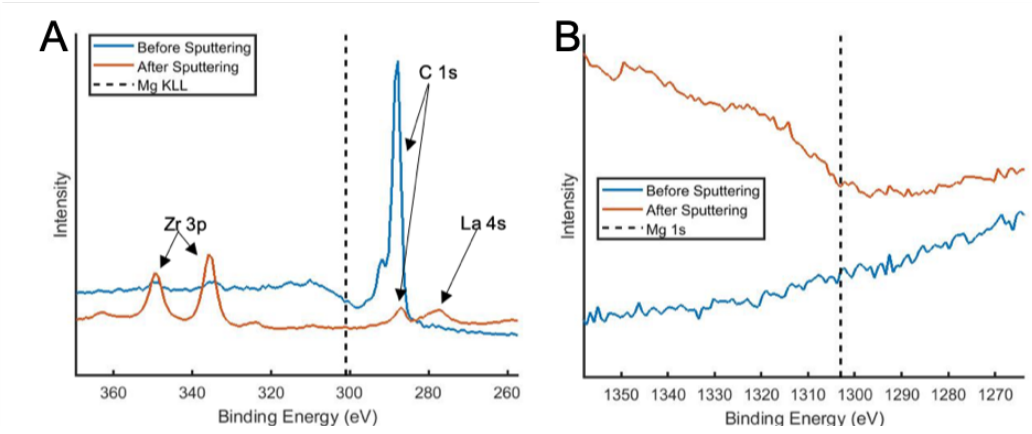

Figure 2.4 X-ray photoelectron spectroscopy spectra before and after sputtering showing no sign of Mg contamination by the MgO boat during sintering for Mg KLL (A) and Mg 1s (B)

X-ray diffraction data (XRD) for the sintered pellets agreed with the theoretical LLZTO structure (**Figure 2.5**).

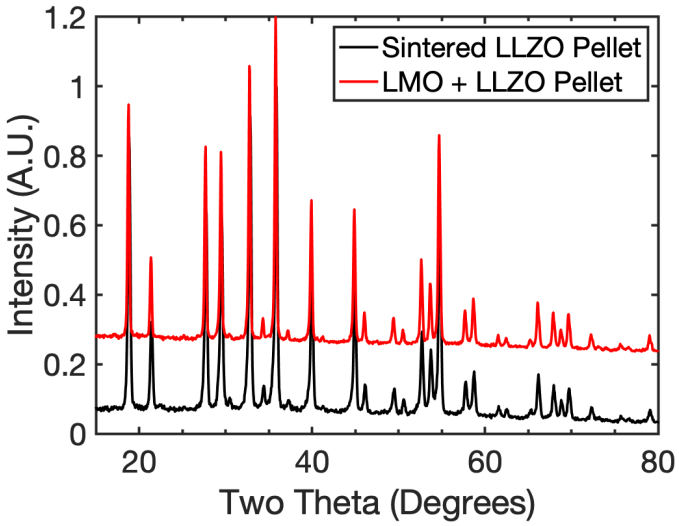

Figure 2.5 XRD of LLZO pellet before and after LMO deposition, the LMO is amorphous and is not detectable by XRD. The LLZO peaks agree with literature values; air exposure was necessary to conduct these measurements. One peak attributable to surface Li_2CO_3 is identifiable at 31˚.

The Faces of the pellets polished in air progressively with 150, 220, 400, 800, and 1000 grit sandpapers (3M®, proprietary ceramic), followed by wet polishing with 1, 0.3, and 0.05 µm alumina particles (Electron Microscopy Sciences) to ensure a flat surface for electrode deposition as well as reduce Li_2CO_3 contamination and then immediately transferred into an argon filled glovebox.[36]

2.3.2 Cathode Deposition

Pellets were transferred under argon to an RF-sputtering deposition chamber built within an argon-filled glove box (Angstrom Engineering, and LMO electrodes were deposited from a 2” LMO target (99.9% purity, ACI Alloys, Inc.). The sputter

deposition was carried out at 60W, 15 cm target distance, 15 sccm of argon flow. A stainless-steel shadow mask with 10 mm diameter circles was used to control where the deposition occurred on the LLZO pellets. Depositions were 2 hours per electrode, with an estimated deposition rate of 0.9 nm/min. The thickness of sputtered films was estimated to be 110 nm by atomic force microscopy (AFM) (**Figure 2.6**).

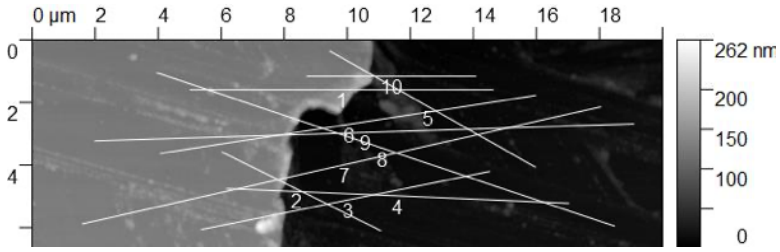

Figure 2.6 AFM image of as-deposited LMO on silicon wafer. The film thickness was determined by averaging the change in height of lines 1-10.

Further annealing was not performed due to prior evidence of reaction at ~500°C.[81] Gold current collectors were deposited using a 3-boat thermal evaporator (CVC SC-3000) onto the sputtered films using the same mask. Symmetric Au cell were synthesized using the same thermal evaporation procedure, but without the prior deposition of LMO.

2.3.3 Cell Assembly

The resulting LMO-LLZO pellets were transferred to a glovebox for cell assembly (MBRAUN® Unilab Pro SP, 0_2 <0.1 ppm, H_20 <0.5 ppm). For cells involving one or two lithium electrodes, lithium foils were punched (10 mm diameter), scraped to

remove oxide, pressed onto the LLZO pellet, and placed into customized Swagelok® cells (**Figure 2.7**).

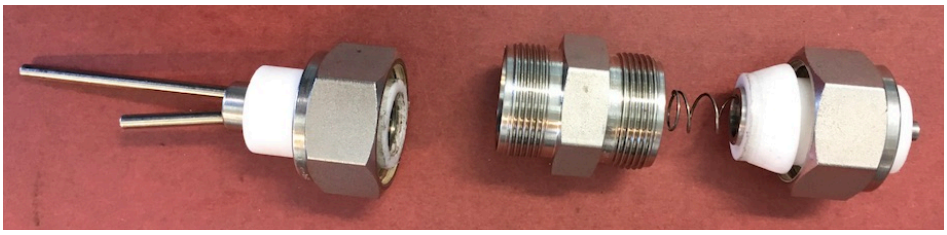

Figure 2.7. Photograph of Swagelok® cell used for electrochemical measurements.

A spring inside the cell is compressed against the anodic current collector and then tightened via the compression fitting of the cell, yielding about 36 kPa pressure. The cells were then heated to 170˚C for at least 12 hours,[31] then re-scraped to remove any newly-formed lithium oxide, which was recently shown to play a large role in the ability of Li metal to wet LLZO.[37] The re-scraping procedure was found to decrease the Li-LLZO interfacial impedance substantially and improve resolution of other impedance features. Symmetric LMO cells were subjected to the same temperature treatment as Li-containing cells for consistency. All electrochemical testing occurred under argon atmosphere in the same glovebox. A thermocouple was inserted into the Swagelok® cells to monitor temperature for elevated temperature operation within an oven (Black and Decker; CF110 - Across International). All electrochemical measurements were performed on a Bio-logic SP-300 potentiostat/galvanostat/FRA.

2.3.4 Materials Characterization

XRD data was obtained on a Bruker D2 Phaser. SEM images were taken using a JEOL JSM-7401F. XPS data was obtained on a Kratos AXIS Nova XPS system using a monochromated Al k-alpha source (1486.6 eV) and a pass energy of 160.0 eV. XPS binding energies were post corrected based on Au, Ag, and Cu foil calibrations. Depth profiling was carried out with Ar-ion milling with incident energy of 3 keV.

2.3.5 EIS Fitting

EIS data was fit within MATLAB® using equivalent circuit models and nonlinear least squares regression. CPEs were chosen to replace all capacitors within the system except for the blocking electrode capacitance in Au symmetric cells. Real cells include aspects such as electrode roughness and thickness variations which result in non-uniformity of the current distribution that basic capacitors cannot model. CPEs have been used for all capacitive elements in the fitting routines and have impedance described by (**Equation 2.1**).

$$(2.1)\ Z_{CPE} = \frac{1}{Q(j\omega)^N}$$

Warburg elements present in cells with lithium intercalation cathodes such as LMO are due to diffusion of lithium into the LMO particles with finite capacity and diffusion length. For RT cells, the standard Warburg element (**EQ. 2.2**), which represents diffusion that is effectively semi-infinite, was chosen, as it most closely resembled the observed impedance spectra.

$$(2.2)\ Z_w = R_d\left(\frac{1}{\sqrt{\omega}} + \frac{1}{j\sqrt{\omega}}\right)$$

For HT symmetric cell measurements, the finite length Warburg (FLW) was most appropriate, and is consistent with the derivation for a lithium ion diffusing into an intercalation particle. Due to the derivation of this element being for a singular particle rather than a thin-film electrode,[93] non-idealities are present which necessitate the use of dispersion parameters to achieve a good fit; the modified FLW element is given by (**EQ. 2.3**).

$$(2.3)\ Z_{FLW} = R_d \frac{\coth[(\tau_d j\omega)^{\frac{\alpha}{2}}]}{(\tau_d j\omega)^{\frac{\alpha}{2}}}$$

The non-idealities necessitating the use of dispersion parameters are the same that are commonly used to justify the use of CPEs in place of capacitors. Symmetric cells further exhibit diffusional behavior from electrodes at two different SOCs, also leading to mixed diffusional character and contributing to the need for dispersion parameters.

The initial assignment of equivalent circuit parameters to cell features was performed after 50 cycles for all cycled cells, as we found that certain features became more visible and stable after a few break-in cycles. We then fit the cycles in reverse order using the fitting result from one cycle as the initial guess for the next (prior) cycle. For some data sets, such as the HT Au|LLZO|Au cells, we opted to fit a truncated frequency range to achieve a more accurate fit of the most relevant elements. In the case of the HT Au|LLZO|Au cells, this was because the capacitance of the blocking electrode dominated the lower frequency range, while the goal for this system was to study grain boundary effects in the electrolyte bulk. For most measurements the very high frequency range (>300kHz) had inductive effects (likely

related to mutual inductance in leads needed for the cell design), and so spectra were also truncated at this limit.

2.4 Results and Discussion

Before discussing the LMO-LLZO interface specifically, we first highlight the major features of polarization curves for the full, thin film batteries using LMO as a cathode. LMO-LLZO-Li full cells were cycled galvanostatically between cell potentials from 2-4 V at both room temperature (RT, 23 ± 2°C) and 100˚C (HT, 100 ± 2°C). The voltage profiles, shown in **Figure 2.8A** (HT) and **Figure 2.8J** (RT), were consistent with sputter-deposited LMO, where the low crystallinity of the deposited films results in a continuous variation of cell voltage.

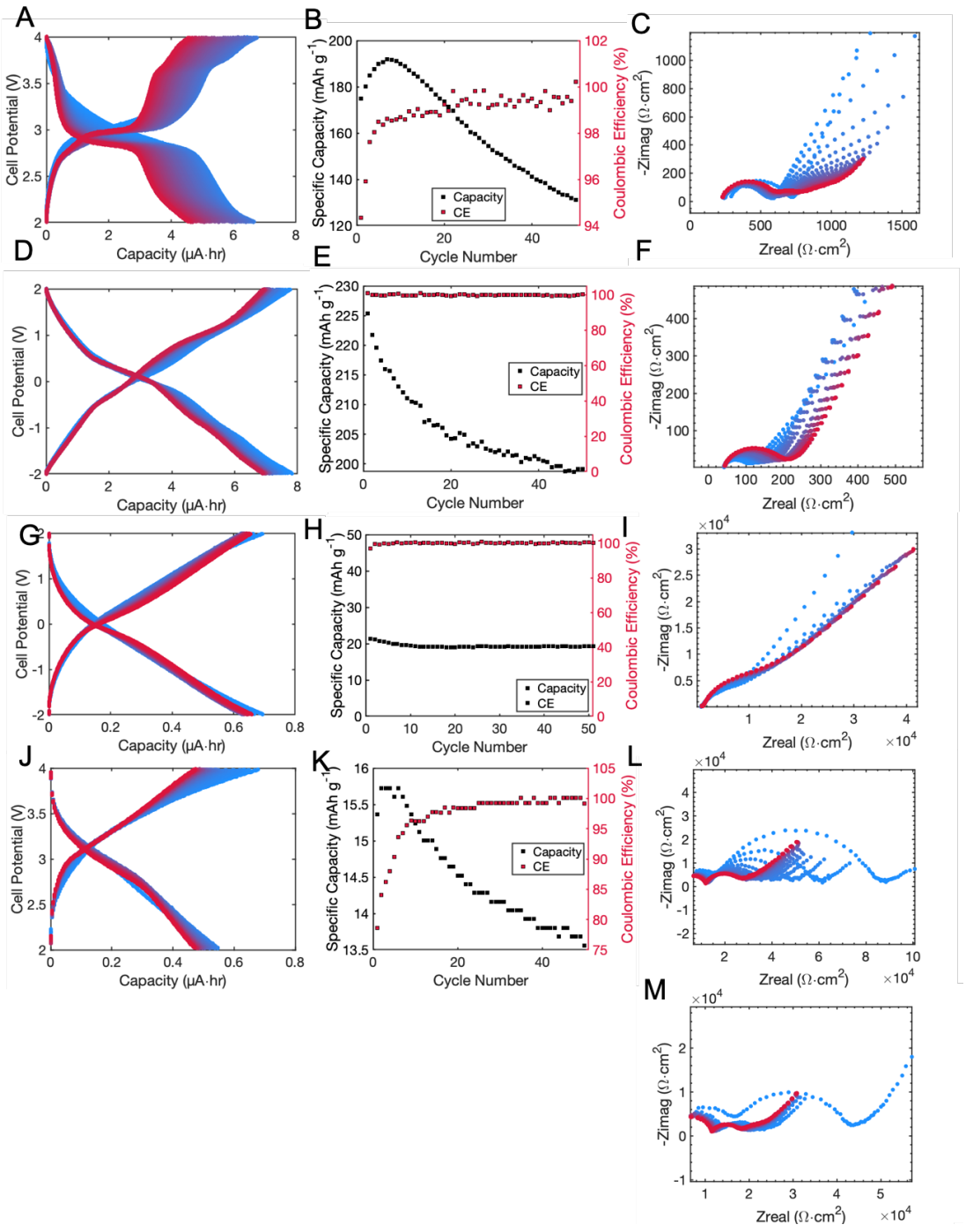

Figure 2.8. Polarization curves, discharge capacities and coulombic efficiencies, and EIS evolution over 50 cycles at 100°C for: LMO | LLZO | Li cells (A-C) and LMO | LLZO | LMO cells (D-F). Blue curves represent initial cycle and transition toward red, representing the 50th cycle. All cycling was performed at 3.8 μAhr/cm^2 and is shown beginning on the charging phase after an initial discharge from 50% SOC (as synthesized).

This is in contrast to behavior of crystalline LMO, which shows two well-defined voltage plateaus at roughly 2.9 V and 4.0 V.[7,94] During initial cycles, HT cells accessed 172 ± 13.5 mAh/g (~64% of their theoretical capacity), shown in **Figure 2.8B**. In contrast, RT cells showed very low capacity (8.83 ± 6.01 mAh/g, ~3% of theoretical, **Figure 2.8K**). Here, theoretical capacities are estimated using the specific capacity of crystalline LMO (285 mAh/g), electrode thickness, and the area of the electrodes. Thus, the estimates presented are conservative, as the films should exhibit lower density than bulk LMO. Over the subsequent course of 50 cycles, HT cells lost 25±8.5% of their maximum capacity, while RT cells experienced negligible capacity fade. The low capacity of the RT cells is due to high cell impedance, dominated by the Li-LLZO interface. Briefly, we note that charge and discharge correspond to plating and stripping at the Li anode, respectively. During stripping, the interface can form voids that increase the impedance. Utilizing higher pressures and temperatures can better maintain and replenish interfacial contact,[29,32,95] but such effects are tangential to the current study of the LMO interface. It may also be noted that Li and LLZO have previously been shown to be kinetically stable against reaction in the operating range of 0-5V.[72–75]

To isolate features associated with the LMO-LLZO interface, symmetric cells were constructed with the architecture LMO|LLZO|LMO. Cycling of these LMO symmetric cells was performed between +/-2 V (cell potential), which should approximately correspond to 2-4 V vs Li/Li^+. This range is approximate because both LMO electrodes shift in potential with charge passage, and the shifts are not identical

above and below the OCV. However, the range of 2-4 V is a fair point of reference as estimated by the similar capacities for the symmetric and full cells and the measured OCV of ~3 V (vs Li/Li^+) for as-synthesized LMO in the full cell configuration. This voltage window corresponds to lithium content approaching x=0 within the accessible portion of $Li_xMn_2O_4$ at one electrode while approaching x=2 at the opposing electrode, and vice versa, thus making the theoretical symmetric cell capacity equivalent to the full cell capacity.

As shown in Figure **2.8D**, symmetric LMO cells accessed up to 75% of their theoretical capacity (average initial specific capacity of 193 ± 22.8 mAh/g) at HT, while at RT they accessed only ~7% (**Figure 2.8H**). Capacity fade was approximately 11% at HT and 1% at RT over 50 cycles (**Figure 2.8D and Figure 2.8H**). The differences in accessible capacity between RT and HT cells are associated with a decrease in polarization resistance by roughly a factor of ~100 at elevated temperature, which can be seen in Nyquist plots at early cycle numbers (**Figure 2.8F & Figure 2.8I**). We found that HT cells could be cycled at a rate of > 10C with limited decrease to the accessed capacity, but for more direct comparison between temperatures, all cycling was carried out at C/3. Polarization curves for cycling at higher discharge rates and corresponding can be found in **Figure 2.9A**.

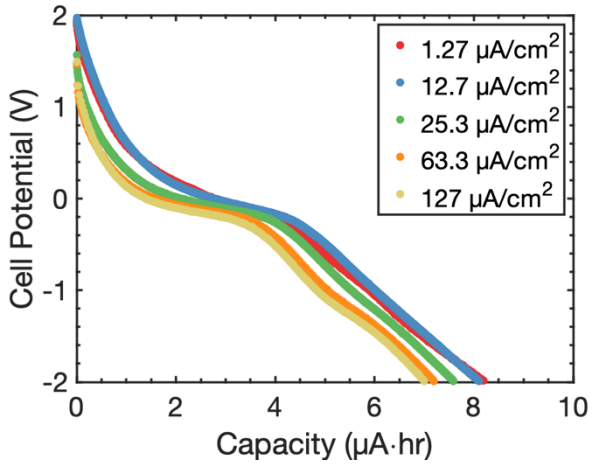

Figure 2.9. Discharge capacity for LMO symmetric cells at rates ranging from ~C/10 to >10C.

EIS measurements on the symmetric LMO cells were repeated at the start of each half cycle, and did not substantially vary when compared at different depths of charge/discharge (**Figure 2.10**).

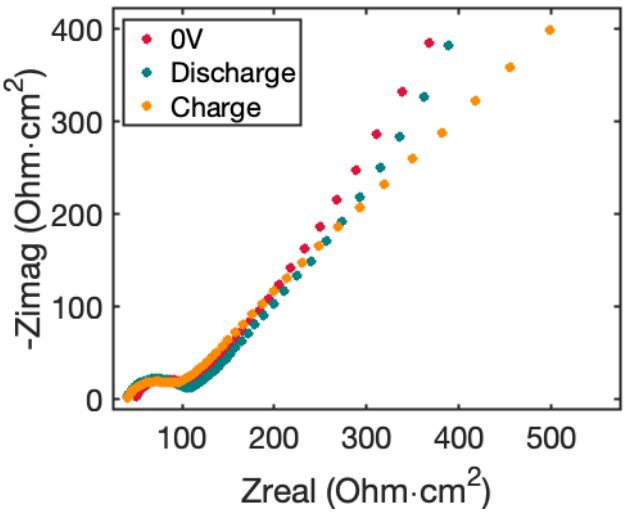

Figure 2.10 Comparison of cell impedance measured at 0, +2, -2 V for symmetric cells

An increase in the overall cell impedance was observed with cycling for both the RT (**Figure 2.8I)** and HT **(Figure 2.8F**) symmetric cells. The corresponding evolution of the impedance spectra is discussed below in the context of the relevant physical conduction processes and equivalent circuit models.

Equivalent circuit models for all cells and operating conditions were determined by a combination of phase inflection detection (PID) analysis[96,97], characteristic time scale assessment, and comparison between full and symmetric cells with common components. Each circuit model comprises resistors (R) and constant phase elements (Q) —the parallel combination of which is generally attributed to one specific interfacial process and time constant—as well as generalized Warburg (W) elements to model diffusion-controlled processes. PID analysis utilizes changes in the slopes of impedance phase angle vs. frequency (derivatives of the Bode plots) to aid in identifying distinct processes that merit an equivalent circuit component; inflection points in the phase angle become maxima or minima in the derivative and are more easily detected than corresponding features in the imaginary component of impedance. For our electrolyte and electrode dimensions (area = 0.79 cm^2; A/L = 7.9 cm), documented capacitance values for bulk, grain boundary, and interface impedances should generally be on the order of ~10^{-11} F, ~10^{-10}-10^{-7} F, and ~10^{-7}-10^{-5}F, respectively.[98] These estimates are used throughout the proceeding discussion to support the assignment of the individual circuit elements.

An initial comparison between LMO symmetric, Li symmetric, and LMO-Li full cells permits identification of several EIS features that appear on differing time scales. Inspection of the Nyquist diagrams (**Figure 2.11**) shows the presence of distinct (though depressed) semicircle features associated with each LMO symmetric cell, both of which are resolvable in the spectra of the full cell.

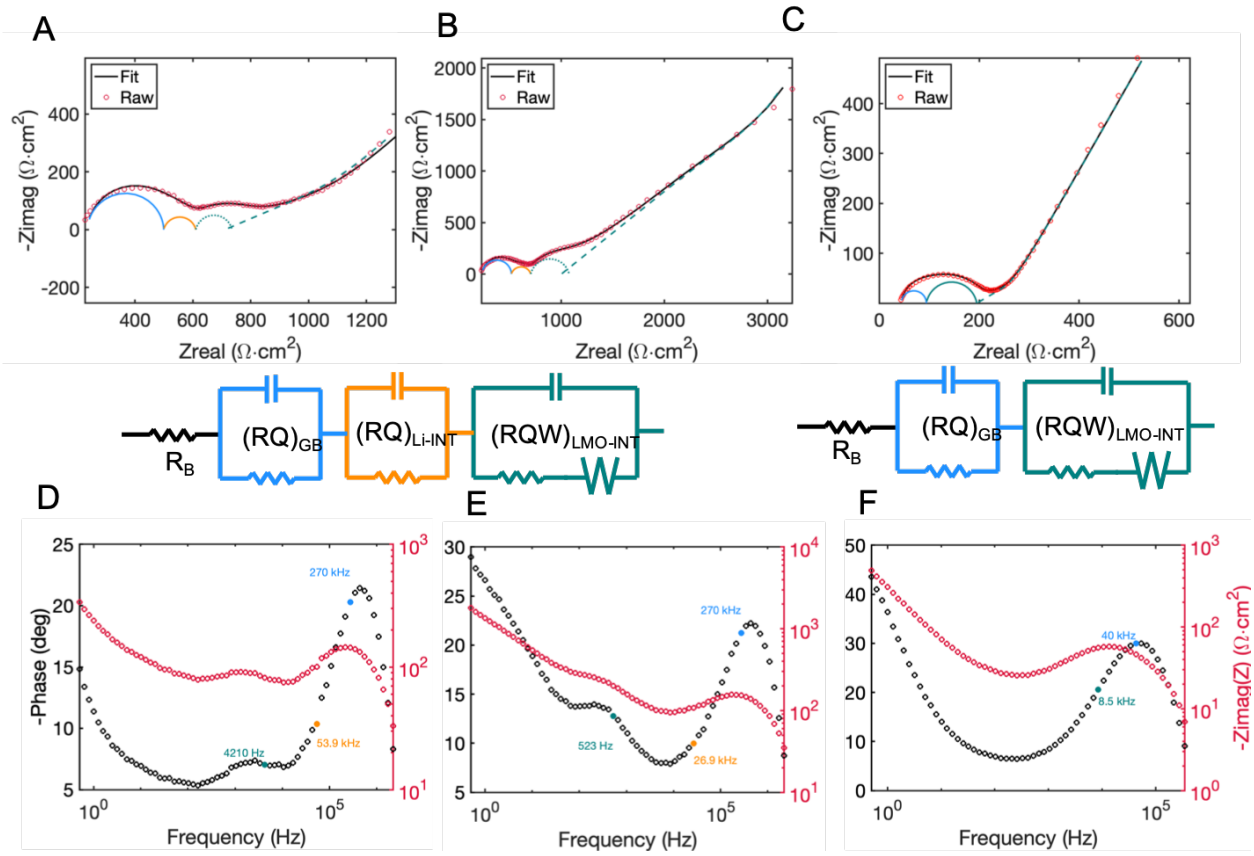

Figure 2.11. Polarization curves, discharge capacities and coulombic efficiencies, and EIS evolution over 50 cycles at 100°C for: LMO|LLZO|Li cells (A-C) and LMO|LLZO|LMO cells (D-F). Blue curves represent initial cycle and transition toward red, representing the 50th cycle. All cycling was performed at 3.8 μAhr/cm^2 and is shown beginning on the charging phase after an initial discharge from 50% SOC (as synthesized).

A singular depressed semicircle to the high-frequency semicircle in full cells also appears in the Li symmetric cells (**Figure 2.12B**).

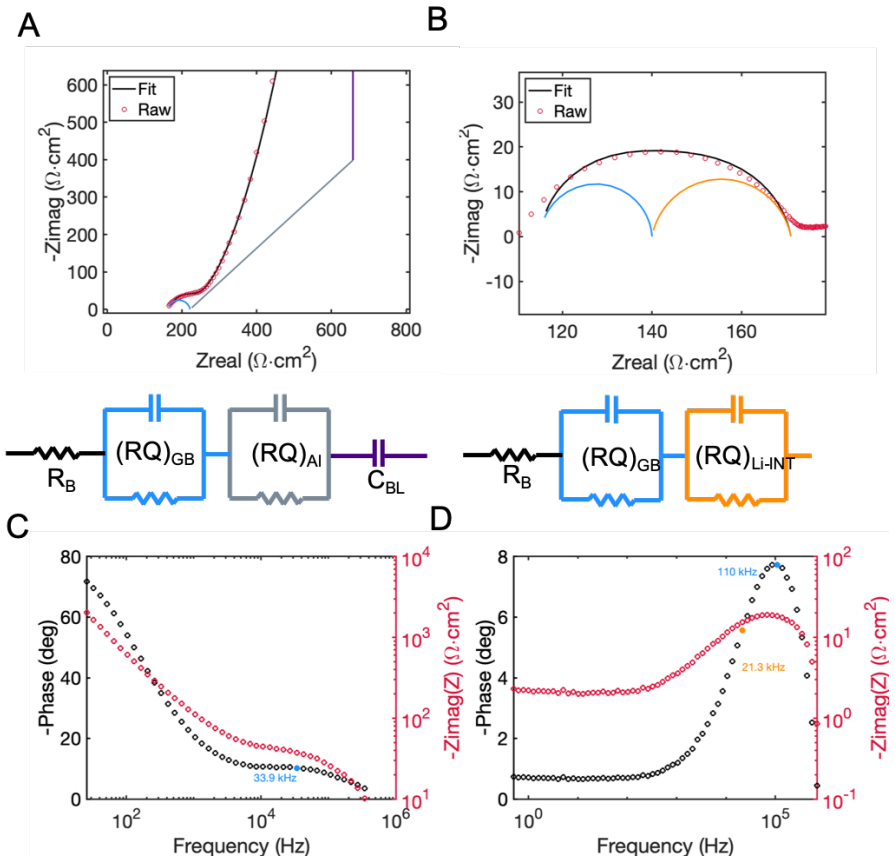

Figure 2.12. Nyquist and Bode plots for Au Symmetric (A&C) and Li Symmetric (B&D) cells at HT with the equivalent circuits used for fitting their EIS.

Warburg (diffusional) tailing is also clear in the low-frequency regime of both the symmetric LMO and full cells, indicating that it must arise from diffusion in LMO. However, to more definitively make equivalent circuit assignments, we also constructed ion-blocking cells (Au | LLZO | Au) to afford insight into the (intragranular) bulk and grain boundary impedance of the electrolyte, which could in principle overlap high frequency processes associated with the primary electrode

materials. The Au symmetric EIS studies revealed two RC-processes, as well as a capacitive effect due to the blocking electrodes, resulting in the equivalent circuit shown in **Figure 2.12A**. We attribute the higher-frequency process to the grain boundaries, consistent with its fit capacitance on the order of 10^{-7} F. The lower-frequency process (capacitance on order of 10^{-4}F) has previously been observed at least once to our knowledge, although was not identified.[99] We suspect it is due to a slight alloying of lithium with gold, consistent with increased resolution of the feature at high temperature and its fit capacitance value suggesting chemical reaction.[98]

Informed by the independent measurement of grain boundary impedance, further interpretation of the symmetric Li, symmetric LMO, and LMO | LLZO | Li full cell EIS can be made. The semicircle noted in the Nyquist plots of LMO symmetric cells (**Figure 2.11C**) is highly depressed, which generally indicates the presence of multiple processes, rather than the alternative of an extremely non-ideal capacitive feature (low CPE exponent).[100] Combined with the Warburg tailing at low frequency, these features were fit with RQ and RQW circuits, placed in series, to capture grain boundary impedance and the electrode-electrolyte interface respectively. The fitted capacitances of these elements were, respectively, on the order of 10^{-8} and 10^{-7} F. Due to the high fraction of theoretical capacity that was accessible at HT, the low frequency diffusion was modeled by a finite-length Warburg Open element (representing diffusion toward a reflective boundary), as is frequently invoked for intercalation materials.[101] Intercalation electrodes are known to exhibit diffusion that is linked to charge-transfer, and thus the finite Warburg element is placed in

series with the resistance while parallel to the capacitance for the best physical correspondance.[97] The same essential process and circuit were also used to fit the EIS from RT LMO symmetric cells, except that the finite Warburg element at HT was replaced by a standard Warburg element at RT, where much higher diffusion resistance effectively creates a semi-infinite boundary condition. The specifics related to the Warburg impedance functions were discussed in section 2.3.5.

To compare cycle-dependent EIS of the Li-LLZO interface, lithium symmetric cells were cycled at 7.6 μA/cm^2 for one hour, to 6μA-hr capacity in each direction, to best approximate capacities relevant for the Li-LLZO interface in full cells at HT. EIS measurements were performed at the end of each half-cycle. The impedance response **Figure 2.12B** showed a primary, depressed Nyquist semicircle attributable to the series impedance of grain boundaries and the Li-LLZO interface, which exhibit reasonable fit capacitance values of 10^{-8} and 10^{-6} F (equivalent circuit in **Figure 2.12B**).

Equipped with equivalent circuit information for the bulk materials and both interfaces, the full cell EIS could then be evaluated. The highest frequency, stretched semicircle of the full cell impedance spectra (**Figure 2.11A**) was assigned to the combination of grain boundaries and the Li-LLZO interface, in accordance with their fit capacitance values of 10^{-9} F and 10^{-7} F, respectively. The second semicircle and subsequent diffusional (Warburg Open) response were attributed to the LMO-LLZO interface likewise through value and agreement of the fit capacitance (10^{-6}-10^{-7}F) with the symmetric cell data. Fitting of the EIS of the full cells at room

temperature mirrored the above procedure for the high temperature data. However, because the impedance of the full cells at was found to be dominated by the Li interface at lower temperature, the fitting does not provide insight into the LMO-LLZO interface under these conditions. Increasing the stack pressure of future cells may resolve this difficulty and permit interpretation at lower temperatures.[32,95]

Having constructed the overall equivalent circuit diagrams, the LMO full cells and LMO symmetric cells were fit iteratively over the course of cycling to track the evolution of the cell components. **Figure 2.13A-C** shows representative impedance spectra for a discharged full cell as well as for symmetric cells at both RT and HT.

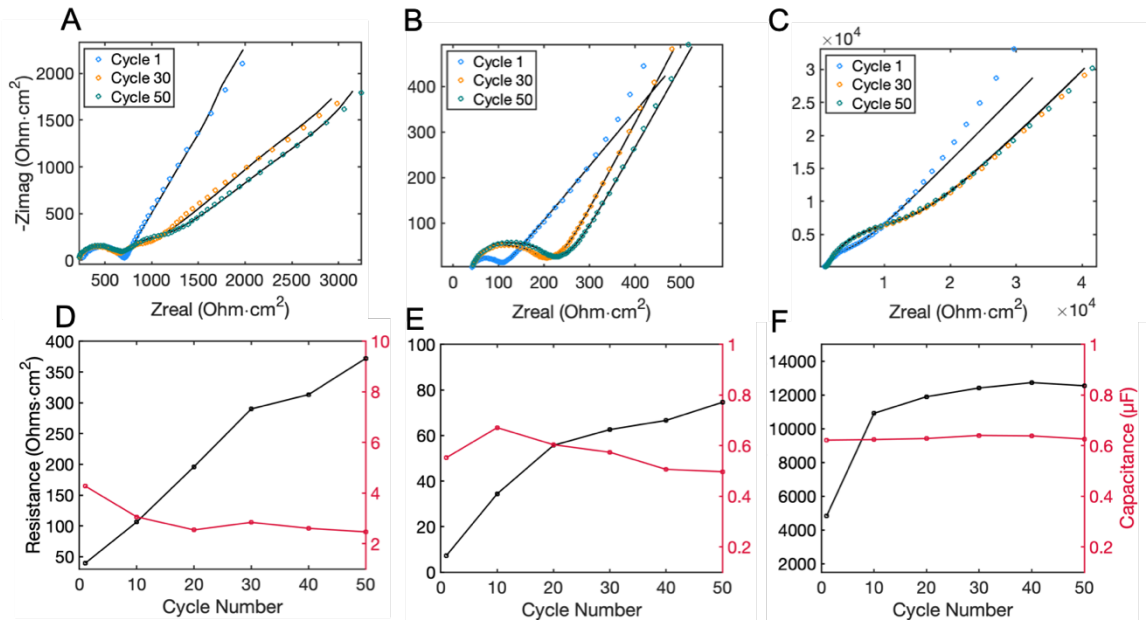

Figure 2.13. Nyquist plots (top), equivalent circuits (middle inset), and bode plots (bottom) for LMO-containing cells tested at 100°C in this study: (A)LMO | LLZO | Li post-charge, (B) LMO | LLZO | Li post-discharge, (C) LMO | LLZO | LMO

Below these (**Figure 2.13D-F**) are shown the tracked values of the resistance and capacitance associated with the LMO-LLZO interface in each cell; complete sets of circuit element parameter values for each model are presented in **Tables 2.1-2.5**.

Table 2.1. Fitting values for HT LMO symmetric cell at selected cycles.

Cycle	R1	R2	C2	N2	R3	C3	N3	R_D	Tau	Alpha
50	4.62E+01	7.46E+01	6.46E-08	9.99E-01	7.46E+01	4.97E-07	9.53E-01	1.74E+02	5.67E-02	6.75E-01
40	4.59E+01	7.17E+01	6.55E-08	1.00E+00	6.66E+01	5.07E-07	9.58E-01	1.68E+02	5.70E-02	6.86E-01
30	4.64E+01	7.04E+01	6.64E-08	1.00E+00	6.26E+01	5.74E-07	9.52E-01	1.67E+02	5.83E-02	6.94E-01
20	4.71E+01	6.78E+01	6.75E-08	1.00E+00	5.57E+01	6.04E-07	9.56E-01	1.70E+02	6.15E-02	7.01E-01
10	4.45E+01	5.39E+01	7.78E-08	1.00E+00	3.44E+01	6.71E-07	9.70E-01	1.46E+02	5.44E-02	7.15E-01
1	4.47E+01	3.55E+01	1.11E-07	1.00E+00	7.29E+00	5.53E-07	1.00E+00	7.44E+01	8.67E-03	5.56E-01

Table 2.2. Fitting values for a RT LMO symmetric cell at selected cycles.

	Cycle	R1	R2	C2	N2	R3	C3	N3	R_D
Charge	50	1.02E+03	4.04E+02	1.78E-06	6.41E-01	1.26E+04	6.26E-07	7.89E-01	5.38E+04
	40	1.04E+03	4.05E+02	1.91E-06	6.36E-01	1.27E+04	6.39E-07	7.86E-01	5.31E+04
	30	1.04E+03	4.17E+02	2.20E-06	6.26E-01	1.24E+04	6.40E-07	7.86E-01	5.16E+04
	20	1.03E+03	4.30E+02	2.08E-06	6.29E-01	1.19E+04	6.28E-07	7.89E-01	4.97E+04
	10	1.03E+03	4.59E+02	2.54E-06	6.11E-01	1.09E+04	6.24E-07	7.92E-01	4.75E+04
	1	9.17E+02	3.00E+02	7.45E-07	7.22E-01	4.83E+03	6.22E-07	7.95E-01	5.20E+04
Discharge	Cycle	R1	R2	C2	N2	R3	C3	N3	R_D
	50	1.02E+03	3.53E+02	2.16E-06	6.32E-01	1.32E+04	8.05E-07	7.57E-01	3.39E+04
	40	1.04E+03	3.50E+02	1.93E-06	6.41E-01	1.33E+04	8.11E-07	7.55E-01	3.48E+04
	30	1.04E+03	3.54E+02	1.69E-06	6.54E-01	1.26E+04	7.84E-07	7.60E-01	3.51E+04
	20	1.03E+03	3.90E+02	2.44E-06	6.22E-01	1.18E+04	7.74E-07	7.64E-01	3.54E+04
	10	1.03E+03	4.59E+02	2.89E-06	6.05E-01	1.00E+04	7.12E-07	7.78E-01	3.59E+04
	1	8.99E+02	3.00E+02	9.01E-07	7.13E-01	4.96E+03	9.51E-07	7.56E-01	2.81E+04

Table 2.3. Fitting values for an HT full cell at selected cycles.

Charge													
Cycle	R1	R2	C2	N2	R3	C3	N3	R4	C4	N4	R_D	Tau	Alpha
50	2.35E+02	2.64E+02	3.26E-09	9.69E-01	1.11E+02	1.83E-07	8.50E-01	1.25E+02	1.38E-06	8.58E-01	9.55E+02	1.66E+00	5.13E-01
40	2.36E+02	2.46E+02	2.67E-09	9.83E-01	1.16E+02	9.23E-08	8.91E-01	9.74E+01	1.31E-06	8.55E-01	1.07E+03	2.81E+00	5.05E-01
30	2.40E+02	2.27E+02	2.13E-09	1.00E+00	1.09E+02	4.44E-08	9.39E-01	8.17E+01	1.05E-06	8.56E-01	1.31E+03	5.37E+00	5.17E-01
20	2.40E+02	2.12E+02	2.21E-09	1.00E+00	1.01E+02	3.66E-08	9.48E-01	7.15E+01	9.36E-07	8.55E-01	1.64E+03	7.13E+00	5.74E-01
10	2.44E+02	1.94E+02	2.28E-09	1.00E+00	8.71E+01	2.02E-08	1.00E+00	6.24E+01	5.66E-07	9.01E-01	2.41E+03	4.62E+00	7.66E-01
1	2.92E+02	1.86E+02	2.45E-09	1.00E+00	2.14E+02	7.87E-08	8.43E-01	4.52E+01	2.56E-06	9.38E-01	1.00E+04	1.31E+00	1.41E+00
Discharge													
Cycle	R1	R2	C2	N2	R3	C3	N3	R4	C4	N4	R_D	Tau	Alpha
50	2.34E+02	2.83E+02	3.03E-09	9.71E-01	1.88E+02	2.90E-07	8.13E-01	3.72E+02	2.47E-06	8.50E-01	6.52E+03	1.97E+00	8.62E-01
40	2.36E+02	2.47E+02	2.29E-09	9.95E-01	2.10E+02	3.43E-07	7.72E-01	3.13E+02	2.61E-06	8.50E-01	7.10E+03	2.56E+00	8.74E-01
30	2.35E+02	2.35E+02	2.21E-09	1.00E+00	2.01E+02	3.40E-07	7.70E-01	2.90E+02	2.84E-06	8.54E-01	7.10E+03	2.51E+00	9.10E-01
20	2.39E+02	2.23E+02	2.32E-09	1.00E+00	1.71E+02	3.22E-07	7.74E-01	1.96E+02	2.55E-06	8.54E-01	7.06E+03	1.77E+00	9.96E-01
10	2.42E+02	2.22E+02	3.34E-09	9.80E-01	1.34E+02	1.52E-06	6.76E-01	1.06E+02	3.06E-06	8.61E-01	7.61E+03	1.20E+00	1.18E+00
1	2.77E+02	2.49E+02	5.84E-09	9.36E-01	1.47E+02	1.51E-07	8.34E-01	3.93E+01	4.28E-06	8.54E-01	1.00E+04	2.50E+00	1.32E+00

Table 2.4. Fitting values for a RT full cell at selected cycles.

	R1	R2	C2	N2	R3	C3	N3	R_D	Tau	Alpha
Discharge Cycle 50	1.50E+03	1.02E+04	3.59E-11	9.31E-01	9.78E+03	1.07E-08	8.89E-01	3.31E+04	5.17E-01	5.04E-01
Charge Cycle 50	1.50E+03	9.58E+03	2.22E-11	9.62E-01	6.00E+03	3.06E-08	8.23E-01	2.84E+04	1.67E+00	6.36E-01

Table 2.5. Fitting values for Au and Li symmetric cells

	R1	R2	C2	N2	R3	C3	N3	C
HT AU	1.62E+02	5.95E+01	3.55E-07	8.78E-01	2.37E+05	1.53E-04	4.73E-01	3.82E-06
RT AU	1.16E+03	9.62E+03	4.36E-07	7.51E-01	6.14E+04	6.75E-06	6.17E-01	2.76E-06
HT Li	1.15E+02	2.50E+01	9.50E-08	9.60E-01	3.10E+01	1.00E-06	8.80E-01	X
RT Li	8.14E+02	1.44E+03	2.20E-10	8.71E-01	3.08E+03	1.83E-07	7.28E-01	X

The difference in magnitude of interfacial resistances between the HT and RT cells is due to a reduction of this resistance with increasing temperature, while changes over time in each dataset correspond to evolution within the cell. The primary quantifiable conclusion of these results is that the LMO-LLZO interfacial resistance (R_{CT}) increases steadily over time while the associated interfacial capacitance (Q_{CT}) stays relatively constant (**Figure 2.13D-F**). This is a critical observation because if an increase in resistance were due to a decrease in contact area, one would expect a corresponding decrease in capacitance as well. Instead, the minor observed change in Q_{CT}, coupled with growth in R_{CT}, indicates that the interfacial area of the LMO electrodes remains relatively constant, suggesting increases in the resistance are due to fundamental changes in the nature of the interface, such as the formation of a less-conductive interfacial decomposition product. This effect is present in cells cycled at both temperatures, although changes are much more pronounced and grow continuously in the HT cells.

To further investigate the possibility of interfacial products between LMO and LLZO, we performed XPS depth profiling[45,47] on cells before and after cycling. We present the depth profiles by fractional signal contribution, defined as $I_A/(I_A+I_B)$, where I is the integrated XPS signal intensity, for elemental pairs. This metric illustrates changes to the relative quantity of each element spanning across the interface between each bulk phase. **Figure 2.14** shows depth profiles for Mn, La, and Zr in the RT (A) and HT (B) cycled cells, overlaid on a control sample that was subjected to the same pretreatment (170˚C) as the cycled cells.

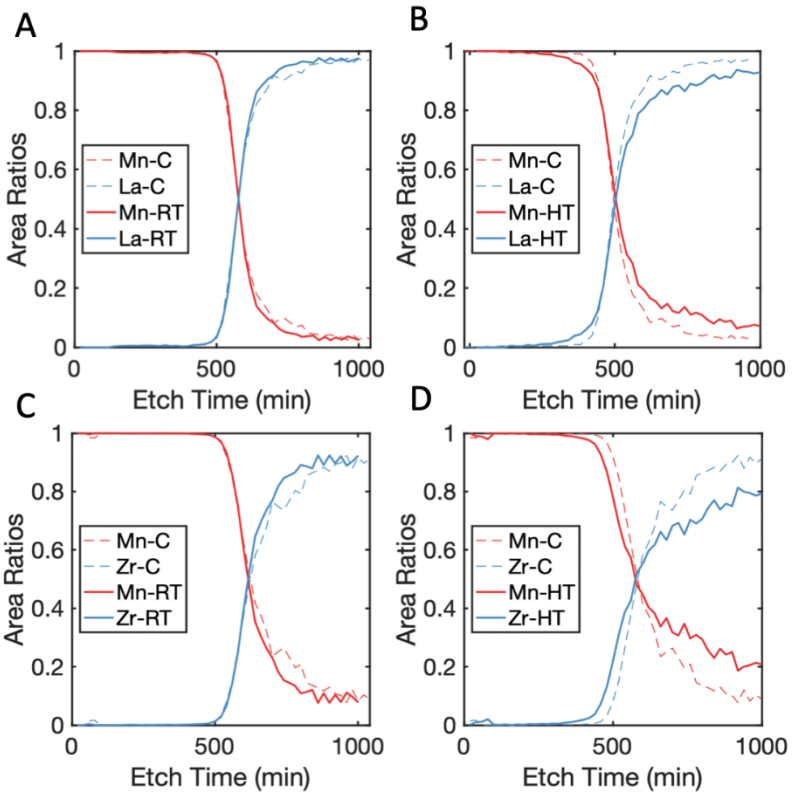

Figure 2.14. XPS depth profiles taken after cycling at RT (A,C) and HT (C-D), overlaid on uncycled control depth profiles for selected pairs of elements. Data is presented as fractional signal contribution amongst the elements compared. (A-B) Mn $2p_{3/2}$ vs. La $3d_{5/2}$, (C-D) Mn $2p_{3/2}$ vs. Zr 3d.

To minimize possible artifacts from small differences in film thicknesses and etch rates, the profiles are aligned to the point at which the elemental signal contributions are equal. Changes in the spatial extent of an elemental signal must then be related to interdiffusion (barring large variance in interfacial roughness between samples). Consistency between control samples and the profiles of several apparently-immobile elements gives indication that interfacial roughness was reproducible, and thus that changes to the spatial distributions can be attributed to element migration.

A clear difference in the interfacial composition profile is observed between the cell cycled at high temperature and the uncycled cell. The concentration profiles at elevated temperature specifically suggest migration of Mn atoms and thus the likely formation of a reaction zone penetrating into the electrolyte side of the interface. The RT cell experienced far less Mn diffusion, but this is not surprising both due to the inherently slower kinetics at low temperature as well as the significantly lower accessible capacity, which results in passage of much less total charge during cycling. Since cycling at high temperature results in a greater extent of interdiffusion than heat treatment alone (control sample), we hypothesize that the same decomposition behavior may be exhibited at low temperature over substantially longer cycling periods. The full elemental spectra for species profiled in **Figure 2.14** are shown in **Figure 2.15.**

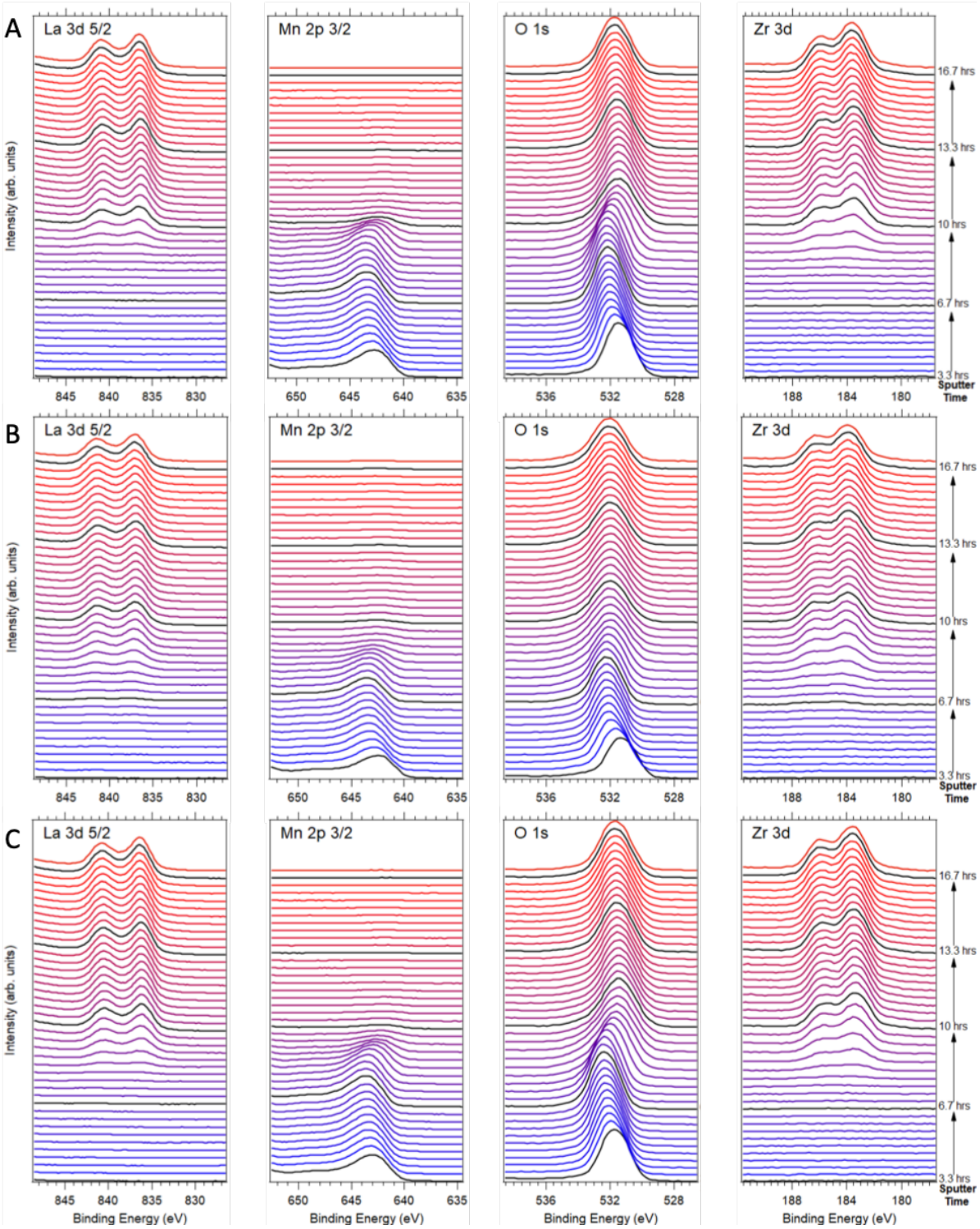

Figure 2.15. XPS spectra for La 3d 5/2, Mn 2p 3/2, O 1s, and Zr 3d core levels as a function of depth for (A) RT cycled, (B) HT cycled, and (C) control samples he HT cycled sample (B), shows less variability in charging especially when entering the

LLZO layer. The comparison is most clear in the O 1s core level because oxygen is in both the LMO and LLZO.

However, due to well-documented complications of selective sputtering (inherent in all depth profiles), as well as evidence of sample charging, we do not assign a specific chemical state or phase to the reaction product(s) at this time.[102–104]

It is noteworthy that in the full composition profiles for all elements monitored (La, Mn, O, C, Zr, Li, Au), all samples show a spike in the concentration of oxygen at the interface (**Figure 2.16**).

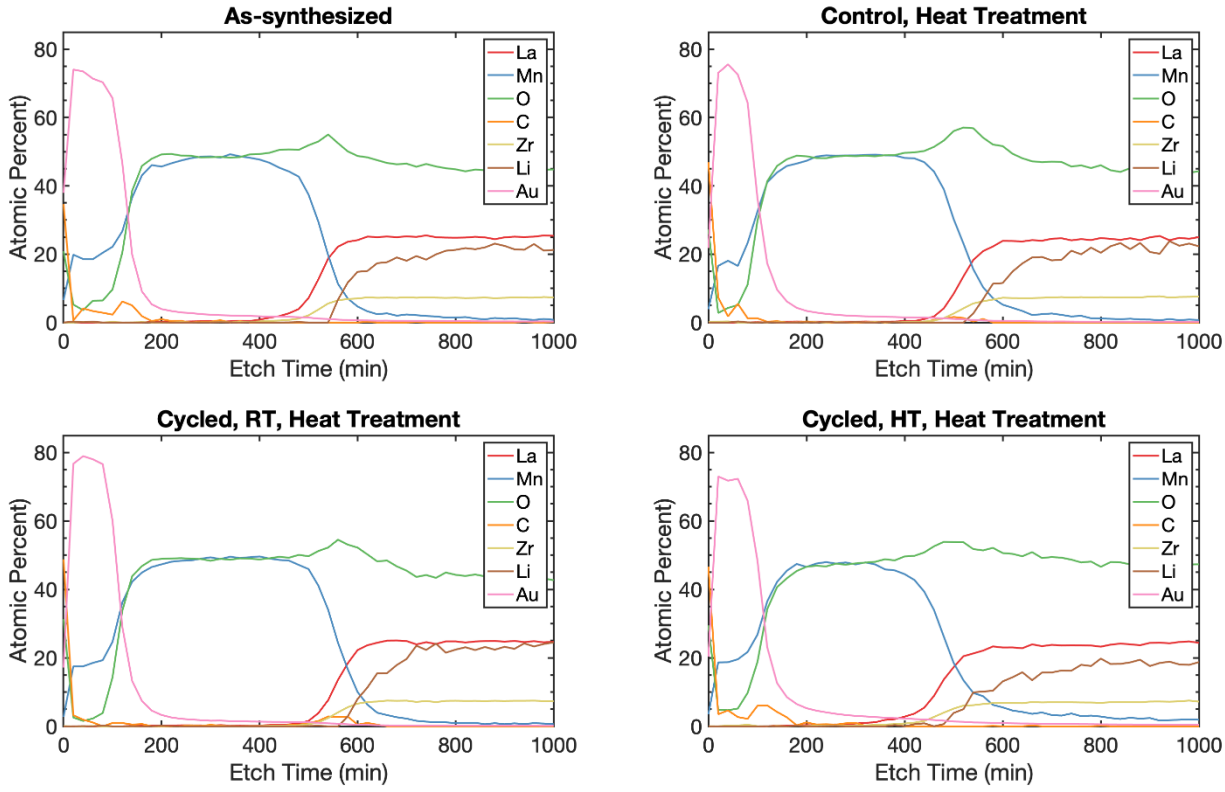

Figure 2.16. XPS depth profiling data for all tracked elements. Note that comparisons should only be made on qualitative basis due to differential sputtering as well as Li loss from the cathode phase due to sample charging.

The feature could possibly relate to different metal oxide stoichiometry, but could also relate to Li_2CO_3 contamination, which is a well-documented issue for LLZO upon any brief atmospheric exposure.[47,105,106] The carbon signal was tracked for these samples as well and did reveal the possible presence of Li_2CO_3, though there was not a clear correlation between C and O signals. Thus, while better polishing and handling protocols could be implemented to further reduce such sources of ambiguity, the present data are still consistent with a reaction between the electrode and electrolyte metal oxides.

Regarding the possible identity of products, precise phase identification is a challenge at buried interfaces, and even more powerful x-ray absorption techniques can be left with ambiguities in assignments.[47] Nonetheless, computational studies have suggested possible products for reaction between LLZO and the cathode material $LiMnO_2$, closely related to LMO ($LiMn_2O_4$).[50] Depending on the voltage, several binary metal oxides, lithiated manganese-deficient oxides, $La_xZr_yO_z$ compounds, and $LaMn_2O_5$ have been predicted as possible reaction products. The formation of a Mn-deficient Mn-oxide phase or a La-Mn mixed metal oxide would be most consistent with observation of Mn migration into the electrolyte region.

2.5 Conclusions

Thin film LMO electrodes were used to investigate the LMO-LLZO interface and its stability during electrochemical operation. The combination of ion-blocking

electrodes, symmetric cells, and full cells permitted isolation of individual cell interfaces and identification of key EIS signatures. Battery operation resulted in an apparent cycling-induced reaction between LMO and LLZO. EIS data from full and symmetric cell cycling indicated that this product increased the interfacial impedance of the cell, contributing to the capacity fade. XPS further showed that changes at the interface were associated with the formation of a reaction zone. We note that the amorphous nature of the films may make them more prone to reaction than crystalline LLZO, but that the present findings still place a conservative boundary on these materials' compatibility.

Irrespective of the growth of the interfacial product, the initial impedance of the LMO-LLZO interface was larger than desirable for a commerical battery. While extensive polishing was used to reduce Li_2CO_3 contaimation, it was still detected via XPS, and further reduction of interfacial contaminants may help to reduce this impedance. Aditional methods to passivate and reduce the impedance of the interface, such as addition of interlayers, could be investigated and subjected to the same analysis to assess interfacial degradation in future work. Along these lines, one recent study used an $Li_{2.3}C_{0.7}B_{0.3}O_3$ interlayer to lower interfacial impedance against LLZO, though capacity fade was later seen due to mechanical degradation.[107] Computational studies have also looked at the stability of a large range of possible interlayer materials, with $LiGaO_2$ and $LiNbO_3$[108] as well as Li_2ZrO_3[49] identified for high chemical capability as SSE interlayers. Experimental verification of the stability of

these possible interlayers is still neccesary. The methodology presented here serves as a useful template for further study of solid state electrochemical interfaces.

3 Decomposition of trace Li_2CO_3 during charging leads to cathode interface degradation with the solid electrolyte LLZO

3.1 Abstract

A major challenge for lithium-containing electrochemical systems is the formation of lithium carbonates. Solid-state electrolytes circumvent the use of organic liquids that can generate these species, but they are still susceptible to Li_2CO_3 formation from exposure to water vapor and carbon dioxide. It is reported here that trace quantities of Li_2CO_3, re-formed after following standard mitigation and handling procedures, can decompose at high charging potentials and degrade the electrolyte-cathode interface. *Operando* electrochemical mass spectrometry (EC-MS) is employed to monitor the outgassing of solid-state batteries containing the garnet electrolyte $Li_7La_3Zr_2O_{12}$ (LLZO), and, using appropriate controls, CO_2 and O_2 are identified to emanate from the electrolyte-cathode interface at charging potentials >3.8 V (vs. Li/Li^+). The gas evolution is correlated with a large increase in cathode interfacial resistance observed by potential-resolved impedance spectroscopy. This is the first evidence of electrochemical decomposition of *interfacial* Li_2CO_3 in garnet cells and suggests a need to report "time-to-assembly" for cell preparation methods. A graphical abstract is shown in **Figure 3.1.**

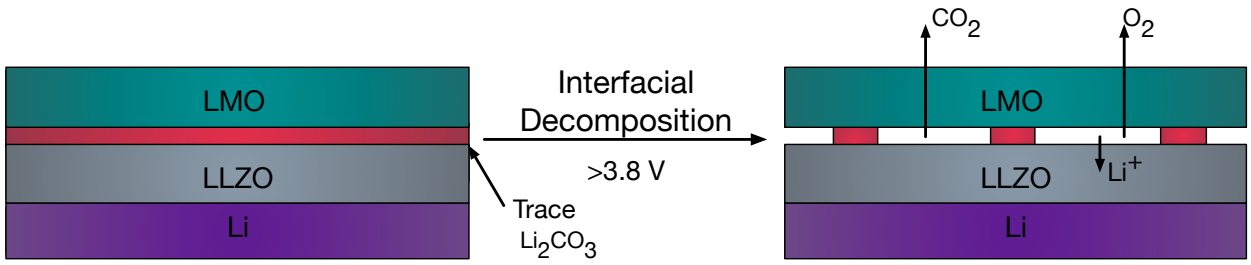

Figure 3.1. Graphical abstract illustrating the interfacial decomposition that occurs during charging potentials of >3.8 V for LMO | LLZO | Li cells.

3.2 Introduction

Solid state lithium-ion batteries offer several advantages over traditional lithium-ion batteries, most notably in enhanced safety and energy density, making them ideal for applications such as electric vehicles. However, these devices encounter stability issues with cycling, and viable commercial implementation will require a better understanding of their degradation mechanisms. The garnet $Li_7La_3Zr_2O_{12}$ (LLZO) is one of the most promising solid electrolytes owing to its high conductivity and stability versus Li metal. However, it is known to form an insulating Li_2CO_3 surface layer upon exposure to H_2O and CO_2, decreasing its efficacy. Formation of Li_2CO_3 is proposed to proceed in a two-step process, mediated by LiOH:[30]

(3.1) $Li_7La_3Zr_2O_{12} + xH_2O \rightarrow Li_{7-x}H_xLa_3Zr_2O_{12} + xLiOH$

(3.2) $LiOH + ½\ CO2 \rightarrow ½\ Li_2CO_3 + ½\ H_2O$

Further mechanistic details of the formation of these layers, along with methods of characterization and impacts on interfacial phenomena such as Li-dendrite growth on anodes, have been recently reviewed, with a focus on "best

practices" for eliminating Li_2CO_3.[109] To minimize contamination, the current state of the art synthesis procedure for "clean" LLZO involves polishing the electrolyte and annealing above 400˚C, completely within an inert argon atmosphere.[30] However, even going beyond this with rigorous ultra-high vacuum heat treatments, it has been found that these contaminants gradually reform at room temperature in an argon glovebox.[34]

Here we present direct evidence linking Li_2CO_3 to interfacial delamination between a model cathode and LLZO, assembled according to current standard practices. We implement *operando* electrochemical mass spectrometry (EC-MS) to show decomposition of sub-nanometer layers of Li_2CO_3 during charging cycles. These deposits (re)form on the surface of the LLZO between the time of its annealing and deposition of the cathode. The decomposition causes irreversible degradation of contact between the cathode and LLZO, and is a direct consequence of the oxidation of Li_2CO_3:[110]

$$(3.3)\ Li_2CO_3 \rightarrow 2Li^+ + 2e^- + \tfrac{1}{2}\ O_2 + CO_2\ (E^\circ = 3.82\ V\ vs.\ Li/Li^+)$$

We show these effects using thin-film LMO|LLZO|Li cells (LMO=$LiMn_2O_4$) and leverage potential-resolved electrochemical impedance spectroscopy (PR-EIS) as a complimentary method to highlight how these changes affect charge transport through the system. Gas evolution is further found to occur when applying a charging current to Au|LLZO|Li cells, where the gold acts as an ion-blocking electrode; this highlights that the decomposition reaction is interface-specific, rather than the result of carbonate formation on the surface of the cathode material.

To our knowledge, carbonate-induced delamination has not previously been observed or quantified for solid-state Li-ion batteries prepared by current best practices. We suggest this is because the primary focus of the field has been on engineering of the Li-metal anode interface[29,31,75,111–113] (and largely using symmetric cells), which operates near 0 V, whereas we observe the effect at an onset overpotential above 3.8 V. It is a problem specific to the cathode interface, and one that possibly explains the common observation of large first-cycle charging capacities seen for solid-state Li-ion batteries. Broadly, our investigations demonstrate an *operando* methodology for assessing the interfacial quality of assembled cells, and they suggest the necessity of highly controlled synthesis conditions to create effectively-contaminant-free garnet electrolyte cells. These findings have particular implications in limitations for fast charging and high-voltage cathodes, which we suggest will require investigation for correlations between gas evolution and performance shifts as a future standard practice.

3.3 Materials and Methods

3.3.1 Electrolyte Preparation

$Li_{6.4}La_3Zr_{1.4}Ta0.6O_{12}$ (LLZTO) was purchased from MTI Corporation (μ_d = 5 μm) and pelletized in a 13 mm stainless steel die (Across International) in 1g increments at 2 metric tons of pressure using a mechanical press (Carver Model M). The resulting pellets were placed in MgO boats within a tube furnace (Thermcraft® XST-3-0-36-1V2-F01) for a two-step sintering process[91], which has been shown to help densify pellets while limiting lithium loss through an initial high temperature

nucleation step and then lower temperature grain growth. Pellets were initially heated to 1200˚C at a ramp rate of 3˚C/min and held for 1 hour. The temperature was then reduced to 1100˚C and held for 5 hours before cooling to room temperature at a rate of 100˚C/hr. The approximate density of the pellets was 90%. Faces of the pellets were polished in air progressively with 150, 400, 800, and 1000 grit sandpapers (3M®, proprietary ceramic), followed by wet polishing with 1, 0.3, and 0.05 μm alumina particles (Electron Microscopy Sciences) to ensure a flat surface for electrode deposition as well as reduce Li_2CO_3 contamination.[36] The resulting pellet thickness are 0.9 mm, depending on how efficiently parallel faces can be achieved during initial polishing. Pellets were then immediately transferred into an argon filled glovebox and heated to 400°C for 3 hours to remove residual Li_2CO_3.

3.3.2 Cathode Deposition

For LMO electrodes, Pellets were next transferred under argon to an RF-sputtering deposition chamber (via a vacuum desiccator with pump, Desi-Vac™) built within an argon-filled glove box (Angstrom Engineering). LMO electrodes were deposited from a 2" LMO target (99.9% purity, ACI Alloys, Inc.). The sputter deposition was carried out at 60W, 15 cm target distance, 15 sccm of argon flow. A stainless-steel shadow mask with 10 mm diameter circles was used to control where the deposition occurred on the LLZO pellets. Depositions were 2 hours per electrode, with an estimated deposition rate of 0.9 nm/min to a total thickness of 110 nm. Aluminum current collectors were deposited within the same deposition chamber from an aluminum target to a thickness of ~120 nm, making the total thickness of

cathode and current collector ~230 nm. The cathode/electrolyte pellets were transferred under argon to the original glovebox for cell assembly. The estimated time between cooling of LLZO pellets and cathode deposition was 3-5 hours.

For Au electrodes, pellets were transferred under argon to a thermal evaporation chamber built within a nitrogen-filled glovebox (Angstrom Engineering). Gold pellets (Kurt J. Lesker Company) were evaporated using a two-step deposition process to a thickness of 80 nm. The gold films were transferred under nitrogen back to the original glovebox and annealed at 200˚C to improve adhesion of the evaporated films. The estimated time between cooling of LLZO pellets and cathode deposition was 3-4 hours.

3.3.3 Cell Assembly and Testing

(MBRAUN® Unilab Pro SP). To create the full cells, lithium foils. (0.75 mm thick) were punched (10 mm diameter), scraped to remove oxide, pressed onto the LLZO pellet, and placed into customized Swagelok® cells (**Fig. S1**). The side of the LLZO pellet opposite the LMO was gently polished with 2000 grit sandpaper inside the glovebox prior to cell assembly to re-clean the interface. The cells were then heated to 100˚C under 36 kPa pressure, the lithium foil separated and re-scraped to remove any newly-formed lithium oxide, and re-adhered to the LLZO. We have found that an oxide forms on the surface of the lithium if a high pressure is not immediately applied across these cells, due to trace oxygen diffusing to the interface, but scraping and pressing at 100˚C forms a protected interface.[37] This re-scraping procedure was found to decrease the Li-LLZO interfacial impedance substantially and thus improve

resolution of other impedance features. These pellet stacks were placed within PEEK cells, clamped in a vice to apply stack pressure, and rapidly connected to the MS for electrochemical testing at 100˚C. Calibration of cell headspaces for CO_2 was performed with standard calibration gases (GASCO®), the O_2 response was too near baseline to quantify.

All electrochemical measurements were performed on a Bio-logic SP-300 potentiostat/galvanostat/FRA. Before all reported cycling data, the cells were discharged to 2V at a rate of ~C/10 (1, to ensure cells started in fully discharged state. The theoretical capacity of all LMO cells is 10.2 μAh, based on the thickness of the electrodes and the complete extraction 2 full units of lithium (285 mAh/g). Some variation in cell capacities is expected due to slight removal of current collector in center of cells due to pressure cells experience. The areal loadings of the cathodic and anodic current collectors are 0.045 mg/cm^2. The resulting excess capacity of the lithium electrode relative to the LMO cathode is thus ~13000x.

3.3.4 Description of cell housing & EC-MS system

The design of our cell was largely based on that of McCloskey et al.,[114] but with changes made specifically for testing of all solid state batteries by enabling application of stack pressures. The combination of a low volume and hermetically sealed cell gives this system the low detection limit necessary for monitoring evolution of gaseous products at that arise in interfaces of solid states batteries.

The cell is comprised of two PEEK rods the seal against an outer PEEK sleeve with O-rings (**Figure 3.2A&B**).

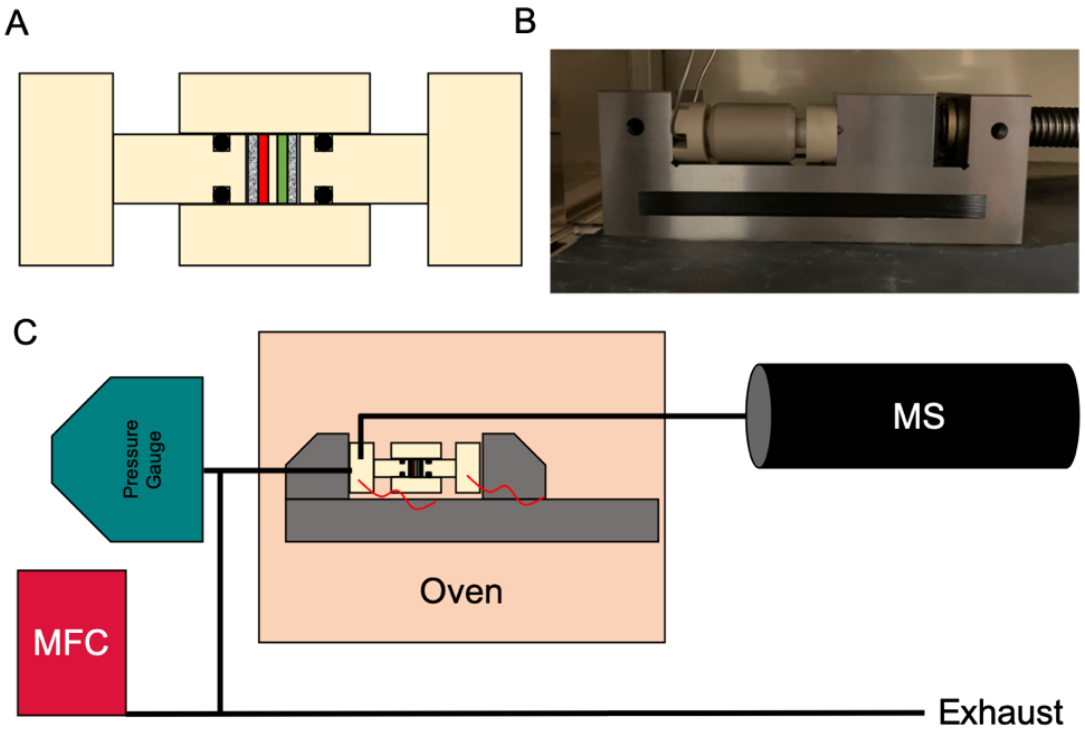

Figure 3.2. Cross-sectional diagram (A) and photograph (B) of custom-designed PEEK cell used in all experiments. C) Overview of entire EC-MS system including the PEEK cell.

PEEK was chosen for its electrical insulation, machinability, chemical compatibility, and thermal stability. Electrical connections and capillaries are fed through and sealed with compression O-rings. The overall metal pieces connecting the cell were kept to a minimum to minimize capacitance to provide an accurate EIS responses. In order to apply a stack pressure to the cell while also minimizing the headspace for sensitivity we had to construct the cell without the use springs. Therefore, we opted to construct the cell to be operated within a mechanical vice that was small enough to fit within an oven to be able to test the cell at a variety of temperatures. To isolate the cell electrically from the vice, as well as allow

compression, we added to head caps to the pistons. The slots in the side of these caps allow electrical connection to be made and capillaries to be able to pass through while the flat head could accept the mechanical load from the vice. A sintered stainless-steel frit with a pore size of 2 micron was used a spacer to create the cell headspace, although we do note that there is some additional headspace as the LLZO pellet is 2 mm smaller than the diameter of the outer PEEK sleeve. In summary we designed an extremely low volume headspace cell (estimated volume ~0.3 mL) with accurate EIS response specifically for use with solid state lithium batteries in that it can be used with a range of temperature and stack pressures.

The cell and vice are contained within an oven to allow control over cell operating temperature (**Figure 3.2C**). A mass flow controller is connected to the system to control the flow of carrier into the cell headspace. This carrier gas is teed off to reduce flowrate into the cell using a 50 micron peek capillary, a necessary reduction for the small amounts of gas evolved in these experiments. The effluent of the cell is directly connected to the MS with stainless steel capillary tubing to sample all evolved gases during cell operation.

Differential electrochemical mass spectrometry (DEMS) has been used to measure quantities in a similar way to our EC-MS system. The lack of a differential pumping stage and the direct flow of the entire cell headspace into the MS differentiates our setup from other DEMS or localized probe online electrochemical mass spectrometry (OLEMS) systems, hence the use of the general nomenclature "EC-MS".

3.4 Results and Discussion

To characterize the cathode interface degradation of LLZO-based solid state cells, a thin film architecture, LMO | LLZO | Li, with sputter-deposited LMO cathodes was employed (**Figure 3.3**).

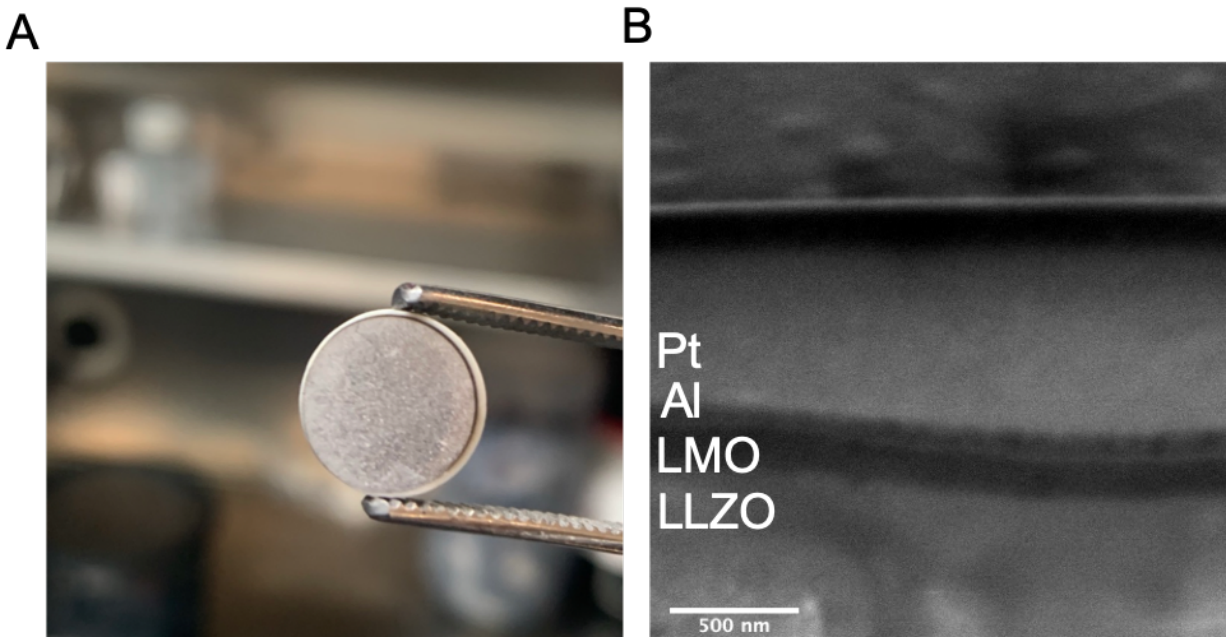

Figure 3.3. A) Photograph of LLZO pellet with cathode and current collector deposited. B) Cross sectional SEM image of cathode interface prepared by focused ion beam. The platinum is deposited to protect the interface during ion-milling.

Notably, all electrolytes were polished and annealed at 400°C, and they were kept under argon at all times leading up to cathode deposition. The "time-to-assembly" (post-annealing) was roughly 3-5 hours for all cells. During initial cycling, large first-cycle charging capacities were observed, followed by much smaller subsequent discharge capacities, as shown in **Figure 3.4**.

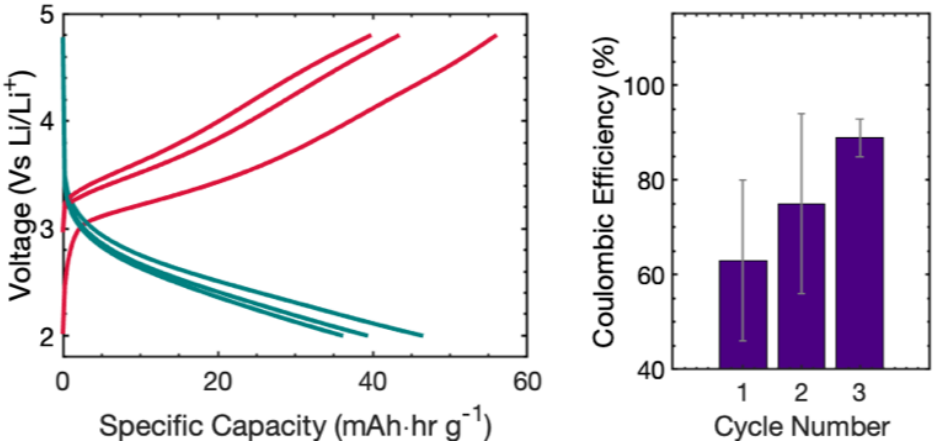

Figure 3.4 (A) Representative charge (red) and discharge (teal) behavior over 3 cycles for LMO | LLZO | Li cells. (B) Average coulombic efficiencies based on three replicate cells over 3 cycles for LMO | LLZO | Li architecture. Cells were cycled at 38uA/cm2 (~3C).

Alongside the initial losses in capacity, the coulombic efficiencies of these cells showed a marked increase and gradual stabilization (at the diminished capacity) as cycling continued. Reports of high-charging capacities and subsequent capacity fade for the first cycles of bulk-type LLZO full cells have previously been ascribed to organolithium compounds formed during sintering.[107,115,116] However, these compounds have never been identified, and while they are likely present in the cited systems (likely alongside Li_2CO_3) they would not be present in the cells constructed in this study because the cathodes here were not derived from organic precursors.

To explore the nature of the initial degradation effects, impedance response was next monitored throughout early charging and discharging cycles to probe the potential-dependence of characteristic microscopic processes. A full cycle corresponds roughly to variation of the lithium stoichiometry in the range $0<x<2$ for $Li_{2-x}Mn_2O_4$. To identify onset regimes of various phenomena, the charging cutoff voltage was

increased between sequential cycles while taking the PR-EIS measurements. **Figures 3.5A** and **3.5B** show EIS taken at intervals of 400 mV between initial charge and discharge cutoffs of 4 V and 2 V vs. Li/Li^+, respectively. We have previously resolved these spectra into a number of bulk and interfacial contributions through comparison with symmetric cells (Li-Li, LMO-LMO, and blocking Au-Au), and found that a mid-frequency semicircle preceding the low-frequency diffusion tail corresponds to the parallel processes of charge transfer and space charge formation at the LMO|LLZO interface.[70] An equivalent circuit diagram and detailed fits will be discussed below, but we first comment on a few holistic aspects. Most importantly, when kept below 4 V, the primary features of the EIS response appear to maintain their relative magnitude and shape at individual voltages in either cycling direction, with the exception of a slight growth in resistance associated with the diffusion regime (crystal domain growth within the thin film).[117] In contrast, when the cutoff voltage is increased, the mid-frequency impedance arc associated with interfacial charge transfer at the cathode grows to a dramatically larger resistance that persists throughout the remainder of the EIS measurements over discharge and further cycling. **Figures 3.5C** and **3.5D** show a survey of PR-EIS spectra between a high charge cutoff of 4.6 V and discharge back to 2 V, with finer spacings of 100 mV shown in the inset of **Figure 3.5C**. Clear changes in the EIS signatures manifest around 4.3-4.4 V. While this is a relatively high voltage of apparent onset, it may be noted that CO_2 evolution (to be shown below) is observed much sooner (3.8 V) and simply accelerates at higher voltage. This suggests that the same degradation mechanism

may be subtly operative in many cells within the literature that use a cutoff voltage of 4.0 V, despite it not resulting in obvious, large, single-cycle impedance increases.

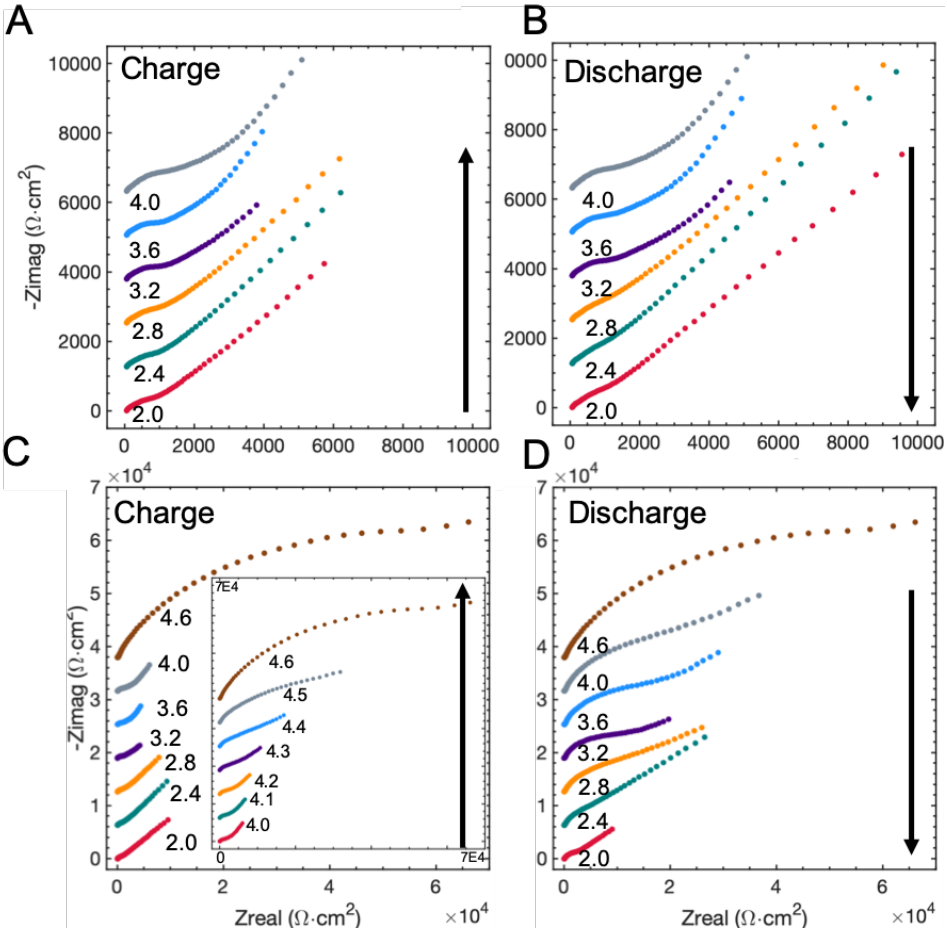

Figure 3.5. Impedance spectra for charge and subsequent discharge at 4μA/cm2 with 4.0 V cutoff (A-B) and 4.5 V cutoff (C-D), showing irreversible degradation at the higher potential. Inset in panel C shows every 100 mV between 4 and 4.6. Frequencies range from 1 MHz to 0.5 Hz (from left to right across each spectrum.) The rate of cycling between EIS measurements was ~C/3 (3 μA).

The physicochemical changes induced by decomposition of Li_2CO_3 can be further compared in equivalent circuit (**Figure 3.6C**) fits for the EIS before and after high charging voltages were applied to the cell (**Figures 3.6A** and **3.6B**).

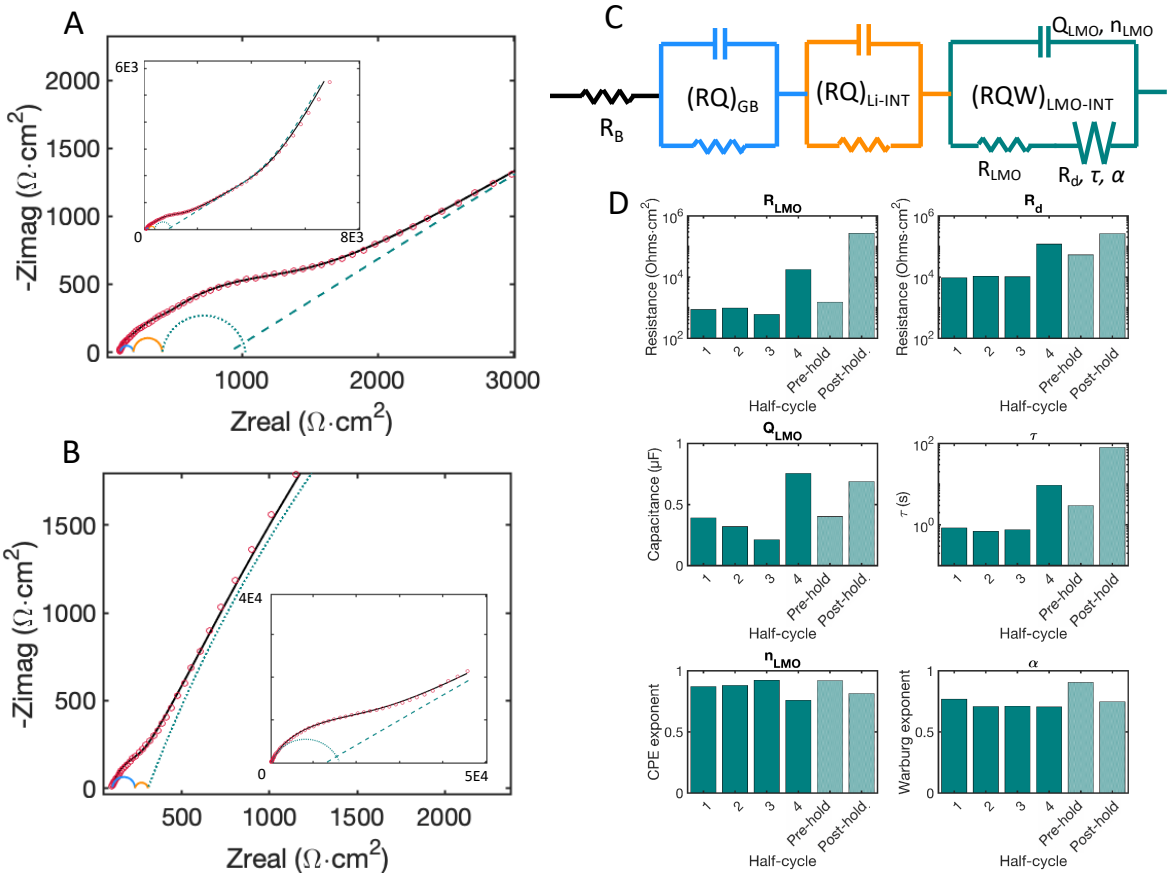

Figure 3.6 EIS analysis of LMO | LLZO | Li cells. (A) EIS spectra and fit component impedances measured at 3.6 V, before high voltage was applied. (B) EIS spectra and fit component impedances measured at 3.6 V, after high voltage was applied. A large growth in the final semicircle feature is evident. (C) Equivalent circuit used to fit LMO | LLZO | Li cells, with elements involving critical parameters marked (D) Evolution of the labeled equivalent circuit parameters corresponding to the teal section of the circuit (equations in Supporting Information) measured at 3.6 V over four half-cycles 2.0-4.6 V (labeled 1-4), as well as before and after more extreme cycling (with a fresh cell, light hatched bars) including a 10 minute potentiostatic hold at 4.8 V.

The fits after high voltage charging (4th half-cycle) show a large increase to the interfacial resistance of the cathodic interface arc (R_{LMO}) as may be expected, as well as a noticeable decrease in the associated constant phase element (CPE) exponent (n_{LMO}) (**Figure 3D,** full fitting data in **Table 3.1**).

Table 3.1 Equivalent circuit fitting parameters for LMO cells at different potentials.

2.4 V													
Half-cycle	R_b	R_{GB}	Q_{GB}	n_{GB}	R_{Li}	Q_{Li}	n_{Li}	R_{LMO}	Q_{LMO}	n_{LMO}	Zw	τ	α
1	1.06E+02	1.08E+02	2.00E-08	1.00E+00	2.31E+02	7.79E-08	9.83E-01	9.86E+02	5.71E-07	8.50E-01	2.69E+04	2.12E+00	9.41E-01
2	1.10E+02	1.09E+02	2.01E-08	1.00E+00	2.65E+02	9.23E-08	9.57E-01	1.18E+03	3.61E-07	8.83E-01	6.23E+04	2.09E+00	9.83E-01
3	1.10E+02	1.08E+02	1.76E-08	1.00E+00	2.52E+02	5.43E-08	9.96E-01	9.88E+02	2.79E-07	9.11E-01	6.98E+04	5.88E+00	9.52E-01
4	1.07E+02	1.51E+02	2.95E-08	9.86E-01	2.67E+02	1.25E-06	9.15E-01	7.31E+03	7.19E-07	7.68E-01	1.66E+05	9.67E+00	7.72E-01
2.8 V													
Half-cycle	R_b	R_{GB}	Q_{GB}	n_{GB}	R_{Li}	Q_{Li}	n_{Li}	R_{LMO}	Q_{LMO}	n_{LMO}	Zw	τ	α
1	1.07E+02	1.13E+02	2.02E-08	1.00E+00	2.46E+02	1.01E-07	9.61E-01	9.74E+02	4.79E-07	8.63E-01	1.86E+04	1.10E+00	8.84E-01
2	1.10E+02	1.17E+02	1.87E-08	1.00E+00	2.70E+02	5.32E-08	1.00E+00	8.15E+02	1.52E-07	9.73E-01	8.40E+04	9.93E+00	8.92E-01
3	1.09E+02	1.06E+02	1.93E-08	1.00E+00	2.73E+02	9.43E-08	9.51E-01	1.05E+03	3.73E-07	8.86E-01	2.44E+04	1.03E+00	9.10E-01
4	1.04E+02	1.54E+02	2.84E-08	9.91E-01	2.77E+02	1.47E-06	9.23E-01	1.12E+04	7.78E-07	7.62E-01	1.09E+05	9.13E+00	6.63E-01
3.2 V													
Half-cycle	R_b	R_{GB}	Q_{GB}	n_{GB}	R_{Li}	Q_{Li}	n_{Li}	R_{LMO}	Q_{LMO}	n_{LMO}	Zw	τ	α
1	1.07E+02	8.82E+01	2.20E-08	1.00E+00	2.42E+02	8.48E-08	9.55E-01	8.82E+02	4.13E-07	8.69E-01	1.08E+04	1.93E+00	7.24E-01
2	1.08E+02	1.04E+02	2.10E-08	1.00E+00	2.33E+02	9.94E-08	9.57E-01	8.95E+02	3.13E-07	8.86E-01	1.30E+04	1.80E+00	6.89E-01
3	1.08E+02	1.00E+02	1.81E-08	1.00E+00	2.45E+02	4.70E-08	1.00E+00	6.30E+02	1.67E-07	9.56E-01	1.31E+04	2.27E+00	6.89E-01
4	1.02E+02	1.32E+02	3.05E-08	9.98E-01	9.45E+02	6.13E-07	9.79E-01	1.80E+04	1.34E-06	7.11E-01	1.03E+05	2.20E+01	8.50E-01
3.6 V													
Half-cycle	R_b	R_{GB}	Q_{GB}	n_{GB}	R_{Li}	Q_{Li}	n_{Li}	R_{LMO}	Q_{LMO}	n_{LMO}	Zw	τ	α
1	1.09E+02	1.14E+02	2.03E-08	1.00E+00	2.26E+02	8.56E-08	9.78E-01	8.72E+02	3.91E-07	8.73E-01	9.40E+03	8.42E-01	7.68E-01
2	1.07E+02	1.05E+02	2.12E-08	1.00E+00	2.33E+02	9.88E-08	9.61E-01	9.66E+02	3.19E-07	8.81E-01	1.06E+04	6.93E-01	7.08E-01
3	1.08E+02	9.32E+01	2.06E-08	1.00E+00	2.25E+02	6.60E-08	9.76E-01	6.03E+02	2.13E-07	9.24E-01	1.02E+04	7.61E-01	7.12E-01
4	1.06E+02	1.44E+02	2.81E-08	9.95E-01	2.54E+02	1.95E-06	9.52E-01	1.78E+04	7.55E-07	7.59E-01	1.19E+05	9.41E+00	7.06E-01
4 V													
Half-cycle	R_b	R_{GB}	Q_{GB}	n_{GB}	R_{Li}	Q_{Li}	n_{Li}	R_{LMO}	Q_{LMO}	n_{LMO}	Zw	τ	α
1	1.09E+02	9.70E+01	2.01E-08	1.00E+00	2.19E+02	5.29E-08	9.99E-01	5.67E+02	1.34E-07	9.54E-01	9.72E+03	3.98E-01	6.05E-01
2	1.09E+02	9.70E+01	2.01E-08	1.00E+00	2.19E+02	5.29E-08	9.99E-01	5.67E+02	1.34E-07	9.54E-01	9.72E+03	3.98E-01	6.05E-01
3	1.08E+02	1.10E+02	1.99E-08	1.00E+00	2.33E+02	8.37E-08	9.74E-01	8.26E+02	2.38E-07	9.08E-01	1.22E+04	5.85E-01	6.84E-01
4	1.08E+02	2.04E+02	2.56E-08	9.98E-01	3.46E+02	2.73E-07	9.85E-01	1.09E+04	2.92E-07	8.79E-01	1.48E+05	5.33E+00	6.61E-01

CPEs are used to model the non-ideality of real electrochemical capacitances, and a decrease in the exponent can be indicative of increasing surface roughness,[100] such as would be the case for a previously sharp LMO | (Li_2CO_3) | LLZO interface that was experiencing delamination. In addition to the changes in the parameters characterizing the cathode interface itself, it may be noted that the time constant associated with diffusion within the LMO also rises. The time constant relates to both

the diffusion coefficient and the characteristic path length $\left(\tau_d = \frac{\delta^2}{D_x^{\alpha}}\right)$, and the initial diffusion coefficient (with δ being electrode thickness) was 1.01x10^{-10} cm^2/s, in relative agreement with literature.[118,119] After applying high voltage, we attribute the rise in τ_d to increases in the average diffusion path length for Li entering the film at fewer points, due to delamination. This interpretation is consistent with the changes seen in the Warburg element resistance (R_d), which we previously mentioned relates more directly to grain growth; the key distinction to stress in comparison to τ_d is that the changes to R_d are more asymptotic with respect to cell break-in. **Figure 3.6D** highlights this through comparison of separate tests on an identical cell subjected to more extreme cycling to a 4.8 V cutoff and a potentiostatic hold at 4.8 V (the procedure utilized below for gas quantification; EIS in **Fig. 3.7)**

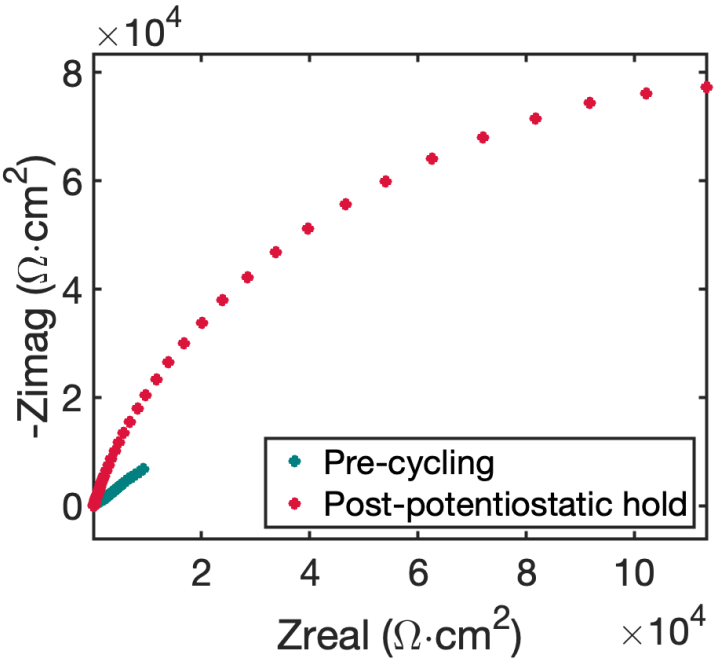

Figure 3.7. Cell impedance changes pre-cycling (green), and after the cycling procedure utilized for CO_2 quantification (red).

Fitting values associated with **Figure 3.7** are presented in **Table 3.2.**

Table 3.2 Equivalent circuit fitting parameters for LMO | LLZO | Li cell before and after EC-MS gas quantification procedure

	Rb	R_{GB}	Q_{GB}	n_{GB}	R_{Li}	Q_{Li}	n_{Li}	R_{LMO}	Q_{LMO}	n_{LMO}	Zw	τ	α
Pre-cycling	1.23E+02	5.51E+01	2.35E-08	1.00E+00	1.16E+02	3.45E-07	9.58E-01	1.52E+03	4.01E-07	9.21E-01	5.32E+04	2.99E+00	9.05E-01
Post-potentiostatic hold at 4.8V	1.14E+02	4.73E+01	3.19E-08	1.00E+00	3.43E+02	6.61E-06	9.79E-01	2.71E+05	6.87E-07	8.14E-01	2.64E+05	7.92E+01	7.47E-01

After the higher voltage hold, the area-specific resistance for the Warburg element (R_d) still plateaus on the order of 10^5 Ω-cm^2, whereas the R_{LMO} and τ_d values, attributed to Li_2CO_3 decomposition, show much more growth relative to their initial values, beyond what occurred in the 4.6 V cycled cells.

The observed irreversible growth in interfacial impedance could in principle be consistent with either physical delamination (instigated by Li_2CO_3 decomposition) or chemical reaction (between cathode and electrolyte). This was probed by using Au cathodes in place of LMO. Because Au is a blocking electrode, appreciable charging of the cell should not be possible in the absence of any surface contaminants. However, a small irreversible charging current was able to be passed, thereby suggesting the presence of an unstable impurity phase at the Au-LLZO interface. The EIS of the Au | LLZO | Li cells before and after this irreversible charge (**Figure 3.8 A-C**) also shows over an order of magnitude increase in the resistance associated with the Au-LLZO interface (**Figure 3.8D**).

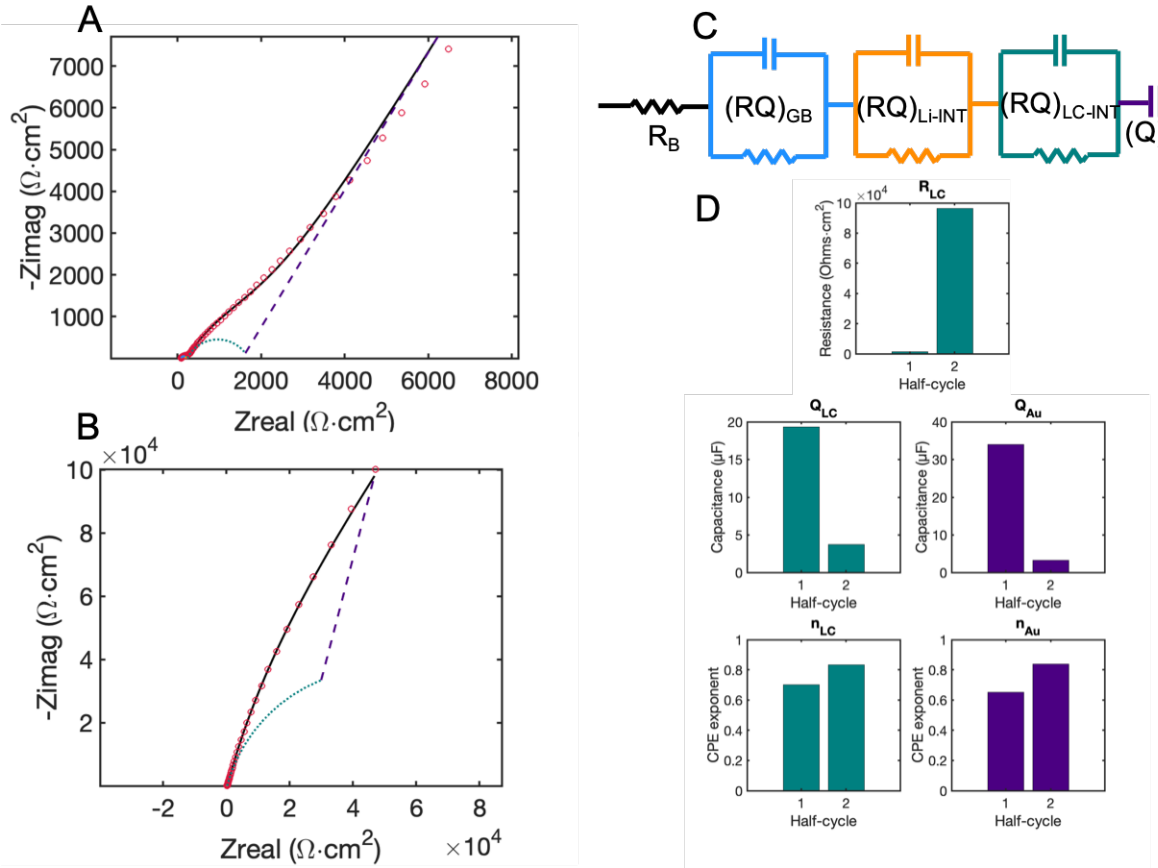

Figure 3.8 EIS analysis of Au|LLZO|Li cells. (A) EIS spectra and fit component impedances before high voltage (4.8 V) was applied (B) EIS spectra and fit component impedances after high voltage was applied. A large growth in the final semicircle feature is evident. (C) Equivalent circuit used to fit Au|LLZO|LMO cells, (D) Evolution of specific equivalent circuit parameters corresponding to the teal and purple sections of the circuit) measured before and after application of a charging current. In contrast to LMO-cells, the teal section corresponds to ionic conduction and capacitance of the lithium carbonate layer itself (now resolvable from the cathode) and the purple section represents the blocking nature of the Au contact.

This corroborates the suggestion of a mechanism for delamination via the electrochemical oxidation of Li_2CO_3, re-formed before the cathode is deposited. The associated equivalent circuit fitting values for the Au cell are presented in **Table 3.3**.

Table 3.3 Equivalent circuit fitting parameters for Au | LLZO | Li cell before and after application of 4.8 V.

	R_b	R_{GB}	C_{GB}	n_{GB}	R_{Li}	C_{Li}	n_{Li}	R_{LC}	Q_{LC}	n_{LC}	Q_{Au}	n_{Au}
Pre-HV	9.08E+01	9.18E+01	2.66E-08	1.00E+00	4.60E+01	4.45E-07	9.91E-01	1.45E+03	1.93E-05	7.02E-01	3.40E-05	6.51E-01
Post-HV	9.09E+01	9.55E+01	2.70E-08	1.00E+00	6.51E+01	3.37E-07	9.96E-01	9.65E+04	3.73E-06	8.33E-01	3.20E-06	8.37E-01

Differential electrochemical mass spectrometry (DEMS) has previously been implemented to quantitatively assess the stoichiometry and Faradaic (in)efficiency toward Li_2CO_3 in traditional (liquid-electrolyte) Li-ion batteries,[120–122] as well as other systems requiring detailed accounting of charge passed, such as Li-O_2 batteries.[123,124] However, in solid-state cells with proper pretreatments according to current best practices, the amount of Li_2CO_3 available to be oxidized at the LMO-LLZO interface is very low, and its ability (or timescale) to escape the buried solid-solid interface is also unknown. Special care was thus taken in designing a cell and EC-MS system with adequate sensitivity to detect low amounts of gas that would be associated with electrochemical decomposition of re-formed Li_2CO_3. As a point of reference, a 1 nm thick film would correspond to approximately 2 nanomols of crystalline Li_2CO_3 per cm^2 of LLZO pellet.

Using the low-volume cell and EC-MS apparatus described in section 3.3.4, cells were first discharged to 2V, before initiating a cycling procedure from 2.0-4.8 V (**Figure 3.9**).

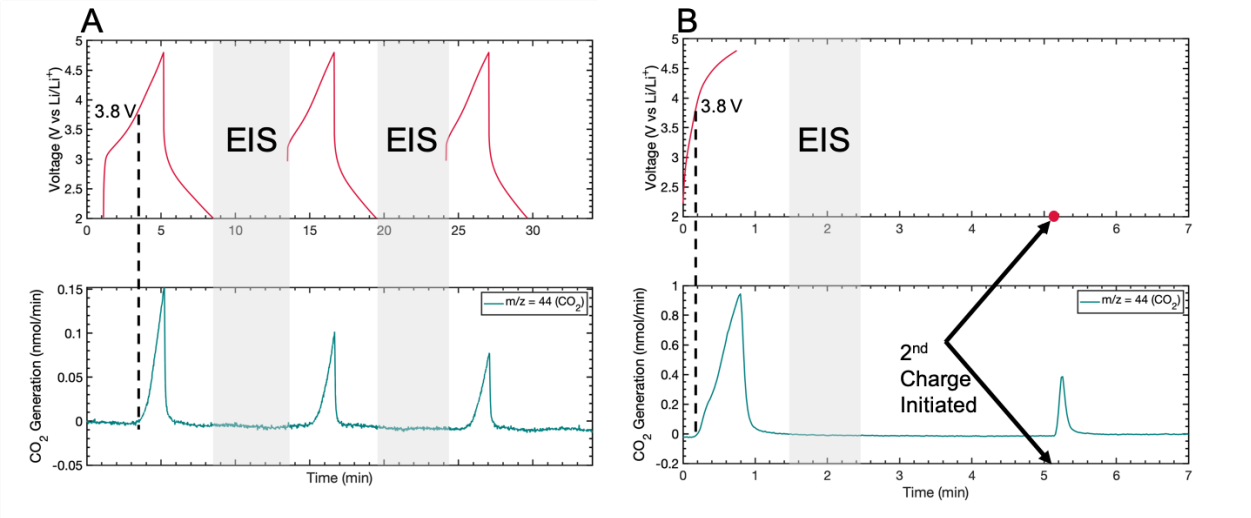

Figure 3.9. Evolution of CO_2 as detected by EC-MS as correlated to charging voltage for 3 cycles of LMO | LLZO | Li cell (A) and 2 cycles for the Au | LLZO | Li cell (B). The onset potentials of gas evolution is highlighted for the first cycle. LMO and Au cells are cycled at 30uA (~3C for the LMO cells).

As the cell charged, CO_2 (**Figure 3.9**) and O_2 (**Figure 3.10**) evolution were detected at ~3.8 V and above.

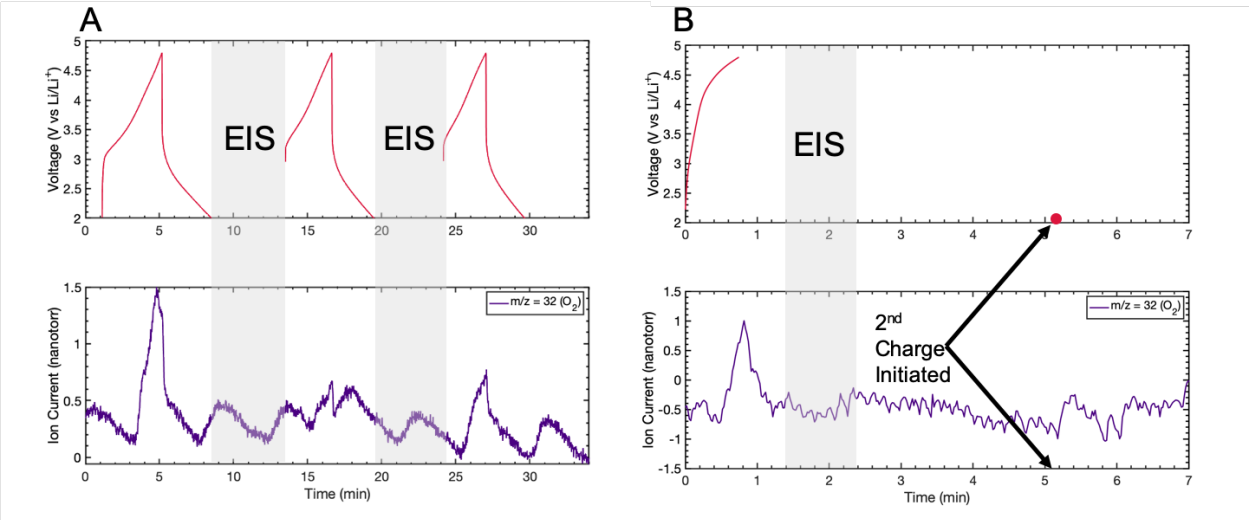

Figure 3.10. Evolution of O_2 as detected by EC-MS as correlated to charging voltage for 3 cycles of LMO | LLZO | Li cell (A) and 2 cycles for the Au | LLZO | Li cell (B). LMO and Au cells are cycled at 30uA (~3C for the LMO cells).

No gas evolution was detected during discharge; however, evolution of both O_2 and CO_2 resumed on the following two charging cycles, with diminishing response each time, consistent with degradation of a finite source of Li_2CO_3.[125] The total amount of CO_2 evolved based on these first 3 cycles followed by a 10 min potentiostatic hold at 4.8 V (full profile in **Figure 3.11**) totaled 0.51 nanomols, which would correspond to an approximately 0.2 nm film.

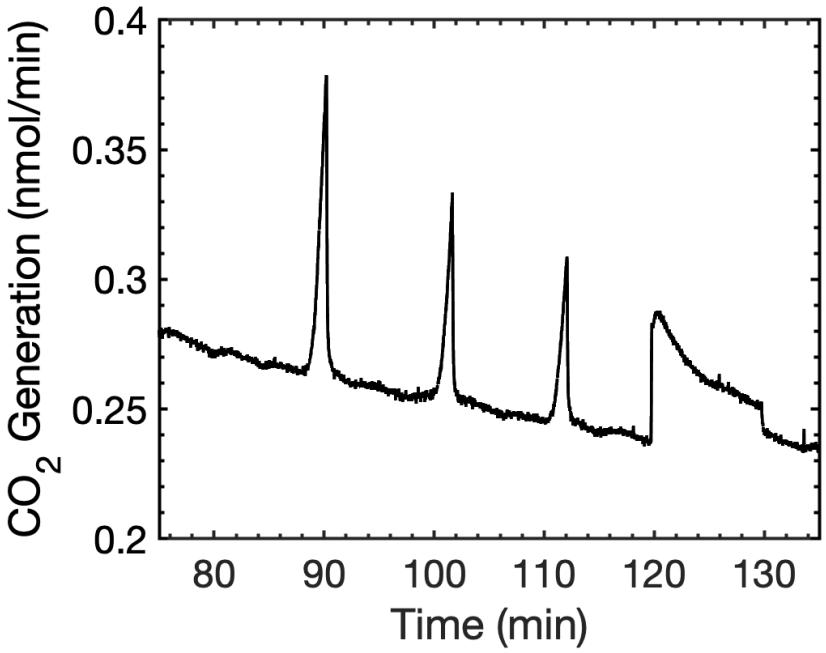

Figure 3.11. CO_2 generation for three cycles followed by a 10 min potentiostatic hold at 4.8 V.

Currently, there are only two examples of MS being employed to monitor all-solid-state cells during operation, and these works involved measuring the evolution of CO_2 from *bulk* cathodes.[126,127] Thus, the current work represents identification of a new "chemically relevant" lower limit for Li_2CO_3 contamination, specific to the interfacial characteristics of solid-state systems.

Further verification of the Li_2CO_3 decomposition was demonstrated by applying oxidative currents to Au|LLZO|Li cells while monitoring gas evolution by EC-MS. Both CO_2 (**Figure 3.9B**) and O_2 (**Figure 3.10B**) were observed, and the cell was found to be effectively dead after the first cycle—initiating the same oxidation procedure a second time immediately hit the cutoff voltage of the experiment. The total evolution from the Au cell amounted to 0.38 nanomols of CO_2, similar to the LMO cell, but in contrast, the first cycle gave a much higher rate of CO_2 evolution. We hypothesize that gas trapping within interfacial pockets could provide an underestimate of the CO_2 produced, and this may be more prevalent in the LMO cells due to better adhesion between regions in direct contact with LLZO, as well as the electrode thickness (LMO+Al ~230 nm vs. Au ~80 nm). We also note that when studying contamination, exact quantities will inherently be subject to variation; the magnitudes of film growth quoted here are reproducible within our procedure, and are meant to be representative of typical preparations considered to be standard best practices in most labs. Using a sputter chamber equipped with a substrate heater capable of annealing the LLZO pellets under UHV conditions directly prior to deposition could likely synthesize a truly Li_2CO_3-free surface; however, the key takeaway is that for typical assembly conditions that require exposure to a glovebox environment, vanishingly small quantities of Li_2CO_3 still have a substantive impact.

3.5 Conclusions

Through cycling and PR-EIS measurements of electrochemical cells with LLZO electrolytes, we observed a large resistive feature that corresponds with changes to

the LLZO-cathode interface. This change becomes prominent in the 4-4.5 V cell potential range. Through the use of *operando* EC-MS, we found evidence for the electrochemical decomposition of Li_2CO_3 coinciding with these changes, with gas evolution onsetting at even lower potentials than where major short-term performance losses are observed. By using comparable cells with intercalating and blocking electrodes, we were able to confirm that gas evolution was specifically from the cathode interface. The changes observed here are generally not observed in Li symmetric cells, where the voltages are lower, and thus we underscore the importance of full cell testing when designing synthesis methods for garnet solid electrolyte-based batteries. Lithium carbonate decomposition will be a particular concern for high voltage and fast-charge cathode materials, which may experience more rapid and catastrophic failure by this mechanism. We have further demonstrated that while removal of electrolyte-based lithium carbonate is extremely important, post-removal cell assembly must also be viewed as time-sensitive even in argon glovebox conditions, demanding additional strategies to prevent surface contaminant re-formation.

While the thin film cells studied here are most effective in isolating the impact of interfaces, further research will be needed to determine how the findings of this study translate to bulk-cathode cells. We suspect that the negative effects of delamination might be reduced if a more integrated, three-dimensional interface is formed (e.g. graded cathodes), but because the decomposition reaction stems from the electrolyte it will still pose an issue unless formation of Li_2CO_3 can be completely

mitigated. Extremely rapid cell assembly and/or assembly of solid-state cells under inert atmospheres at temperatures >400˚C could be one pathway to forming a Li_2CO_3-free interface, but this would be contingent upon avoiding interfacial reactions possibly taking place between electrolyte and electrode at these elevated temperatures. Sequential sputtering has been recently employed to this effect to create LCO|LLZO half cells,[128] though the approach would not readily be adapted beyond thin film batteries. Furthermore, it is possible that protective interlayers,[49,107] if fabricated quickly, could help mitigate this issue by shielding LLZO from contaminants.[129] No matter which direction these Li_2CO_3 mitigation routes take, increased attention to detail and documentation of synthesis conditions including time-to-assembly and gaseous environment conditions at all stages for each electrode—ideally followed by in-situ analyses of off-gassed products—will be necessary to accurately probe the degradation mechanisms of LLZO-containing cells.

4 Thermally Enhancing the Conductivity of Discharge Products to Promote Deep Discharge of Solid State Li-O_2 Batteries

4.1 Introduction

Li-O_2 batteries have been widely investigated due to their theoretical energy density being among the highest possible for different battery chemistries. However, parasitic reactions, poor cycling stability, and the insulating nature of their discharge products have all proven to be large hurdles for these cells, and overcoming these challenges is necessary for their commercialization. Two primary pathways have been identified for the formation of the discharge product Li_2O_2 in aprotic electrolyte Li-O_2 cells: (1) a surface mechanism and (2) a solution mechanism.[63] The first mechanism results in sustained growth of a film on the cathode surface until a limiting thickness occurs, resulting in a phenomenon coined "sudden death" where the cells experience a dramatic increase in overpotential due to the insulating nature of Li_2O_2,[130] ultimately severely limiting their realized capacity. The discovery of the solution mechanism circumvented the limited growth of the surface mechanism by moving the path of the electrons out of the insulating Li_2O_2 products, instead relying on the dissolution of surface intermediate LiO_2, which could then disproportionate into large particulate Li_2O_2 on the cathode surface. While this mechanism can therefore result in a marked increase in cell capacity due to thicker discharge products, detachment of these particles from the electrode[65] and parasitic reactions

due to aprotic electrolytes are still issues in these cells, ultimately limiting their cycle life. We suggest that by employing a solid electrolyte instead of an aprotic electrolyte, the issues present at the cathode will be further mitigated. Solid electrolytes offer two massive benefits when compared to aprotic electrolytes, their wider operable temperature range permitting elevated operating temperature, which promotes depth of discharge through thermal-enhancement of ionic and electronic conductivities of the discharge product, and the absence of organic carbon-containing compounds that can lead to parasitic reactions for aprotic electrolytes. Ceramic solid electrolytes have been investigated previously for Li-O_2 cells, however these studies are in far fewer number than their liquid electrolyte counterparts, most likely due to difficulty in challenges with structuring of the cathode-electrolyte interface.

Elevated operating range has been previously employed in LiO_2 batteries through the use of molten salt electrolytes, where it was found that depending on the operating temperature and choice of cathode, the nature of the discharge product could shift from Li_2O_2 (<150˚C or carbon cathode)[53,65] to Li_2O (>150˚C, Ni-hybrid cathode).[53,54] These cells largely mitigated parasitic products by using inorganic electrolytes, and were found to operate through the solution mechanism, further increasing their depth of discharge but making them vulnerable to capacity fade via discharge product solubility and detachment. There are two examples of solid state cells operated at high temperatures, but both utilized carbon containing cathodes as well as ambient atmosphere operation making them ill-suited for directly probing high temperature solid state Li-O_2 chemistry.[69,131] Additionally, because discharge

products in solid state Li-O_2 batteries grow into the gaseous cell headspace rather than a liquid electrolyte, losses due to solubility and particle detachment are not expected. Growth of discharge product is interpreted through a surface, film mechanism, where after initial nucleation at the LLZO-Au-O_2 triple-phase-boundary (TPB), sustained growth of the discharge continues via conduction of electrons through the discharge product until a conductivity-limited thickness is achieved.

Here, we propose an alternative cell architecture enabled by the use of a ceramic solid electrolyte, where a patterned metallic cathode is used atop of a solid electrode to permit lateral electron transport across the full cathode area for current collection (**Figure 4.1**), inspired by the design employed by Suzuki et al.[67,68]

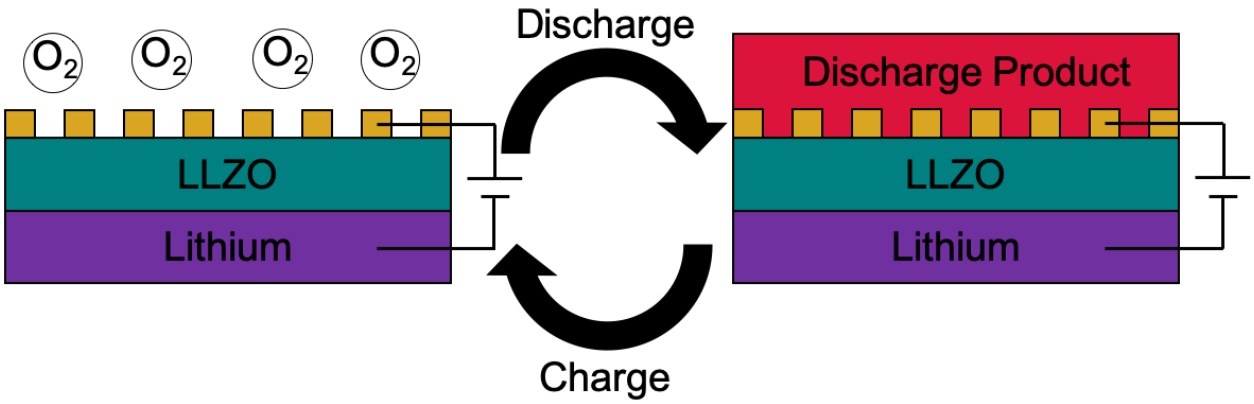

Figure 4.1. Cross-sectional depiction of cell architecture utilized, where the gold electrode is patterned bars across the surface of LLZO pellet. Also depicted is the cycling behavior and corresponding presence or lack of discharge products.

However, by moving to significantly higher temperatures our design promotes depth of discharge through thermal-enhancement of the ionic and electronic conductivities of the discharge product. Additionally, the absence of organic materials helps to

mitigate capacity-loss inducing parasitic reactions. Presence of discharge products is first confirmed by scanning election microscopy (SEM), and Raman spectroscopy. Galvanostatic measurements demonstrate an initial break-in period followed by stable cycling, and the voltage profiles are interpreted. EC-MS is utilized in combination with electrochemical impedance spectroscopy (EIS) to further analyze discharge products.

4.2 Materials and Methods

4.2.1 Electrolyte Preparation

$Li_{6.4}La_3Zr_{1.4}Ta0.6O_{12}$ (LLZTO) was purchased from MTI Corporation (μ_d = 5 μm) and pelletized in a 13 mm stainless steel die (Across International) at 2 metric tons of pressure using a mechanical press (Carver Model M). The resulting pellets were placed in MgO boats within a tube furnace (Thermcraft® XST-3-0-36-1V2-F01) for a two-step sintering process[91], which has been shown to help densify pellets while limiting lithium loss through an initial high temperature nucleation step and then lower temperature grain growth. Pellets were initially heated to 1200˚C at a ramp rate of 3˚C/min and held for 1 hour. The temperature was then reduced to 1100˚C and held for 5 hours before cooling to room temperature at a rate of 100˚C/hr. The approximate density of the pellets was 90%. Faces of the pellets were polished in air progressively with 150, 400, 800, and 1000 grit sandpapers (3M®, proprietary ceramic), followed by wet polishing with 1, 0.3, and 0.05 μm alumina particles (Electron Microscopy Sciences) to ensure a flat surface for electrode deposition as well

as reduce Li_2CO_3 contamination.[36] Pellets were then immediately transferred into an argon filled glovebox and heated to 400°C for 3 hours to remove residual Li_2CO_3.

4.2.2 Cathode Deposition

Pellets were affixed to shadow masks with a 6mmx6mm square electrode area (**Figure 4.2A**).

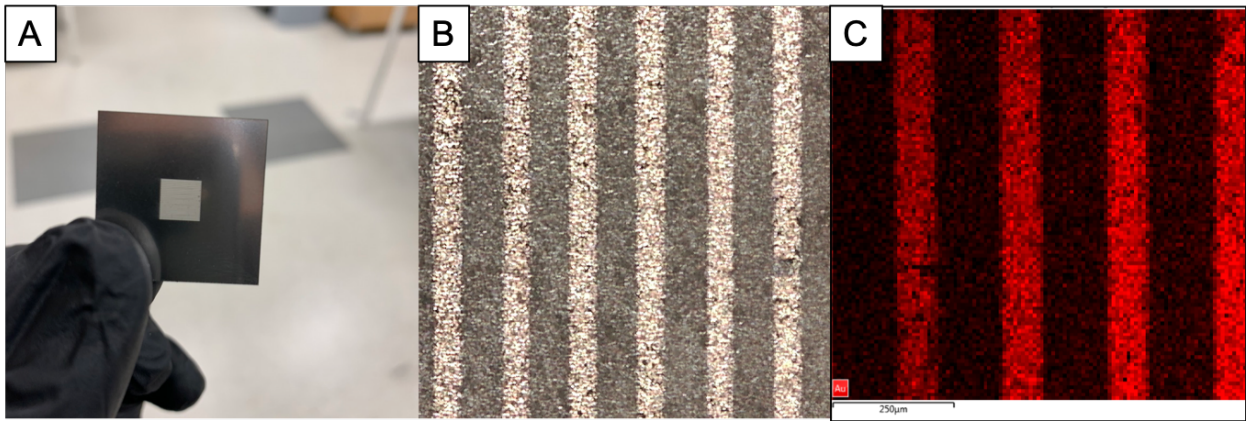

Figure 4.2. A) Photograph of patterned shadow mask used for use with one LLZO pellet. B) Optical microscopy image of patterned Au electrode atop LLZO pellet. C) SEM-EDS map of gold signcal

The masked pellets were transferred under argon to a thermal evaporation chamber built within a nitrogen-filled glovebox (Angstrom Engineering). Gold (Kurt J. Lesker Company) was used an evaporation source for a two-step deposition process to a thickness of 200 nm (**Figure 4.2B-C**). The estimated elapsed time between carbonate removal and cathode deposition was 30 minutes. The gold patterned pellets were transferred under nitrogen back to the original glovebox and annealed at 200˚C to improve adhesion of the evaporated films. Silver conductive paste was spread across one edge of the patterned electrode to conductively link the patterned features.

4.2.3 Cell Assembly

To create the full cells, lithium foils were punched (10 mm diameter), scraped to remove oxide, pressed onto the LLZO pellet, and placed into customized Swagelok® cells (**Fig. S1**). The side of the LLZO pellet opposite the Au was gently polished with 2000 grit sandpaper inside the glovebox prior to cell assembly to re-clean the interface. Porous stainless-steel discs (McMaster-Carr) were used as current collectors on both sides of the pellet stack. These stacks were placed within PEEK cells, clamped in a vice to apply stack pressure, and rapidly connected to the MS for electrochemical testing. Ultra-high purity oxygen was flown through the cell during cycling, but was replaced with argon during MS measurements to enable observation of oxygen evolution.

4.2.4 Materials Characterization

SEM images of discharge products were obtained on an FEI Nova 600 Nanolab (Dual Beam) while EDS images were obtained on a Hitachi SU3500. Raman spectroscopy measurements were obtained on a Horiba LabRAM HR Evolution Spectrometer. Mass spectrometry measurements were performed using an HPR-40 DEMS (Hiden Analytical) operating in inline mode. All electrochemical measurements were performed on a Bio-logic SP-300 potentiostat/galvanostat/FRA.

4.3 Results and Discussion

As an initial method of identifying redox processes associated with molecular oxygen within the cell, we performed headspace switching experiments while monitoring the open circuit voltage (OCV) of these cells. An initial OCV was

measured while flowing Argon through the cell, and the slow decay of the OCV in this regime corresponds to the voltages consistent with the initial behavior of lithium alloying with gold.[132] Upon the introduction of oxygen into the cell a concurrent large increase in the OCV of the cell was observed (**Figure 4.3A**), corresponding to the presence of Li-O_2 redox behavior.

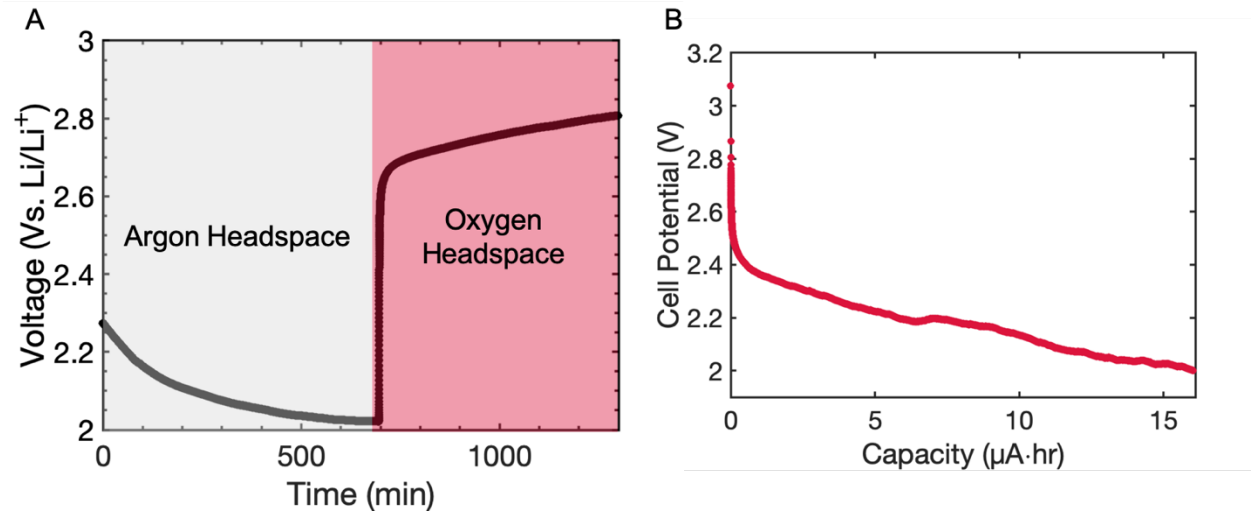

Figure 4.3. A) Measured OCV of cell at 170 ℃ before and after introduction of O2) into the cell headspace. B) First cycle discharge curve of Au | LLZO | Li cell.

A first discharge voltage profile for these cells (**Figure 4.3B),** shows an initial drop to 2.4 V followed by a steady decay down to 2 V, consistent with the formation of a finite amount of discharge product on the cell cathode.

Figure 4.4A shows an SEM image of the gold after discharge.

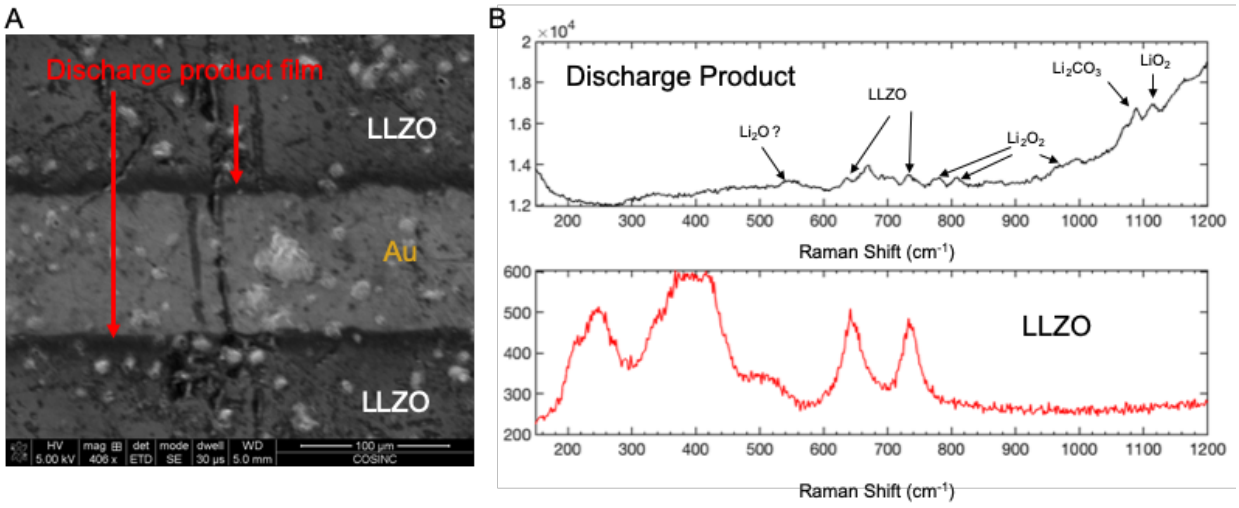

Figure 4.4. A) SEM image of discharged electrodes before cycling. B) Raman spectra of LLZO (red) and discharge product (black).

During discharge, product is deposited at the triple-phase boundary between the LLZO, Au, and O_2 headspace, which we see appear along the edges of the gold cathode. We obtain our first estimates of the thickness of discharge to be 10 microns from these images. Raman spectroscopy (**Figure 4.4B**) measurements identify the presence of Li_2O_2 and Li_2CO_3 when compared with a clean LLZO surface. The lithium carbonate is likely a trace product formed due to reaction with trace CO_2, while Li_2O_2 is the primary discharge product. A peak tentatively assigned to LiO_2 was also detected, however the stability and presence of LiO_2 has been the subject of on-going debate.[55,56] Several other peaks remain unidentified, but it is possible some could be related to discharge product compounds, such as Li_2O or LiOH. Further verification of the exact discharge product distribution is ongoing.

Galvanostatic cycling was first performed at two temperatures, 170˚C (**Figure 4.5A**) and 100˚C (**Figure 4.5C**).

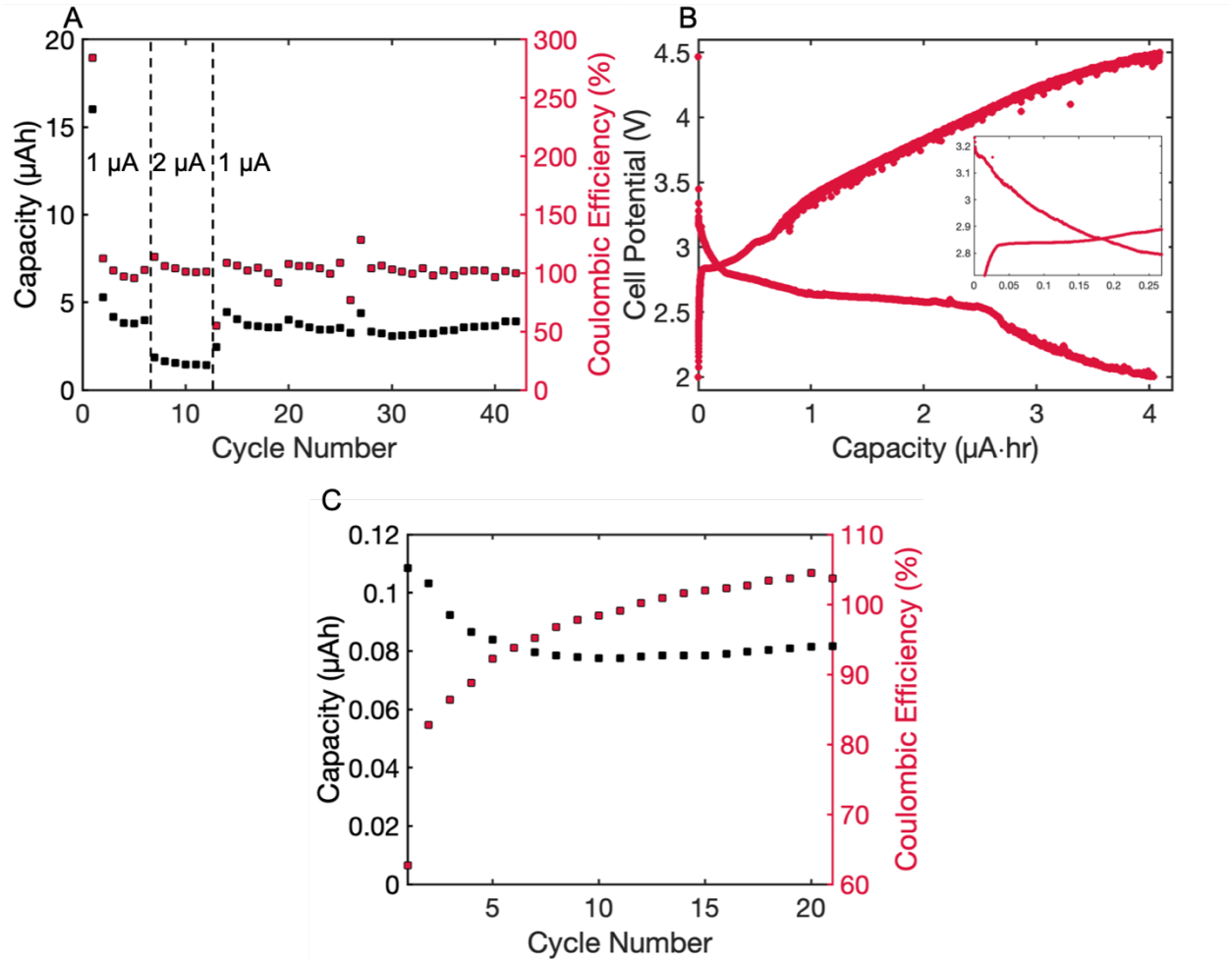

Figure 4.5. A) Discharge capacity and coulombic efficiency for cell cycled at variable rates at 170˚C. B) Voltage profile of steady state operation of 170˚C cell at a cycle rate of 1 μA. Inset shows profile at beginning of charge/discharge. C) Discharge capacity and coulombic efficiency for cell cycled at 100˚C and a rate of 1 μA.

Greater than an order of magnitude increase in the capacity was observed for the higher temperature cells, a change we attribute to increased conductivity of the discharge product. Doubling the rate of discharge at 170˚C (**Figure 4.5A**) resulted in a significantly lower discharge capacity, however this capacity was recovered upon returning back to a lower cycling current. For these cells, we would expect higher charging capacities on the first cycles, as decomposition of the Li_2CO_3 and LiOH on

the LLZO surface that has formed during processing occurs. However, this has not resulted in higher columbic efficiencies for the first cycle, as the first cycle sees a much larger discharge capacity that is only partially reversible, resulting in a first cycle coulombic efficient of 300% (**Figure 4A**). After this first cycle a stable cycling performance is achieved, with a coulombic efficiency of approximately 100%. Deviations north of 100% are likely due to partial decomposition of formed discharged products, such as could be the case for product that became detached and therefore electrically isolated from the gold current collectors.

The voltage profile of a cell after the cell has reached steady operation is presented in **Figure 4.5B**, and we note several changes that have occurred from the initial profile (**Figure 4.3B**). A more consistent plateau has appeared at 2.6 V, followed by a decline to the cutoff at 2V following this plateau, which is consistent with "sudden death" behavior once the film has reached a limiting thickness. The plateau is likely associated with the formation of Li_2O_2 (as identified by Raman spectroscopy) and/or Li_2O, which proceed via the following equations:

$$4.1)\ 2Li^+ + O_2 + 2e^- \rightarrow Li_2O_2$$

$$4.2)\ 2Li^+ + \frac{1}{2}O_2 + 2e^- \rightarrow Li_2O$$

Prior to this plateau at 2.6 V, we a small plateau (inset) is observed at 3.15 V, followed by a rapid and then more gradual decline to the 2.6 V plateau. The plateau at 2.6 V is consistent with the formation of a discharge product in liquid Li-O_2 cells, given the standard reduction potentials for both Li_2O and Li_2O_2 at 170˚C are 2.81 V and 2.82 V

respectably.[53] The behavior above 2.82 V thus cannot likely be explained by typical discharge product formation. However, this behavior could be consistent with the formation of a small amount of LiOH, given its oxidation potential at 3.45 V (at standard conditions).[133]

LiOH is a known surface contaminant for LLZO, and given that the employed cell architecture of the cell exposes the surface of the LLZO, LiOH would be expected to have formed on the surface during synthesis and assembly. We would expect to decompose LiOH according to the following reaction during charging.

$$4.3)\ 4\,LiOH \rightarrow 4\,Li^{+} + 4e^{-} + 2H_2O + O_2$$

Thus, we propose that some of the resulting H_2O remains in the cell adsorbed to the surface, and participates in the discharge reaction resulting in the small plateau followed by the sharp decline above 2.8 V, and note that this small plateau is consistent with behavior seen in cells operated with purposefully humidified O_2 in a similar configuration.[68] We also note that allowing the cell to rest for a period of time after charging, thereby expelling a portion of formed H_2O through purging of the headspace with by flowing O_2, did reduce the contribution to the total discharge capacity for the process above 2.8 V.

For the charging curve depicted in **Figure 4.5B**, two plateaus are observed at 2.8Vand 3.2V, mirroring the number of plateaus in the discharge curve, after which, we see a steady increase in cell potential up to the cutoff voltage of 4.5 V. The total capacity of these plateaus does not align with the total capacity of the discharge

plateau, suggesting an overall greater overpotential for the decomposition of discharge product after an initial low overpotential partial decomposition.

To further probe the nature of the discharge products, EC-MS experiments were conducted while charging cells. Partial pressures of O_2 and CO_2 were monitored by continuously monitoring the headspace of the cell to quantify their evolution during charging of the cell (**Figure 4.6).**

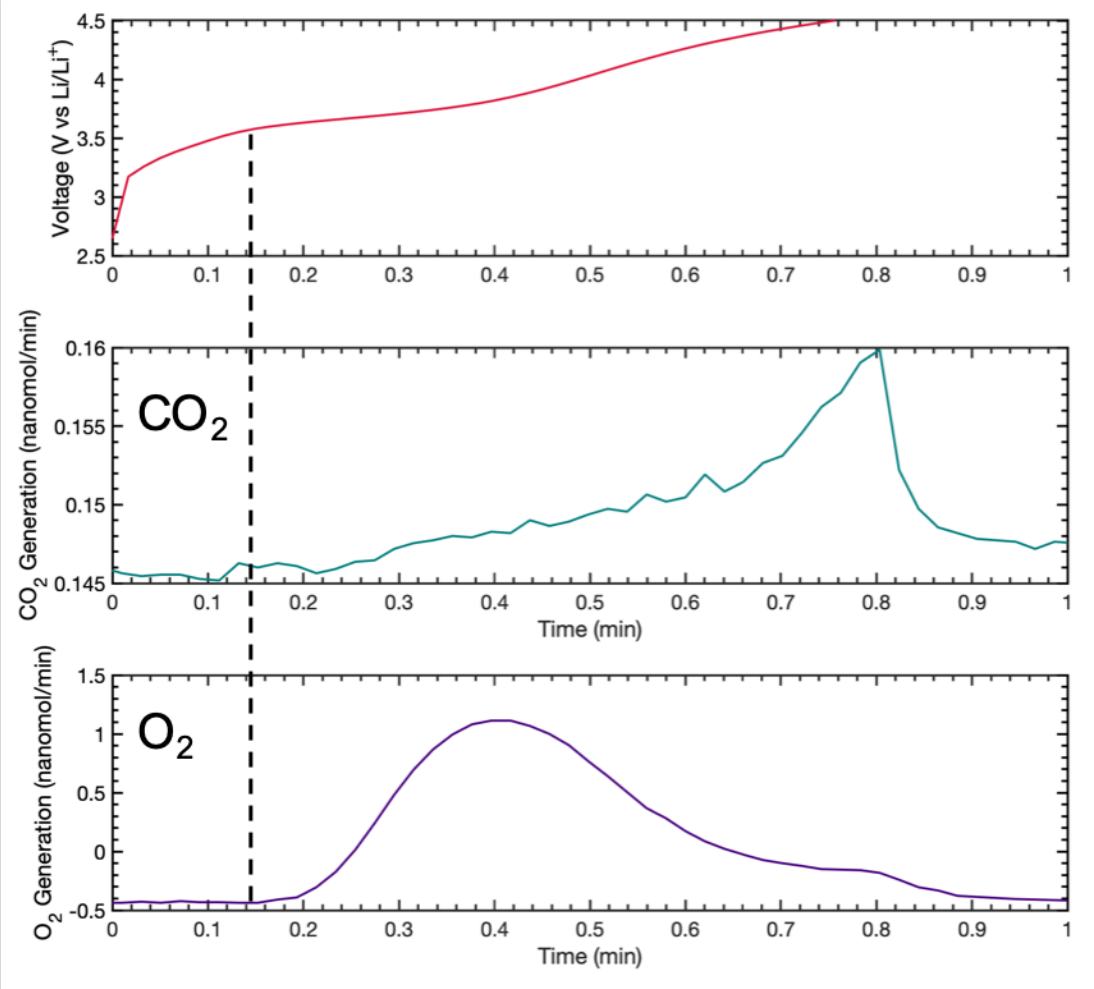

Figure 4.6 Evolution of O_2 and CO_2 as detected by EC-MS as correlated to charging voltage.

Evolution of CO_2 and O_2 begin at approximately 3.5V during charge. By utilizing calibration gases for O_2 and CO_2, we calculated total evolution for once cycle to be 0.55 nanomoles and 0.0115 nanomoles respectively. The evolution of CO_2 coincident with O_2 evolution suggests it may somehow be related to discharge product formation, however it must be a small portion of the greater discharge product due to its low amount relative compared to O_2. We observe that the amount of CO_2 continually increases until charging stops, where O_2 reaches a peak before decaying to a lower rate of evolution. This implies that at a certain point we have decomposed most of the discharge product, and further evolution of O_2 is due to Li_2CO_3 decomposition.

The presence of water was also detected during these measurements (**Figure 4.7**) and could be related to the oxidation of surface LiOH present on the LLZO.

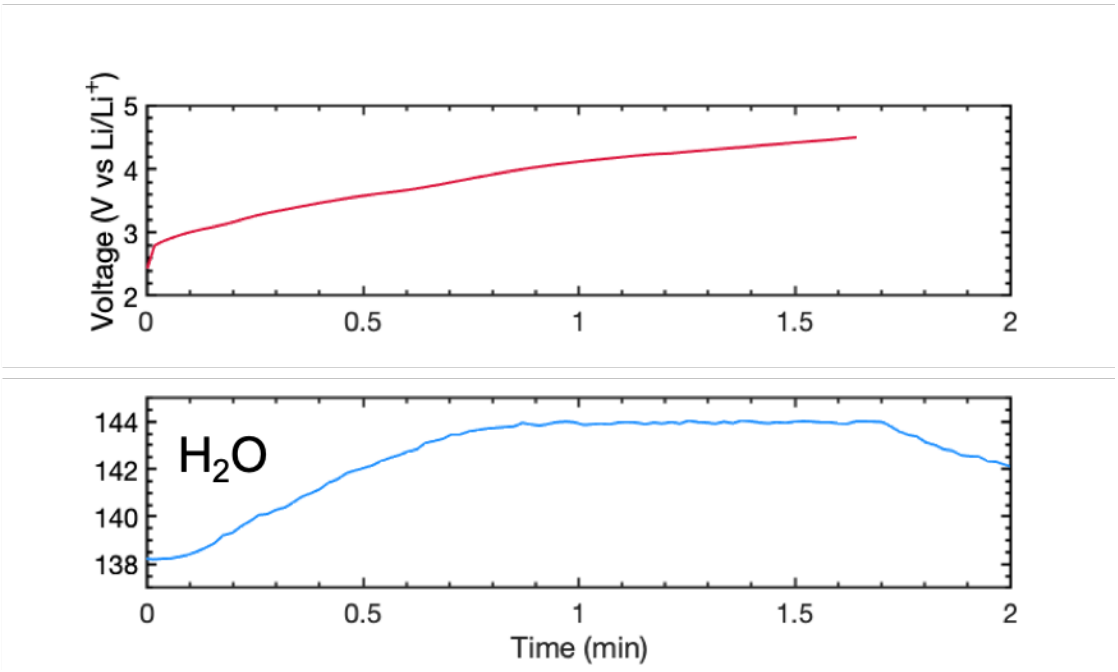

Figure 4.7 Evolution of H_2O as detected by EC-MS as correlated to charging voltage.

Its initial detection occurs below the expected equilibrium potential of 3.38 V. This therefore suggests that at least its initial decomposition could be related to the plateau observed at 2.8 V, meaning that the discharge product involves some amount of hydration ($Li_xO_yH_z$). The lack of an identifiable LiOH peak on the discharge product Raman spectra (**Figure 4.4B**) further suggests the presence of a hydrated product rather than pure LiOH. Lastly, as previously stated, the presence of water in the cell being introduced by the initial decomposition of surface LiOH is supported by the discharge profiles which, after the first charge, begin to exhibit additional plateau-like features at potentials between 3.1 and 2.7 V, coinciding with the formation of secondary discharge products.

The evolution of the cell impedance is represented by a series of Nyquist plots at both charging and discharging cutoff voltages (**Figure 4.8A&B**).

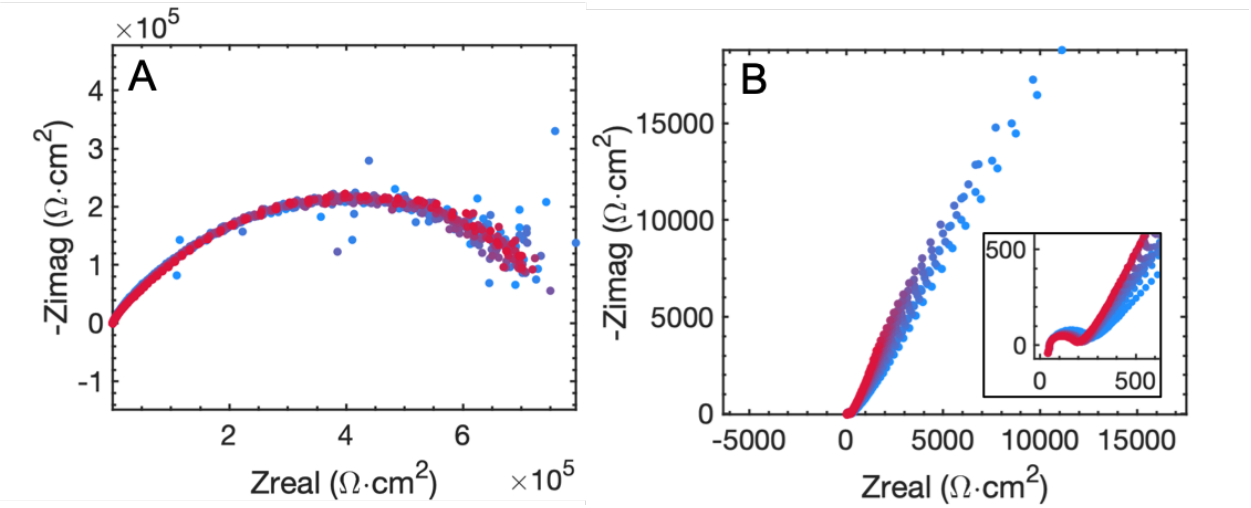

Figure 4.8. A) EIS evolution as measured immediately post-charge (4.5V) and B) post-discharge (2V).

A small arc (**Figure 4.7B**, inset) at high frequency is attributed to the grain boundary and lithium-interface impedances, while the mid-to-low frequency behavior is attributed to the cathode. Measurements post-charge should ideally relate to interface between Au and LLZO and/or the decomposition reaction for the discharge product, while post-discharge should relate to formation of discharge products and conduction through an insulating film. While one would expect an Au-LLZO interface to manifest as a blocking electrode, and therefore a near vertical line, instead a semicircle of tens of thousands of ohms is observed. We suggest that this is likely related to diffusion through a very thin film of un-decomposed discharge product after charging the cell. In relation to the discharge impedance, the near vertical behavior observed is likely related to this same diffusion, however the thickness of the film means that is diffusion pathway will be much longer, and at the same frequency cutoff, we only observe a small portion of the diffusive semicircle relative to post-charging. It is observed that EIS measurements taken after discharge are much smaller in magnitude when compared to measurements taken after charge, and is likely due to expected changes in area from discharge to charge (due to the presence/lack of discharge products). These trends in impedance further support the presence discharge products in these cells.

Currently, some discrepancy exists between the measurements of the discharge product thicknesses between MS and charge passed, and what was visually identified by SEM. The thickness of a layer of Li_2O_2 based on this amount of O_2 evolved as detected by MS would correspond to a discharge product thickness of ~450

nm. We suggest that the SEM images are more indicative of the actual thickness, and that the discrepancy for the MS-based estimates comes from underutilization of the full electrode interfacial area, which is a necessary assumption for these thickness calculations. Thickness calculations based on total charge passed (and assuming a Li_2O_2 discharge product) during discharge also require an assumption of the total area being used, but for the maximum capacities achieved cycling to a cutoff of 2V (16 μAh), would correspond to approximately 3.5 μm. However, the application of the current collector typically blocks up to a quarter of this area, making this measurement more consistent with the SEM imaging. We also note that because the exact composition and density of the discharge product is unknown, non-imaging-based estimates are subject to additional error, further suggesting that imaging is the most accurate way of assessing discharge product growth.

4.4 Conclusions

Cells with patterned Au cathodes were constructed to demonstrate the performance improvements for solid state Li-O_2 cells. By increasing the operating temperature of these cells to 170˚C, the thicknesses of grown discharge products were increased by up to several orders of magnitude relative to the surface mechanism in aprotic Li-O_2 cells. We found that these cells exhibit a highly stable cycling performance, due to the absence of compounds from which parasitic reactions could initiate. Several materials characterization techniques were used in conjunction with quantified MS and cycling measurements to gain insight into the thickness and composition of the discharge products present in these cells. These results suggest

that, when coupled with more rigorous cell design and construction to achieve higher energy densities, solid state Li-O_2 cells operating at high temperatures are worthy of further investigation for the Li-O_2 chemistry.

5 Conclusion & Future Outlook

5.1 Thesis Summary

This thesis has focused on expanding both our understanding and analytical approach to changes that occur at the cathode interface in solid state lithium batteries. While LLZO was chosen as the electrolyte because of its promising properties, the methodology explored in this dissertation was designed and presented such that it could be implemented across all types of solid electrolyte battery systems.

The viability of LMO | LLZO | Li full cells was explored through galvanostatic cycling and EIS measurements. The interpretation and analysis of these measurements were directly supported through a series of symmetric cells isolating the interfaces within these cells. Capacity fade along with an increase in cell impedance was attributed to the cathode interface, while the Li-LLZO interface was stable during cycling. XPS depth-profiling provided evidence of migration of Mn atoms, further suggesting the formation of a reaction zone at the LMO-LLZO interface. These results suggested a limited long-term stability of the LMO-LZZO pairing.

PR-EIS measurements revealed that the cycling LMO | LLZO | Li cells to high charging voltages could cause irreversible damage to these cells reflected by a significant increase in the cell impedance. Utilizing EC-MS, it was shown that trace amounts of Li_2CO_3 that had re-formed at the LMO | LLZO interface were decomposed above 3.8 V vs. Li/Li^+. This decomposition resulted in high initial charging capacities,

and caused a partial delamination of the cell cathode, limiting the accessible cathode capacity. These results represented the first use of MS to detect interfacial decomposition at the cathode-electrode interface, and suggest the importance of reporting a "time-to-synthesis" metric for the construction of LLZO cells after initial Li_2CO_3 removal.

Solid state Li-O_2 cells were constructed with a patterned Au cathode, LLZO electrolyte, and Li metal anode. Through elevated temperature operation, enabled by the use of an all-solid-state system, cells were able to grow films of discharge product up to a depth of 10 microns—significantly thicker than have been achieved by equivalent mechanisms in aprotic cells. MS measurements were utilized to gain further insight into the behavior of these cells, revealing a complex operating mechanism for product formation involving O_2, CO_2 and H_2O, the last two species being due to surface reaction with LLZO. Cycling experiments showed good stability after a period of break-in. These results demonstrate the viability of the solid state Li-O_2 system, and encourage further investigation and refinement of this unique cell configuration.

The cumulative sum of techniques explored throughout this thesis represent a fairly comprehensive toolbox that, as has been shown, can be applied to a multitude of solid state battery chemistries to gain insight into interfacial degradation and its implications for cell failure.

5.2 Recommendations for Future Work

The LMO-LLZO interface was explored extensively in this thesis, and based on the conclusions presented about the stability of this interface, further work assessing the compatibility between the materials is not recommended. However, there are many other cathode-electrolyte systems that warrant electrochemical investigation, and the methodology developed for this system would be highly applicable to other cathode-LLZO combinations. In particular, high voltage cathodes are promising new cathodes to explore. The deconstruction of full cells into symmetric cells can also be applied to the use of interlayers that help shield interfacial reaction between electrode and electrolyte. Interlayers are receiving a good deal of attention for the cathode-LLZO interface, and using this deconstruction method could help to screen stability of various interlayers for this interface by creating additional symmetric cells with and without these interlayers.

The ability to detect the evolution of gas from buried solid-solid interfaces is a relative new area, and such has many avenues for future exploration. The first is in improved experimental setup design. Because of the small amount of Li_2CO_3 available to be oxidized, design considerations for this experiment provided several difficult tradeoffs in terms of quantification. Efforts to create a more leak-proof cell for these experimental conditions would improve these quantification abilities. At the same time, no cell exists in literature that is able to utilize separate chambers to monitor gas evolution independently from the cathode and anode of the cell. While doing so would require the use of two mass spectrometers, the potential to isolate the

behavior occurring at each electrode would provide much greater insight into gas evolution reactions occurring in battery systems. With these improvements, this system would be incredibly robust, and many new combinations of solid state electrolytes and electrode materials could be explored. Employing interlayers to mitigate reaction at the cathode-solid electrolyte interface is a viable option for improved cell performance, but probing the stability of these interlayers will still be necessary, and EC-MS is a well-suited tool to aid in doing so.

Many avenues for further exploration of solid state Li-O_2 cells operating at elevated temperatures exist. Firstly, the work presented in this thesis achieved depths of discharge that greatly improve the energy density of these cells compared to similar mechanisms in aprotic Li-O_2 cells. However, the experimental design necessary for this proof-of-concept did not create a high energy density cell from an areal or volumetric perspective. A pattern density of the Au cathodes that more closely aligns with the limiting film thickness of the discharge product would greatly improve the cells energy density. Furthermore, reduction in electrolyte thickness would improve volumetric and gravimetric energy densities of these cells—a change that would likely necessitate an entirely different electrolyte synthesis, several thin-film deposition techniques would be good candidates. Lastly, even with these changes, it's possible that further gains could be made by creating a 3D-structured cathode-electrolyte interface, further increasing the areal capacity of the cell.

Next, while gold was chosen as the cathode material for its presumed inertness, there other transition metals that could serve as more effective and/or

cheaper materials, warranting their explanation. The catalytic effects of different cathode materials on both the discharge product formation and decomposition reactions could thus be explored.

Finally, this system is particularly well-suited for to be used with *operando* AFM. The Au|LLZO|Li stack could be sealed such that only part of the Au|LLZO surface is exposed, such that an AFM tip could scan the surface. Oxygen could be leaked into a custom-built, sealed, electrochemical AFM cell, and cell cycling could be initiated. The AFM would thus be able to perform measurements on the discharge products as they grow during discharge, as well as decompose during charging. The goal of these experiments would be to increase our understanding of the kinetics of discharge product formation and decomposition in solid state cells, as well as additional material properties of these discharge products such as conductivities.

6 References

(1) Whittingham, M. S. Electrical Energy Storage and Intercalation Chemistry. *Science (80-.).* **1976**, *192*, 1126–1127.

(2) Mizushima, K.; Jones, P. C.; Wiseman, P. J.; Goodenough, J. B. LixCoO2: A New Cathode Material for BAtteries of High Energy Density. *Mater. Res. Bull.* **1980**, *15*, 783–789.

(3) Thackeray, M. M.; Johnson, P. J.; de Picciotto, L. A.; Bruce, P. G.; Goodenough, J. B. Electrochemical Extraction of Lithium from LiMn2O4. *Mater. Res. Bull.* **1984**, *19* (2), 179–187.

(4) Yoshino, A. Secondary Battery, US Patent 4668595A. *United States Pat.* **1987**, No. US06/861,423, 9.

(5) Padhi, A. K.; Nanjundaswamy, K. S.; Goodenough, J. B. Phospho-Olivines as Positive-Electrode Materials for Rechargeable Lithium Batteries. *J. Electrochem. Soc.* **1997**, *144* (4), 1188–1194.

(6) Thackeray, M. M.; Wolverton, C.; Isaacs, E. D. Electrical Energy Storage for Transportation - Approaching the Limits of, and Going beyond, Lithium-Ion Batteries. *Energy Environ. Sci.* **2012**, *5* (7), 7854–7863.

(7) Liu, C.; Neale, Z. G.; Cao, G. Understanding Electrochemical Potentials of Cathode Materials in Rechargeable Batteries. *Mater. Today* **2016**, *19* (2), 109–123.

(8) Bard, Allen J.; Faulkner, L. R. *ELECTROCHEMICAL METHODS:*

Fundamentals and Applications; 2001.

(9) Ernst, S.; Heins, T. P.; Schlüter, N.; Schröder, U. Capturing the Current-Overpotential Nonlinearity of Lithium-Ion Batteries by Nonlinear Electrochemical Impedance Spectroscopy (NLEIS) in Charge and Discharge Direction. *Front. Energy Res.* **2019**, *7* (December), 1–13.

(10) O'Neill, B. C.; Tebaldi, C.; Van Vuuren, D. P.; Eyring, V.; Friedlingstein, P.; Hurtt, G.; Knutti, R.; Kriegler, E.; Lamarque, J. F.; Lowe, J.; et al. The Scenario Model Intercomparison Project (ScenarioMIP) for CMIP6. *Geosci. Model Dev.* **2016**, *9* (9), 3461–3482.

(11) Environmental Protection Agency. DRAFT Inventory of U.S Greenhouse Gas Emissions and Sinks 1990-2019. **2021**.

(12) Howell, D. Vehicle Technologies Office: Electrochemical Energy Storage R&D Overview. **2017**.

(13) Loveridge, M. J.; Remy, G.; Kourra, N.; Genieser, R.; Barai, A.; Lain, M. J.; Guo, Y.; Amor-Segan, M.; Williams, M. A.; Amietszajew, T.; et al. Looking Deeper into the Galaxy (Note 7). *Batteries* **2018**, *4* (1), 1–11.

(14) Janek, J.; Zeier, W. G. A Solid Future for Battery Development. *Nat. Energy* **2016**, *1* (9), 1–4.

(15) Chen, S.; Dai, F.; Cai, M. Opportunities and Challenges of High-Energy Lithium Metal Batteries for Electric Vehicle Applications. *ACS Energy Lett.* **2020**, *5* (10), 3140–3151.

(16) Zhang, B.; Tan, R.; Yang, L.; Zheng, J.; Zhang, K.; Mo, S.; Lin, Z.; Pan, F.

Mechanisms and Properties of Ion-Transport in Inorganic Solid Electrolytes. *Energy Storage Mater.* **2018**, *10* (February 2017), 139–159.

(17) Alpen, U. v.; Rabenau, A.; Talat, G. H. Ionic Conductivity in Li3N Single Crystals. **1977**, *30* (12), 621–622.

(18) Jones, K. S.; Rudawski, N. G.; Oladeji, I.; Pitts, R.; Fox, R. The State of Solid-State Batteries. *Am. Ceram. Soc. Bull.* **2012**, *91* (2), 26–31.

(19) Murugan, R.; Thangadurai, V.; Weppner, W. Fast Lithium Ion Conduction in Garnet-Type Li7La3Zr2O12 **. **2007**, *4*, 7778–7781.

(20) Geiger, C. A.; Alekseev, E.; Lazic, B.; Fisch, M.; Armbruster, T.; Langner, R.; Fechtelkord, M.; Kim, N.; Pettke, T.; Weppner, W. Crystal Chemistry and Stability of "Li7La 3Zr2O12" Garnet: A Fast Lithium-Ion Conductor. *Inorg. Chem.* **2011**, *50* (3), 1089–1097.

(21) Wolfenstine, J.; Sakamoto, J.; Allen, J. L. Electron Microscopy Characterization of Hot-Pressed Al Substituted Li 7La 3Zr 2O 12. *J. Mater. Sci.* **2012**, *47* (10), 4428–4431.

(22) Rangasamy, E.; Wolfenstine, J.; Sakamoto, J. The Role of Al and Li Concentration on the Formation of Cubic Garnet Solid Electrolyte of Nominal Composition Li 7La 3Zr 2O 12. *Solid State Ionics* **2012**, *206*, 28–32.

(23) Mottet, M.; Marcolongo, A.; Laino, T.; Tavernelli, I. Doping in Garnet-Type Electrolytes: Kinetic and Thermodynamic Effects from Molecular Dynamics Simulations. *Phys. Rev. Mater.* **2019**, *3* (3), 1–13.

(24) Kotobuki, M.; Munakata, H.; Kanamura, K.; Sato, Y.; Yoshida, T. Compatibility

of Li[Sub 7]La[Sub 3]Zr[Sub 2]O[Sub 12] Solid Electrolyte to All-Solid-State Battery Using Li Metal Anode. *J. Electrochem. Soc.* **2010**, *157* (10), A1076.

(25) Monroe, C.; Newman, J. The Impact of Elastic Deformation on Deposition Kinetics at Lithium/Polymer Interfaces. *J. Electrochem. Soc.* **2005**, *152* (2), A396.

(26) Ren, Y.; Shen, Y.; Lin, Y.; Nan, C. W. Direct Observation of Lithium Dendrites inside Garnet-Type Lithium-Ion Solid Electrolyte. *Electrochem. commun.* **2015**, *57*, 27–30.

(27) Ishiguro, K.; Nakata, Y.; Matsui, M.; Uechi, I.; Takeda, Y.; Yamamoto, O.; Imanishi, N. Stability of Nb-Doped Cubic Li 7 La 3 Zr 2 O 12 with Lithium Metal . *J. Electrochem. Soc.* **2013**, *160* (10), A1690–A1693.

(28) Luntz, A. C.; Voss, J.; Reuter, K. Interfacial Challenges in Solid-State Li Ion Batteries. *J. Phys. Chem. Lett.* **2015**, *6* (22), 4599–4604.

(29) Krauskopf, T.; Hartmann, H.; Zeier, W. G.; Janek, J. Toward a Fundamental Understanding of the Lithium Metal Anode in Solid-State Batteries - An Electrochemo-Mechanical Study on the Garnet-Type Solid Electrolyte Li 6.25 Al 0.25 La 3 Zr 2 O 12. *ACS Appl. Mater. Interfaces* **2019**, *11* (15), 14463–14477.

(30) Sharafi, A.; Kazyak, E.; Davis, A. L.; Yu, S.; Thompson, T.; Siegel, D. J.; Dasgupta, N. P.; Sakamoto, J. Surface Chemistry Mechanism of Ultra-Low Interfacial Resistance in the Solid-State Electrolyte Li7La3Zr2O12. *Chem. Mater.* **2017**, *29* (18), 7961–7968.

(31) Sharafi, A.; Meyer, H. M.; Nanda, J.; Wolfenstine, J.; Sakamoto, J.

Characterizing the Li-Li7La3Zr2O12 Interface Stability and Kinetics as a Function of Temperature and Current Density. *J. Power Sources* **2016**, *302*, 135–139.

(32) Wang, M. J.; Choudhury, R.; Sakamoto, J. Characterizing the Li-Solid-Electrolyte Interface Dynamics as a Function of Stack Pressure and Current Density. *Joule* **2019**, *3* (9), 2165–2178.

(33) Kim, S.; Jung, C.; Kim, H.; Thomas-Alyea, K. E.; Yoon, G.; Kim, B.; Badding, M. E.; Song, Z.; Chang, J. M.; Kim, J.; et al. The Role of Interlayer Chemistry in Li-Metal Growth through a Garnet-Type Solid Electrolyte. *Adv. Energy Mater.* **2020**, *10* (12).

(34) Zhu, Y.; Connell, J. G.; Tepavcevic, S.; Zapol, P.; Garcia-Mendez, R.; Taylor, N. J.; Sakamoto, J.; Ingram, B. J.; Curtiss, L. A.; Freeland, J. W.; et al. Dopant-Dependent Stability of Garnet Solid Electrolyte Interfaces with Lithium Metal. *Adv. Energy Mater.* **2019**, *9* (12), 1–11.

(35) Wang, Z.; Chen, X.; Cheng, Y.; Niu, C. Adsorption and Deposition of Li2O2 on the Pristine and Oxidized TiC Surface by First-Principles Calculation. *J. Phys. Chem. C* **2015**, *119* (46), 25684–25695.

(36) Sharafi, A.; Yu, S.; Naguib, M.; Lee, M.; Ma, C.; Meyer, H. M.; Nanda, J.; Chi, M.; Siegel, D. J.; Sakamoto, J. Impact of Air Exposure and Surface Chemistry on Li–Li $_{7}$ La $_{3}$ Zr $_{2}$ O $_{12}$ Interfacial Resistance. *J. Mater. Chem. A* **2017**, *5* (26), 13475–13487.

(37) Zheng, H.; Wu, S.; Tian, R.; Xu, Z.; Zhu, H.; Duan, H.; Liu, H. Intrinsic

Lithiophilicity of Li–Garnet Electrolytes Enabling High-Rate Lithium Cycling. *Adv. Funct. Mater.* **2019**, *1906189*, 1–10.

(38) Porz, L.; Swamy, T.; Sheldon, B. W.; Rettenwander, D.; Frömling, T.; Thaman, H. L.; Berendts, S.; Uecker, R.; Carter, W. C.; Chiang, Y. M. Mechanism of Lithium Metal Penetration through Inorganic Solid Electrolytes. *Adv. Energy Mater.* **2017**, *7* (20), 1–12.

(39) Swamy, T.; Park, R.; Sheldon, B. W.; Rettenwander, D.; Porz, L.; Berendts, S.; Uecker, R.; Craig Carter, W.; Chiang, Y. M. Lithium Metal Penetration Induced by Electrodeposition through Solid Electrolytes: Example in Single-Crystal Li6La3ZrTaO12 Garnet. *J. Electrochem. Soc.* **2018**, *165* (16), A3648–A3655.

(40) Han, F.; Westover, A. S.; Yue, J.; Fan, X.; Wang, F.; Chi, M.; Leonard, D. N.; Dudney, N. J.; Wang, H.; Wang, C. High Electronic Conductivity as the Origin of Lithium Dendrite Formation within Solid Electrolytes. *Nat. Energy* **2019**, *4* (3), 187–196.

(41) Kazyak, E.; Garcia-Mendez, R.; LePage, W. S.; Sharafi, A.; Davis, A. L.; Sanchez, A. J.; Chen, K. H.; Haslam, C.; Sakamoto, J.; Dasgupta, N. P. Li Penetration in Ceramic Solid Electrolytes: Operando Microscopy Analysis of Morphology, Propagation, and Reversibility. *Matter* **2020**, *2* (4), 1025–1048.

(42) Wang, M.; Wolfenstine, J. B.; Sakamoto, J. Temperature Dependent Flux Balance of the Li/Li7La3Zr2O12 Interface. *Electrochim. Acta* **2019**, *296*, 842–847.

(43) Park, K.; Yu, B. C.; Jung, J. W.; Li, Y.; Zhou, W.; Gao, H.; Son, S.; Goodenough,

J. B. Electrochemical Nature of the Cathode Interface for a Solid-State Lithium-Ion Battery: Interface between LiCoO2 and Garnet-Li7La3Zr2O12. *Chem. Mater.* **2016**, *28* (21), 8051–8059.

(44) Ohta, S.; Kobayashi, T.; Seki, J.; Asaoka, T. Electrochemical Performance of an All-Solid-State Lithium Ion Battery with Garnet-Type Oxide Electrolyte. *J. Power Sources* **2012**, *202*, 332–335.

(45) Zarabian, M.; Bartolini, M.; Pereira-Almao, P.; Thangadurai, V. X-Ray Photoelectron Spectroscopy and AC Impedance Spectroscopy Studies of Li-La-Zr-O Solid Electrolyte Thin Film/LiCoO2 Cathode Interface for All-Solid-State Li Batteries. *J. Electrochem. Soc.* **2017**, *164* (6), A1133–A1139.

(46) Tsai, C. L.; Ma, Q.; Dellen, C.; Lobe, S.; Vondahlen, F.; Windmüller, A.; Grüner, D.; Zheng, H.; Uhlenbruck, S.; Finsterbusch, M.; et al. A Garnet Structure-Based All-Solid-State Li Battery without Interface Modification: Resolving Incompatibility Issues on Positive Electrodes. *Sustain. Energy Fuels* **2019**, *3* (1), 280–291.

(47) Vardar, G.; Bowman, W. J.; Lu, Q.; Wang, J.; Chater, R. J.; Aguadero, A.; Seibert, R.; Terry, J.; Hunt, A.; Waluyo, I.; et al. Structure, Chemistry, and Charge Transfer Resistance of the Interface between Li7La3Zr2O12 Electrolyte and LiCoO2 Cathode. *Chem. Mater.* **2018**, *30* (18), 6259–6276.

(48) Hänsel, C.; Afyon, S.; Rupp, J. L. M. Investigating the All-Solid-State Batteries Based on Lithium Garnets and a High Potential Cathode-LiMn1.5Ni0.5O4. *Nanoscale* **2016**, *8* (43), 18412–18420.

(49) Xiao, Y.; Miara, L. J.; Wang, Y.; Ceder, G. Computational Screening of Cathode Coatings for Solid-State Batteries. *Joule* **2019**, *3* (5), 1252–1275.

(50) Miara, L. J.; Richards, W. D.; Wang, Y. E.; Ceder, G. First-Principles Studies on Cation Dopants and Electrolyte|Cathode Interphases for Lithium Garnets. *Chem. Mater.* **2015**, *27* (11), 4040–4047.

(51) Abraham, K. M. A Polymer Electrolyte-Based Rechargeable Lithium/Oxygen Battery. *J. Electrochem. Soc.* **1996**, *143* (1), 1.

(52) Girishkumar, G.; McCloskey, B.; Luntz, a. C.; Swanson, S.; Wilcke, W. Lithium-Air Battery: Promise and Challenges. *J. Phys. Chem. Lett.* **2010**, *1* (14), 2193–2203.

(53) Xia, C.; Kwok, C. Y.; Nazar, L. F. A High-Energy-Density Lithium-Oxygen Battery Based on a Reversible Four-Electron Conversion to Lithium Oxide. *Science (80-.).* **2018**, *361* (6404), 777–781.

(54) Giordani, V.; Tozier, D.; Uddin, J.; Tan, H.; Gallant, B. M.; McCloskey, B. D.; Greer, J. R.; Chase, G. V.; Addison, D. Rechargeable-Battery Chemistry Based on Lithium Oxide Growth through Nitrate Anion Redox. *Nat. Chem.* **2019**, *11* (December).

(55) Kwak, W. J.; Park, J. B.; Jung, H. G.; Sun, Y. K. Controversial Topics on Lithium Superoxide in Li-O2 Batteries. *ACS Energy Lett.* **2017**, *2* (12), 2756–2760.

(56) Halder, A.; Wang, H.-H.; Lau, K. C.; Assary, R. S.; Lu, J.; Vajda, S.; Amine, K.; Curtiss, L. A. Identification and Implications of Lithium Superoxide in Li–O $_2$

Batteries. *ACS Energy Lett.* **2018**, 1105–1109.

(57) Mahne, N.; Fontaine, O.; Thotiyl, M. O.; Wilkening, M.; Freunberger, S. A. Mechanism and Performance of Lithium-Oxygen Batteries-a Perspective. *Chem. Sci.* **2017**, *8* (10), 6716–6729.

(58) McCloskey, B. D.; Speidel, A.; Scheffler, R.; Miller, D. C.; Viswanathan, V.; Hummelshøj, J. S.; Nørskov, J. K.; Luntz, A. C.; Change, L.; Lcm, M. Twin Problems of Interfacial Carbonate Formation in Nonaqueous Li-O2 Batteries. *J. Phys. Chem. Lett.* **2012**, *3* (Lcm), 672–681.

(59) Mahne, N.; Schafzahl, B.; Leypold, C.; Leypold, M.; Grumm, S.; Leitgeb, A.; Strohmeier, G. A.; Wilkening, M.; Fontaine, O.; Kramer, D.; et al. Singlet Oxygen Generation as a Major Cause for Parasitic Reactions during Cycling of Aprotic Lithium–Oxygen Batteries. *Nat. Energy* **2017**, *2* (March), 17036.

(60) McCloskey, B. D.; Scheffler, R.; Speidel, A.; Bethune, D. S.; Shelby, R. M.; Luntz, a C. On the Efficacy of Electrocatalysis in Nonaqueous Li-O2 Batteries. *J. Am. Chem. Soc.* **2011**, *133* (45), 18038–18041.

(61) Viswanathan, V.; Thygesen, K. S.; Hummelshj, J. S.; Nrskov, J. K.; Girishkumar, G.; McCloskey, B. D.; Luntz, A. C. Electrical Conductivity in Li 2O 2 and Its Role in Determining Capacity Limitations in Non-Aqueous Li-O 2 Batteries. *J. Chem. Phys.* **2011**, *135* (21).

(62) Laoire, C. O.; Mukerjee, S.; Abraham, K. M.; Plichta, E. J.; Hendrickson, M. A. Influence of Nonaqueous Solvents on the Electrochemistry of Oxygen in the Rechargeable Lithium−Air Battery. *J. Phys. Chem. C* **2010**, *114* (19), 9178–

9186.

(63) Johnson, L.; Li, C.; Liu, Z.; Chen, Y.; Freunberger, S. A.; Ashok, P. C.; Praveen, B. B.; Dholakia, K.; Tarascon, J. M.; Bruce, P. G. The Role of LiO 2 Solubility in O 2 Reduction in Aprotic Solvents and Its Consequences for Li-O 2 Batteries. *Nat. Chem.* **2014**, *6* (12), 1091–1099.

(64) Kwak, W.-J.; Kim, H.; Jung, H.-G.; Aurbach, D.; Sun, Y.-K. Review—A Comparative Evaluation of Redox Mediators for Li-O 2 Batteries: A Critical Review . *J. Electrochem. Soc.* **2018**, *165* (10), A2274–A2293.

(65) Giordani, V.; Tozier, D.; Tan, H.; Burke, C. M.; Gallant, B. M.; Uddin, J.; Greer, J. R.; McCloskey, B. D.; Chase, G. V.; Addison, D. A Molten Salt Lithium-Oxygen Battery. *J. Am. Chem. Soc.* **2016**, *138* (8), 2656–2663.

(66) Kumar, B.; Kumar, J.; Leese, R.; Fellner, J. P.; Rodrigues, S. J.; Abraham, K. M. A Solid-State, Rechargeable, Long Cycle Life Lithium–Air Battery. *J. Electrochem. Soc.* **2010**, *157* (1), A50.

(67) Suzuki, Y.; Kami, K.; Watanabe, K.; Imanishi, N. Characteristics of Discharge Products in All-Solid-State Li-Air Batteries. *Solid State Ionics* **2015**, *278*, 222–227.

(68) Suzuki, Y.; Watanabe, K.; Sakuma, S.; Imanishi, N. Electrochemical Performance of an All-Solid-State Lithium-Oxygen Battery under Humidified Oxygen. *Solid State Ionics* **2016**, *289*, 72–76.

(69) Sun, J.; Zhao, N.; Li, Y.; Guo, X.; Feng, X.; Liu, X.; Liu, Z.; Cui, G.; Zheng, H.; Gu, L.; et al. A Rechargeable Li-Air Fuel Cell Battery Based on Garnet Solid

Electrolytes. *Sci. Rep.* **2017**, *7* (8), 41217.

(70) Delluva, A. A.; Dudoff, J.; Teeter, G.; Holewinski, A. Cathode Interface Compatibility of Amorphous LiMn2O4(LMO) and Li7La3Zr2O12(LLZO) Characterized with Thin-Film Solid-State Electrochemical Cells. *ACS Appl. Mater. Interfaces* **2020**, *12* (22), 24992–24999.

(71) Wu, B.; Wang, S.; Evans IV, W. J.; Deng, D. Z.; Yang, J.; Xiao, J. Interfacial Behaviours between Lithium Ion Conductors and Electrode Materials in Various Battery Systems. *J. Mater. Chem. A* **2016**, *4* (40), 15266–15280.

(72) Kotobuki, M.; Kanamura, K.; Sato, Y.; Yoshida, T. Fabrication of All-Solid-State Lithium Battery with Lithium Metal Anode Using Al2O3-Added Li7La3Zr 2O12 Solid Electrolyte. *J. Power Sources* **2011**, *196* (18), 7750–7754.

(73) Thompson, T.; Yu, S.; Williams, L.; Schmidt, R. D.; Garcia-Mendez, R.; Wolfenstine, J.; Allen, J. L.; Kioupakis, E.; Siegel, D. J.; Sakamoto, J. Electrochemical Window of the Li-Ion Solid Electrolyte Li7La3Zr2O12. *ACS Energy Lett.* **2017**, *2* (2), 462–468.

(74) Nakayama, M.; Kotobuki, M.; Munakata, H.; Nogami, M.; Kanamura, K. First-Principles Density Functional Calculation of Electrochemical Stability of Fast Li Ion Conducting Garnet-Type Oxides. *Phys. Chem. Chem. Phys.* **2012**, *14* (28), 10008–10014.

(75) Ma, C.; Cheng, Y.; Yin, K.; Luo, J.; Sharafi, A.; Sakamoto, J.; Li, J.; More, K. L.; Dudney, N. J.; Chi, M. Interfacial Stability of Li Metal-Solid Electrolyte Elucidated via in Situ Electron Microscopy. *Nano Lett.* **2016**, *16* (11), 7030–

7036.

(76) Han, F.; Westover, A. S.; Yue, J.; Fan, X.; Wang, F.; Chi, M.; Leonard, D. N.; Dudney, N. J.; Wang, H.; Wang, C. High Electronic Conductivity as the Origin of Lithium Dendrite Formation within Solid Electrolytes. *Nat. Energy* **2019**, *4* (3), 187–196.

(77) Taylor, N. J.; Stangeland-Molo, S.; Haslam, C. G.; Sharafi, A.; Thompson, T.; Wang, M.; Garcia-Mendez, R.; Sakamoto, J. Demonstration of High Current Densities and Extended Cycling in the Garnet Li7La3Zr2O12solid Electrolyte. *J. Power Sources* **2018**, *396* (April), 314–318.

(78) Albertus, P.; Babinec, S.; Litzelman, S.; Newman, A. Status and Challenges in Enabling the Lithium Metal Electrode for High-Energy and Low-Cost Rechargeable Batteries. *Nat. Energy* **2018**, *3* (1), 16–21.

(79) Il'ina, E. A.; Raskovalov, A. A. Studying of Superionic Solid Electrolyte Li7La3Zr2O12 Stability by Means of Chemical Thermodynamics for Application in All-Solid-State Batteries. *Electrochim. Acta* **2020**, *330*, 135220.

(80) Wakasugi, J.; Munakata, H.; Kanamura, K. Thermal Stability of Various Cathode Materials against Li6.25Al0.25La3Zr2O12 Electrolyte. *Electrochemistry* **2017**, *85* (2), 77–81.

(81) Ren, Y.; Liu, T.; Shen, Y.; Lin, Y.; Nan, C. W. Chemical Compatibility between Garnet-like Solid State Electrolyte Li6.75La3Zr1.75Ta0.25O12and Major Commercial Lithium Battery Cathode Materials. *J. Mater.* **2016**, *2* (3), 256–264.

(82) Yan, X.; Li, Z.; Wen, Z.; Han, W. Li/Li7La3Zr2O12/LiFePO4all-Solid-State Battery with Ultrathin Nanoscale Solid Electrolyte. *J. Phys. Chem. C* **2017**, *121* (3), 1431–1435.

(83) Zhang, N.; Long, X.; Wang, Z.; Yu, P.; Han, F.; Fu, J.; Ren, G.; Wu, Y.; Zheng, S.; Huang, W.; et al. Mechanism Study on the Interfacial Stability of a Lithium Garnet-Type Oxide Electrolyte against Cathode Materials. *ACS Appl. Energy Mater.* **2018**, *1* (11), 5968–5976.

(84) Wang, D.; Sun, Q.; Luo, J.; Liang, J.; Sun, Y.; Li, R.; Adair, K.; Zhang, L.; Yang, R.; Lu, S.; et al. Mitigating the Interfacial Degradation in Cathodes for High-Performance Oxide-Based Solid-State Lithium Batteries. *ACS Appl. Mater. Interfaces* **2019**, *11* (5), 4954–4961.

(85) Jin, Y.; McGinn, P. J. Al-Doped Li 7La 3Zr 2O 12 Synthesized by a Polymerized Complex Method. *J. Power Sources* **2011**, *196* (20), 8683–8687.

(86) Put, B.; Vereecken, P. M.; Labyedh, N.; Sepulveda, A.; Huyghebaert, C.; Radu, I. P.; Stesmans, A. High Cycling Stability and Extreme Rate Performance in Nanoscaled LiMn2O4 Thin Films. *ACS Appl. Mater. Interfaces* **2015**, *7* (40), 22413–22420.

(87) Fehse, M.; Trócoli, R.; Ventosa, E.; Hernández, E.; Sepúlveda, A.; Morata, A.; Tarancón, A. Ultrafast Dischargeable LiMn2O4 Thin-Film Electrodes with Pseudocapacitive Properties for Microbatteries. *ACS Appl. Mater. Interfaces* **2017**, *9* (6), 5295–5301.

(88) Dudney, N. J. Solid-State Thin-Film Rechargeable Batteries. *Mater. Sci. Eng.*

B Solid-State Mater. Adv. Technol. **2005**, *116* (3 SPEC.ISS.), 245–249.

(89) Dudney, N. J.; Bates, J. B.; Zuhr, R. A.; Young, S.; Robertson, J. D.; Jun, H. P.; Hackney, S. A. Nanocrystalline Li x Mn 2 ⁄ y O 4 Cathodes for Solid-State Thin-Film Rechargeable Lithium Batteries. *Journal of the Electrochemical Society*. 2000, pp 2455–2464.

(90) Iriyama, Y.; Nishimoto, K.; Yada, C.; Abe, T.; Ogumi, Z.; Kikuchi, K. Charge-Transfer Reaction at the Lithium Phosphorus Oxynitride Glass Electrolyte/Lithium Manganese Oxide Thin-Film Interface and Its Stability on Cycling. *J. Electrochem. Soc.* **2006**, *153* (5), A821.

(91) Huang, X.; Xiu, T.; Badding, M. E.; Wen, Z. Two-Step Sintering Strategy to Prepare Dense Li-Garnet Electrolyte Ceramics with High Li + Conductivity. *Ceram. Int.* **2017**.

(92) Matsui, M.; Takahashi, K.; Sakamoto, K.; Hirano, A.; Takeda, Y.; Yamamoto, O.; Imanishi, N. Phase Stability of a Garnet-Type Lithium Ion Conductor Li 7La3Zr2O12. *Dalt. Trans.* **2014**, *43* (3), 1019–1024.

(93) Diffusion, L. IV . Transport Phenomena Lecture 16 : Concentration Polarization. *Transport* **2015**, *1* (2), 1–8.

(94) Bates, J. B.; Dudney, N. J.; Lubben, D. C.; Gruzalski, G. R.; Kwak, B. S.; Yu, X.; Zuhr, R. A. Thin-Film Rechargeable Lithium Batteries. *J. Power Sources* **1995**, *54* (1), 58–62.

(95) Krauskopf, T.; Mogwitz, B.; Rosenbach, C.; Zeier, W. G.; Janek, J. Diffusion Limitation of Lithium Metal and Li–Mg Alloy Anodes on LLZO Type Solid

Electrolytes as a Function of Temperature and Pressure. *Adv. Energy Mater.* **2019**, *1902568*, 1902568.

(96) Cassel, A.; Fleutot, B.; Courty, M.; Viallet, V.; Morcrette, M. Sol-Gel Synthesis and Electrochemical Properties Extracted by Phase Inflection Detection Method of NASICON-Type Solid Electrolytes LiZr2(PO4)3 and Li1.2Zr1.9Ca0.1(PO4)3. *Solid State Ionics* **2017**, *309* (March), 63–70.

(97) Larfaillou, S.; Guy-Bouyssou, D.; Le Cras, F.; Franger, S. Comprehensive Characterization of All-Solid-State Thin Films Commercial Microbatteries by Electrochemical Impedance Spectroscopy. *J. Power Sources* **2016**, *319*, 139–146.

(98) West, A.; Irvine, J.; Sinclair, D. Electroceramics : Characterization by Impedance Spectroscopy. *Adv. Mater.* **1990**, *2* (3), 132–138.

(99) Tenhaeff, W. E.; Rangasamy, E.; Wang, Y.; Sokolov, A. P.; Wolfenstine, J.; Sakamoto, J.; Dudney, N. J. Resolving the Grain Boundary and Lattice Impedance of Hot-Pressed Li7La3Zr2O12 Garnet Electrolytes. *ChemElectroChem* **2014**, *1* (2), 375–378.

(100) Orazem, M. E.; Pàbre, N.; Tribollet, B. Enhanced Graphical Representation of Electrochemical Impedance Data. *J. Electrochem. Soc.* **2006**, *153* (4), 129–136.

(101) Lim, C. IV . Transport Phenomena Lecture 20 : Warburg Impedance. *MIT OpenCourseWare* **1899**, 1–7.

(102) Malherbe, J. B.; Hofmann, S.; Sanz, J. M. Preferential Sputtering of Oxides: A Comparison of Model Predictions with Experimental Data. *Appl. Surf. Sci.*

1986, *27* (3), 355–365.

(103) Lobe, S.; Dellen, C.; Windmüller, A.; Tsai, C. L.; Vondahlen, F.; Uhlenbruck, S.; Guillon, O. Challenges Regarding Thin Film Deposition of Garnet Electrolytes for All-Solid-State Lithium Batteries with High Energy Density. *Ionics (Kiel).* **2018**, *24* (8), 2199–2208.

(104) Wood, K. N.; Teeter, G. XPS on Li Battery Related Compounds: Analysis of Inorganic SEI Phases and a Methodology for Charge Correction. *ACS Appl. Energy Mater.* **2018**, *1*, acsaem.8b00406.

(105) Cheng, L.; Crumlin, E. J.; Chen, W.; Qiao, R.; Hou, H.; Franz Lux, S.; Zorba, V.; Russo, R.; Kostecki, R.; Liu, Z.; et al. The Origin of High Electrolyte-Electrode Interfacial Resistances in Lithium Cells Containing Garnet Type Solid Electrolytes. *Phys. Chem. Chem. Phys.* **2014**, *16* (34), 18294–18300.

(106) Cheng, L.; Liu, M.; Mehta, A.; Xin, H.; Lin, F.; Persson, K.; Chen, G.; Crumlin, E. J.; Doeff, M. Garnet Electrolyte Surface Degradation and Recovery. *ACS Appl. Energy Mater.* **2018**, *1* (12), 7244–7252.

(107) Han, F.; Yue, J.; Chen, C.; Zhao, N.; Fan, X.; Ma, Z.; Gao, T.; Wang, F.; Guo, X.; Wang, C. Interphase Engineering Enabled All-Ceramic Lithium Battery. *Joule* **2018**, *2* (3), 497–508.

(108) Yu, S.; Park, H.; Siegel, D. J. Thermodynamic Assessment of Coating Materials for Solid-State Li, Na, and K Batteries. *ACS Appl. Mater. Interfaces* **2019**, *11* (40), 36607–36615.

(109) Huo, H.; Luo, J.; Thangadurai, V.; Guo, X.; Nan, C. W.; Sun, X. Li2CO3: A

Critical Issue for Developing Solid Garnet Batteries. *ACS Energy Lett.* **2020**, *5* (1), 252–262.

(110) Mahne, N.; Renfrew, S. E.; McCloskey, B. D.; Freunberger, S. A. Electrochemical Oxidation of Lithium Carbonate Generates Singlet Oxygen. *Angew. Chemie Int. Ed.* **2018**.

(111) Wang, M. J.; Choudhury, R.; Sakamoto, J. Characterizing the Li-Solid-Electrolyte Interface Dynamics as a Function of Stack Pressure and Current Density. *Joule* **2019**, *3* (9), 2165–2178.

(112) Lu, Y.; Huang, X.; Ruan, Y.; Wang, Q.; Kun, R.; Yang, J.; Wen, Z. An: In Situ Element Permeation Constructed High Endurance Li-LLZO Interface at High Current Densities. *J. Mater. Chem. A* **2018**, *6* (39), 18853–18858.

(113) Zheng, H.; Wu, S.; Tian, R.; Xu, Z.; Zhu, H.; Duan, H.; Liu, H. Intrinsic Lithiophilicity of Li–Garnet Electrolytes Enabling High-Rate Lithium Cycling. *Adv. Funct. Mater.* **2019**.

(114) McCloskey, B. D.; Bethune, D. S.; Shelby, R. M.; Girishkumar, G.; Luntz, A. C. Solvents Critical Role in Nonaqueous Lithium-Oxygen Battery Electrochemistry. *J. Phys. Chem. Lett.* **2011**, *2* (10), 1161–1166.

(115) Kim, K. J.; Rupp, J. L. M. All Ceramic Cathode Composite Design and Manufacturing towards Low Interfacial Resistance for Garnet-Based Solid-State Lithium Batteries. *Energy Environ. Sci.* **2020**, *13* (12), 4930–4945.

(116) Ohta, S.; Komagata, S.; Seki, J.; Saeki, T.; Morishita, S.; Asaoka, T. All-Solid-State Lithium Ion Battery Using Garnet-Type Oxide and Li3BO3 Solid

Electrolytes Fabricated by Screen-Printing. *J. Power Sources* **2013**, *238*, 53–56.

(117) Bates, J. B.; Dudney, N. J.; Neudecker, B.; Ueda, A.; Evans, C. D. Thin-Film Lithium and Lithium-Ion Batteries. *Solid State Ionics* **2000**, *135* (1), 33–45.

(118) Tang, S. B.; Lai, M. O.; Lu, L. Study on Li+-Ion Diffusion in Nano-Crystalline LiMn2O4 Thin Film Cathode Grown by Pulsed Laser Deposition Using CV, EIS and PITT Techniques. *Mater. Chem. Phys.* **2008**, *111* (1), 149–153.

(119) Kuwata, N.; Nakane, M.; Miyazaki, T.; Mitsuishi, K.; Kawamura, J. Lithium Diffusion Coefficient in LiMn2O4 Thin Films Measured by Secondary Ion Mass Spectrometry with Ion-Exchange Method. *Solid State Ionics* **2018**, *320* (December 2017), 266–271.

(120) Wang, H.; Rus, E.; Sakuraba, T.; Kikuchi, J.; Kiya, Y.; Abruna, H. D. CO2 and O2 Evolution at High Voltage Cathode Materials of Li-Ion Batteries: A Differential Electrochemical Mass Spectrometry Study. *Anal. Chem.* **2014**, *86* (13), 6197–6201.

(121) Renfrew, S. E.; McCloskey, B. D. Quantification of Surface Oxygen Depletion and Solid Carbonate Evolution on the First Cycle of LiNi0.6Mn0.2Co0.2O2 Electrodes. *ACS Appl. Energy Mater.* **2019**, *2* (5), 3762–3772.

(122) Castel, E.; Berg, E. J.; El Kazzi, M.; Novák, P.; Villevieille, C. Differential Electrochemical Mass Spectrometry Study of the Interface of x Li2MnO3·(1-x)LiMO2 (M = Ni, Co, and Mn) Material as a Positive Electrode in Li-Ion Batteries. *Chem. Mater.* **2014**, *26* (17), 5051–5057.

(123) Thotiyl, M. M. O.; Freunberger, S. a; Peng, Z.; Bruce, P. G. The Carbon

Electrode in Nonaqueous Li − O 2 Cells. *J. Am. Chem. Soc.* **2013**, *135* (1), 494–500.

(124) McCloskey, B. D.; Bethune, D. S.; Shelby, R. M.; Mori, T.; Scheffler, R.; Speidel, a; Sherwood, M.; Luntz, a C. Limitations in Rechargeability of Li-O2Batteries and Possible Origins. *J. Phys. Chem. Lett.* **2012**, *3*, 3043–3047.

(125) Li, Y.; Chen, X.; Dolocan, A.; Cui, Z.; Xin, S.; Xue, L.; Xu, H.; Park, K.; Goodenough, J. B. Garnet Electrolyte with an Ultralow Interfacial Resistance for Li-Metal Batteries. *J. Am. Chem. Soc.* **2018**, *140* (20), 6448–6455.

(126) Strauss, F.; Teo, J. H.; Schiele, A.; Bartsch, T.; Hatsukade, T.; Hartmann, P.; Janek, J.; Brezesinski, T. Gas Evolution in Lithium-Ion Batteries: Solid versus Liquid Electrolyte. *ACS Appl. Mater. Interfaces* **2020**, *12* (18), 20462–20468.

(127) Bartsch, T.; Strauss, F.; Hatsukade, T.; Schiele, A.; Kim, A. Y.; Hartmann, P.; Janek, J.; Brezesinski, T. Gas Evolution in All-Solid-State Battery Cells. *ACS Energy Lett.* **2018**, *3* (10), 2539–2543.

(128) Sastre, J.; Chen, X.; Aribia, A.; Tiwari, A. N.; Romanyuk, Y. E. Fast Charge Transfer across the Li7La3Zr2O12Solid Electrolyte/LiCoO2Cathode Interface Enabled by an Interphase-Engineered All-Thin-Film Architecture. *ACS Appl. Mater. Interfaces* **2020**, *12* (32), 36196–36207.

(129) Wu, J. F.; Pu, B. W.; Wang, D.; Shi, S. Q.; Zhao, N.; Guo, X.; Guo, X. In Situ Formed Shields Enabling Li 2 CO 3 -Free Solid Electrolytes: A New Route to Uncover the Intrinsic Lithiophilicity of Garnet Electrolytes for Dendrite-Free Li-Metal Batteries. *ACS Appl. Mater. Interfaces* **2019**, *11* (1), 898–905.

(130) Viswanathan, V.; Thygesen, K. S.; Hummelshøj, J. S.; Nørskov, J. K.; Girishkumar, G.; McCloskey, B. D.; Luntz, a C. Electrical Conductivity in Li2O2 and Its Role in Determining Capacity Limitations in Non-Aqueous Li-O2 Batteries. *J. Chem. Phys.* **2011**, *135* (21), 214704.

(131) Kitaura, H.; Zhou, H. All-Solid-State Lithium-Oxygen Battery with High Safety in Wide Ambient Temperature Range. *Sci. Rep.* **2015**, *5*, 1–8.

(132) Bach, P.; Stratmann, M.; Valencia-Jaime, I.; Romero, A. H.; Renner, F. U. Lithiation and Delithiation Mechanisms of Gold Thin Film Model Anodes for Lithium Ion Batteries: Electrochemical Characterization. *Electrochim. Acta* **2015**, *164*, 81–89.

(133) Burke, C. M.; Black, R.; Kochetkov, I. R.; Giordani, V.; Addison, D.; Nazar, L. F.; McCloskey, B. D. Implications of 4 e ⁻ Oxygen Reduction via Iodide Redox Mediation in Li–O ₂ Batteries. *ACS Energy Lett.* **2016**, 747–756.